

Seismic Resistance of Unreinforced Load-bearing Masonry Buildings, Retrofitted with a Strain-Hardening Cement-Based Composite

by

Mariska Kotzé



Thesis presented in partial fulfilment of the

Masters of Engineering (Civil)

in the Faculty of Engineering at Stellenbosch University

Supervisors: Dr. G. C. van Rooyen
Prof. G.P.A.G. van Zijl

March 2020

Declaration

By submitting this thesis electronically, I declare that the entirety of the work contained therein is my own, original work, that I am the sole author thereof (save to the extent explicitly otherwise stated), that reproduction and publication thereof by Stellenbosch University will not infringe any third party rights and that I have not previously in its entirety or in part submitted it for obtaining any qualification.

Date:

Abstract

There are many low-rise unreinforced load-bearing masonry (ULM) buildings in the Western Cape, South Africa, which is a seismic zone. These buildings are susceptible to collapse should a seismic event occur. Retrofitting is proposed for these buildings in order to better withstand seismic actions. A possible retrofitting technique is to use a sprayable strain-hardening cement-based composite (SHCC) overlay. It is postulated that the SHCC overlay could sufficiently improve the ductility of the masonry buildings to prevent collapse.

To determine the effect SHCC has on low-rise buildings, a non-linear finite element analysis (FEA) was done based on previous experimental and numerical testing. The previous tests comprised of masonry wallettes retrofitted with a sprayable SHCC overlay as well as tests with debonding strips between the SHCC overlay and masonry substrate. The experimental setup was replicated with FEA software and the numerical results were compared to that of the experimental tests. The numerical model was adjusted until it gave a good representation of the experimental data in terms of the diagonal shear failure and the shear force against displacement distribution.

The numerical model was then used to model a typical building in the low-income areas in the Western Cape. The building was simplified to a two dimensional problem as only a quasi-static in-plane analysis was done. Two sides of the building were considered to give a qualitative representation of the building as a whole. The East side with a 7.2 m length and no openings was modelled as well as the North side with a 32 m length with various openings and a lower wall stiffness for the ground floor.

The building model showed promising results as the SHCC overlay changed the failure mechanism on the East side from diagonal shear to flexural shear failure with a significant increase in the ductility and shear resistance. The North side maintained the diagonal shear failure, the shear resistance was also increased significantly but the ductility did not improve. It was concluded that the SHCC overlay could improve the seismic resistance of a low-rise ULM building. It is however recommended that further studies are done on the material parameters and that more experimental tests are needed on debonding strips and seismic loading.

Uittreksel

Daar is baie lae-stygende, onversterkte, lasdraende messelwerk (ULM) geboue in die Wes-Kaap, Suid-Afrika, wat 'n seismiese gebied is. Gevolglik kan hierdie geboue ineenstort indien seismiese aktiwiteit sou plaasvind. Hierdie geboue moet toegerus word om die seismiese aksies beter te weerstaan. 'n Moontlike monteringstegniek is om 'n spuitbare vervormings-verhardende sement-samestelling (SHCC) oorlaag te gebruik. Daar word gepostuleer dat die SHCC-oorlaag die duktiliteit van die messelwerkgeboue voldoende kan verbeter om ineenstorting te voorkom, of ten minste genoeg tyd te voorsien sodat die inwoners die gebou kan ontruim voor die ineenstorting.

Om die effek van SHCC op lae-stygende geboue te bepaal, is 'n nie-lineêre eindige elementanalise (FEA) gedoen op grond van vorige eksperimentele en numeriese toetse. Die vorige toetse bestaan uit messelwerk-muurborde wat met 'n spuitbare SHCC-oorlaag toegerus is, asook toetse met nie-binding stroke tussen die SHCC-oorlaag en messelwerk-substraat. Die eksperimentele opstelling is met FEA sagteware gemodelleer en die numeriese resultate is vergelyk met die van die eksperimentele toetse. Die numeriese model is aangepas totdat dit 'n goeie voorstelling van die eksperimentele toetse gee ten opsigte van die diagonaal skuifvervorming en die skuifkrag teenoor verplasing.

Die numeriese model is toe gebruik om 'n tipiese gebou in die lae-inkomstegebiede in die Wes-Kaap te modelleer. Die gebou is tot 'n tweedimensionele probleem vereenvoudig, aangesien slegs 'n kwasi-statische in-vlak-analise gedoen is. Twee kante van die gebou is beskou vir 'n kwalitatiewe voorstelling van die gebou as geheel. Die oostekant met 'n lengte van 7,2 m en geen openinge nie is gemodelleer, asook die noordekant met 'n lengte van 32 m met verskillende openings en 'n laer muurstyfheid vir die grondvloer.

Die model van die gebou het belowende resultate getoon, aangesien die SHCC-oorlaag die falingsmeganisme aan die oostekant verander het van diagonale skuiffaling na buig-skuif-faling, met 'n beduidende toename in die duktiliteit en skuifweerstand. Die noordekant het die diagonale skuiffaling gehandhaaf, die skuifweerstand is ook aansienlik verhoog, maar die duktiliteit het nie verbeter nie. Daar is tot die gevolgtrekking gekom dat die SHCC-oorlaag die seismiese weerstand van 'n lae ULM-gebou kan verbeter. Dit word egter aanbeveel dat verdere studies oor die materiaal parameters gedoen word, meer eksperimentele toetse op nie-binding stroke en seismiese belading word benodig.

Acknowledgements

I would like to express gratitude to my supervisors, Dr. Gert van Rooyen and Gideon van Zijl, without whom none of this would be possible.

In addition I would like to express my appreciation to the following people:

- Mr Hee-Jeong Kang and the rest of the Diana support team, for their speedy response and valuable advice with regards to technical aspects of using Diana.
- My office colleagues, Andrew Way and Fred Bakker for the help, support and endless entertainment they provided.
- The rest of my office colleagues for memorable coffee breaks at 10:30.

Thank you to my husband, Alwyn Kotzé, my parents, brother, family and friends for you endless love and support.

Most importantly all glory to God for making all things possible.

Contents

Declaration	i
Abstract	ii
Uittreksel	iii
Acknowledgements	iv
Contents	v
List of Figures	viii
List of Tables	x
Nomenclature	xii
Abbreviations	xv
1 Introduction	1
1.1 Motivation	2
1.2 Overview	2
2 Literature Review	3
2.1 Seismic activity in South-Africa	3
2.1.1 South African codes for Seismic activity	4
2.2 Unreinforced Masonry buildings	4
2.2.1 Masonry Structures in Seismic zones	4
2.2.2 In-Plane Failure modes of ULM walls	4
2.3 Previously researched/developed retrofitting techniques	5
2.3.1 Near Surface Mounted reinforcements	5
2.3.2 Carbon Fibre Reinforced Polymer strips	5
2.3.3 Engineered Cement-based Composite overlays	6
2.3.4 Strain Hardening Cement based Composite bonded overlay	6
2.4 SHCC Material Properties	6
2.4.1 Tension	7

CONTENTS

2.4.2	Compression	8
2.4.3	Elastic Modulus	8
2.4.4	Shear Behaviour	8
2.4.5	SHCC Material Matrix	8
2.5	Spray-able SHCC development	9
2.5.1	Fresh Properties	9
2.5.2	Hardened Properties	9
2.5.3	Shrinkage	10
2.6	Finite Element Analysis in Diana	10
2.6.1	Crack Modelling	10
2.6.2	Materials	11
2.6.3	Mesh Elements	14
2.6.4	Interface	15
2.6.5	Modelling Approach	16
2.6.6	Non-linear Analysis	16
2.7	Modal Analysis	21
2.8	Previous Research on SHCC as a Retrofitting Technique	22
2.8.1	Ductility Factor	24
2.8.2	Debonding Strip Theory	25
2.8.3	Energy Contribution Factor	25
3	Finite Element Model Development	29
3.1	Finite Element Model Setup	29
3.1.1	Geometry	29
3.1.2	Boundary Conditions	30
3.1.3	Loading	30
3.1.4	Materials	31
3.1.5	Mesh	33
3.1.6	Analyses	33
3.2	FEM of Debonding Strips	34
3.2.1	Geometry	34
3.2.2	Debonding Strip Interface	34
3.3	Output Results	35
3.4	FE Model Summary	35
4	Finite Element Model Results	36
4.1	Masonry Wall	36
4.2	SHCC retrofitting	38
4.3	Debonding strips	40
4.4	Chapter Conclusion	44
5	Full Scale Model Development	45
5.1	Representative Building	45
5.2	Geometry Simplification to 2D model	46

CONTENTS

5.3	Boundary Conditions	47
5.3.1	East side Boundary Conditions	47
5.3.2	North side Boundary Conditions	47
5.4	Loading	48
5.4.1	Service Limit State Design	48
5.4.2	Modal Analysis	49
5.5	Mesh	50
5.6	Analysis and Output variables	52
6	Full Scale Model Results	53
6.1	East Side	53
6.1.1	Masonry	53
6.1.2	SHCC	54
6.2	North Side	56
6.2.1	Masonry	56
6.2.2	SHCC	57
6.2.3	Debonding strips	59
6.3	Chapter Conclusion	60
7	Conclusions and Recommendations	62
7.1	Finite Element Models of Experimental Walls	62
7.2	Full Scale FE Models of the Representative Building	63
7.3	Recommendations for further research	63
	Bibliography	65
A	Digital Appendix	A1

List of Figures

2.1	South Africa seismic hazard zone map, extracted from SANS 10160-4 (2011)	3
2.2	Damage to multi storey buildings due to earthquakes, are predominantly diagonal shear failure.	4
2.3	Failure modes of URM walls (Tomažević, 1999)	5
2.4	Retrofitting techniques for masonry infill panels.	6
2.5	Schematic illustration of tensile stress-strain comparison of Concrete, FRC and SHCC	7
2.6	Unloading and reloading tensile behaviour Boshoff (2007)	8
2.7	Rankine-Hill yield condition	11
2.8	Rankine tension yield approximation	12
2.9	Hardening Softening law of Hill behaviour	13
2.10	Exponential Tension softening curve for the Total Strain crack model	14
2.11	Coulomb friction criteria	15
2.12	Linear Mesh Elements	15
2.13	Quadratic mesh elements	15
2.14	Quadratic Triangular Interface element	16
2.15	Different modelling approaches	16
2.16	Iteration Process	17
2.17	Newton-Raphson	18
2.18	Quasi-Newton (Secant) iteration	19
2.19	Load and Displacement control	19
2.20	Arc-length control	20
2.21	Norm Items	21
2.22	Experimental setup (De Beer, 2016)	23
2.23	Shear force over displacement of the full scale tests and a comparison to the FEM results for a double leaf masonry wall with no SHCC overlay.	24
2.24	Shear force over displacement of the full scale tests and a comparison to the FEM results for a double leaf masonry wall with a 15 mm SHCC overlay.	24
2.25	Ductility equation value illustration	25
2.26	SHCC specimens fracture patterns (Luković <i>et al.</i> , 2014)	26
2.27	Debonding strips on the masonry wall (De Jager, 2018)	26
2.28	Energy Contribution Factor parameters	27

LIST OF FIGURES

2.29	Shear force against displacement for the experimental tests and FEA with debonding strips done by De Jager (2018)	27
3.1	Basic setup of full scale shear wall test	29
3.2	Rod forces	30
3.3	Mesh dependency of quadrilateral and triangular elements with high integration	33
3.4	25mm Triangular mesh of the shear wall model	34
3.5	Basic setup of the full scale shear wall test with debonding strips	35
4.1	Shear force against displacement for the Masonry wall with no retrofitting . .	36
4.2	Principal strains (E1) for the masonry wall with no retrofitting at the respective displacements.	37
4.3	Shear force against displacement for the masonry wall retrofitted with an SHCC overlay	38
4.4	Principal strains (E1) in the SHCC overlay at different displacements.	39
4.5	Tractions in the interface between the masonry substrate and the SHCC overlay at the respective displacements.	40
4.6	Shear force against displacement for the Masonry wall with SHCC overlay and debonding strips	41
4.7	Shear force against displacement for the Masonry wall with SHCC overlay and 75-150 debonding strips obtained from the numerical models	41
4.8	Principal strains (E1) in the SHCC overlay at different displacements for the masonry wall retrofitted with SHCC and debonding strips.	42
4.9	Tractions in the interface between the masonry substrate and the SHCC overlay at different displacements for the retrofitted masonry wall with 75-150 debonding strips.	43
5.1	Buildings in the Cape Flats area	45
5.2	General floor plan of the buildings in the Cape Flats area Van der Kolf (2014)	46
5.3	East side view illustration of the full scale building with the loading and boundary conditions	47
5.4	North side view illustration of the full scale building with the loading and boundary conditions for the 8 m width	48
5.5	Simplified three degree of freedom approach for the modal analysis of the residential building	49
5.6	Mesh dependency for the full scale models using quadratic triangular elements with high integration	50
5.7	Hardening Softening Hill law for the masonry model with 125 mm elements .	51
5.8	Mesh used for the full-scale models	51
6.1	Shear force against displacement for the bottom floor of the East side masonry wall with no retrofitting	53
6.2	Principal strains (E1) in the masonry with no retrofitting on the ground floor of the East side at the respective displacements	54

6.3	Shear force against displacement for the bottom floor of the East side masonry wall with SHCC retrofitting	55
6.4	Principal strains (E1) in the SHCC overlay on the ground floor of the East side at 41.8 mm displacement	55
6.5	Tractions in the SHCC overlay on the ground floor of the East side at 41.8 mm displacement	56
6.6	Shear force against displacement for the ground floor of the North side masonry wall with no retrofitting	57
6.7	Principal strains (E1) in the 220 mm masonry wall on the ground floor with no retrofitting on the North side at 7.2 mm displacement	57
6.8	Shear force against displacement for the ground floor on the North side with the masonry retrofitted with SHCC on the ground floor alone	58
6.9	Principal strains (E1) in the SHCC overlay on the ground floor of the North side at 14.5 mm displacement	58
6.10	Tractions in the interface between the SHCC overlay and the masonry substrate on the ground floor of the North side at 14.5 mm displacement	59
6.11	75-150 debonding strips applied to the ground floor of the North side	59
6.12	Shear force against displacement for the ground floor retrofitted with SHCC and debonding strips on the North side	60

List of Tables

2.1	Fibre Properties (Stander, 2007)	9
2.2	SHCC mix properties	10
2.3	Ductility Factors (De Jager, 2018)	28
2.4	ECF values at different forces (De Jager, 2018)	28
3.1	Initial and end forces for the Rods	30
3.2	Rankine-Hill model parameters for masonry	31
3.3	Rotating smeared crack material model parameters for SHCC	32
3.4	Coulomb friction interface material parameters	32
3.5	Concrete and Steel linear elastic material parameters	32
3.6	Loads applied in the respective Phases	34
3.7	Coulomb friction interface material parameters for debonding strips	35
4.1	Energy Contribution Factors	44

LIST OF TABLES

4.2	Ductility Summary	44
5.1	Densities and Loadings that were applied (SANS 10160-2, 2011)	48
5.2	Line loads applied in the respective models	49
6.1	Ductility factors and maximum shear resistance of the representative building	60
7.1	Ductility factors and maximum shear force of the numerical and experimental test for the masonry wallettes	62
7.2	Energy Contribution Factors of the numerical and experimental test for the masonry wallettes	62
7.3	Summary of the ductility factors and maximum shear resistance for the representative building	63

Nomenclature

a	Gravity acceleration, assumed to be 9.81 m/s^2
A	Area of the mesh element
A_d	Accidental load
c	Cohesion
C	Damping matrix
$\{d\}$	Displacement vector
d_0	Slump core diameter
d_1	Maximum diameter of slump
d_2	Diameter perpendicular to d_1
D_1	Maximum diameter of slump, after vibration
D_2	Diameter perpendicular to D_1 , after vibration
E	Young's Modulus
f_c	Compressive strength
\bar{f}_c	Average tensile strength at first crack
f_{ext}	External force
f_{int}	Internal force
f_t	Tensile strength

NOMENCLATURE

\bar{f}_u	Average ultimate tensile strength
F	Reaction force
F_0	Applied force
g	Residual force
G_f	Fracture energy
h	Crack bandwidth
k_n	Normal stiffness modulus
k_{t_x}	Shear stiffness modulus (x)
k_{t_y}	Shear stiffness modulus (y)
K	Stiffness
M	Mass
t_n	Normal traction
t_t	Tangent traction
$\Delta\{u\}$	Incremental displacement vector
x	Displacement
\dot{x}	Velocity
\ddot{x}	Acceleration
γ	Deformability
Γ	Deformability, after vibration
δ_u	Ultimate displacement
δ_y	Yield displacement
ϵ_0	Strain at σ_0

NOMENCLATURE

$\bar{\epsilon}_u$	Average ultimate tensile strain
ι	Identity matrix
κ_p	Plastic strain
μ	Ductility factor
ν	Poissons's ratio
ρ	Mass density
σ_0	Pre-stress
σ_{tf}	First crack stress
σ_x	Stress in the x direction
σ_y	Stress in the y direction
τ	Shear stress
ϕ	Friction angle
$\{\phi\}$	Eigenvectors
ψ	Dilatancy angle
ω	Eigenvalue

Abbreviations

<i>CAC</i>	Calcium Aluminate Cement
<i>CFRP</i>	Carbon Fibre Reinforced Polymer
<i>CoV</i>	Coefficient of Variation
<i>DTT</i>	Direct Tensile Tests
<i>ECC</i>	Engineered Cement-based Composite
<i>ECF</i>	Energy Contribution Factor
<i>FA</i>	Fly Ash
<i>FE</i>	Finite Element
<i>FEA</i>	Finite Element Analysis
<i>FEM</i>	Finite Element Model
<i>FRC</i>	Fibre Reinforced Concrete
<i>NSM</i>	Near Surface Mounted
<i>OPC</i>	Ordinary Portland Cement
<i>RC</i>	Reinforced Concrete
<i>SABS</i>	South African Bureau of Standards
<i>SANS</i>	South African National Standards
<i>SHCC</i>	Strain Hardening Cement-based Composite

ABBREVIATIONS

<i>SP</i>	Super Plasticiser
<i>SUN</i>	Stellenbosch University
<i>ULM</i>	Unreinforced Load-bearing Masonry
<i>URM</i>	Unreinforced Masonry
<i>UTT</i>	Uni-axial Tensile Tests

Chapter 1

Introduction

In South Africa there are areas that are prone to seismic activity and within these areas there are many unreinforced load-bearing masonry buildings (ULM) that are not designed to withstand seismic actions, specifically in the Western Cape. These buildings are unsafe for the inhabitants and should be retrofitted to prevent collapse if a seismic event occurs.

Masonry is a popular building material in South Africa due to it being readily available, affordable and not requiring skilled labour to construct. Most buildings of up to four stories are built from ULM. Although masonry has high compressive strength, it has low tensile strength and has a brittle shear failure. These characteristics cause masonry to have poor seismic resistance since its brittle failure mode allows little time for the occupants to evacuate the building in a seismic event.

De Beer (2016) proposed using strain hardening cement-based composite (SHCC) to retrofit these buildings. SHCC is a fibre reinforced concrete that has strain hardening followed by softening behaviour in tension which is ideal to improve the ductility of ULM buildings in order to prevent a brittle collapse. De Beer (2016) developed sprayable SHCC, tested it on masonry wallettes and found that the SHCC significantly improved the shear resistance of the masonry wallettes, but the ductility was not improved. De Jager (2018) continued on de Beer's (2016) research by introducing debonding strips between the SHCC overlay and the masonry substrate to improve the ductility and it showed promising results. De Jager (2018) also developed finite element models (FEM) in Diana (2017a) and compared their results with the experimental data.

De Beer (2016) and De Jager (2018) concluded that retrofitting ULM buildings with an SHCC overlay could be an effective retrofitting technique to improve the ductility and the seismic resistance of ULM buildings.

In this study, the finite element models were developed further. However, they are quasi-static models considering only in-plane action. The previous experimental tests were used to validate the FE models. Then using the validated FE models a typical building in the low-income areas of the Western Cape was modelled to obtain a qualitative evaluation of how the SHCC would influence the behaviour of masonry on a larger scale. This so-called representative building had to be simplified to accommodate the quasi-static, in-plane modelling approach.

This study reports on the results obtained from the numerical models, focusing on the difference in ductility due to the retrofitted SHCC overlay and the contribution in energy dissipation due to the debonding strips between the SHCC overlay and the masonry substrate. This was done for the experimental models as well as the models of the representative building.

1.1 Motivation

It is the responsibility of an engineer to ensure the safety and reliability of the structures that were designed by the engineer him/herself and others. Many ULM buildings in the Western Cape are not safe should a seismic event occur. This study aims to obtain a qualitative evaluation of how a SHCC overlay on masonry buildings would improve the seismic resistance of the structure.

1.2 Overview

Chapter 2 discusses the theoretical background regarding the seismic zones in South Africa, a detailed discussion of the material properties of SHCC, possible retrofitting techniques previously researched by other researchers, concepts on non-linear finite element analysis (FEA) and material models used in this study.

In Chapter 3 the development of the finite element model is discussed. This model is based on experimental tests and previous models thereof. The aim is to obtain the strain distribution in the masonry substrate and the SHCC overlay while obtaining a good representation of the experimental results.

Chapter 4 discusses the results that were obtained from the models developed in Chapter 3 in comparison to the findings of the experimental tests.

Chapter 5 discusses the simplification and FEM development of the representative building. The aim was to obtain the global response of the masonry walls, masonry walls retrofitted with an SHCC overlay and to obtain better insight on the effect that SHCC has on larger masonry areas.

In Chapter 6 the results obtained from the FE models of Chapter 5 are discussed in detail.

Chapter 7 discusses the overall conclusions that were drawn and recommendations for further improvement and studies that could be conducted.

Chapter 2

Literature Review

This chapter provides background information that is relevant to the study. Seismic activity in South Africa and the impact that seismic events have on multi-storey unreinforced masonry buildings are discussed. Possible retrofitting solutions for these buildings are discussed.

2.1 Seismic activity in South-Africa

Certain areas of South Africa are prone to low to moderate seismic activity. Earthquakes are rare but can have devastating consequences if structures are not designed to resist these forces.

Figure 2.1 represents a map of South Africa's peak ground acceleration in terms of gravity acceleration (g), with a probability of exceedance of 10% at a return period of 50 years. Two different zones are illustrated in the figure, namely Zone I and Zone II. These zones represent naturally occurring and mining induced seismic events respectively (SANS 10160-4, 2011). Buildings within both zones have to be designed to withstand seismic events. As seen in Figure 2.1, these zones cover a significant portion of South Africa and there is a high density of occupants within these zones.

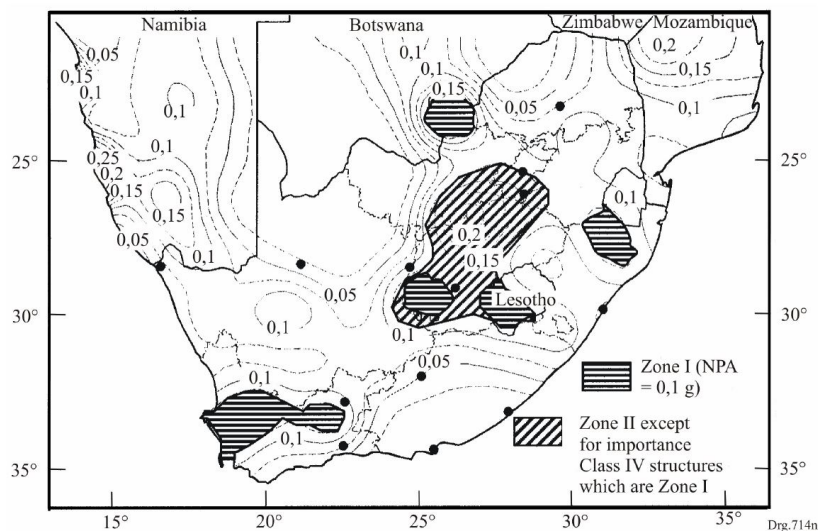


Figure 2.1: South Africa seismic hazard zone map, extracted from SANS 10160-4 (2011)

2.1.1 South African codes for Seismic activity

South Africa's design code for seismic activity was implemented in 1989 (SABS 0160, 1989) and revised in 2011 (SANS 10160-4, 2011). The SABS 0160 (1989) was seen by engineers to be over conservative and not cost effective, therefore many engineers neglected to implement the code in their designs (Wium and van Zijl, 2005). Due to this, unreinforced load bearing masonry buildings that were built before 1989 and some afterwards do not adhere to the design codes and are unsafe should a seismic event occur. These buildings have to be retrofitted to better withstand seismic events to ensure the safety of the occupants.

2.2 Unreinforced Masonry buildings

Steel structures and reinforced concrete structures perform reasonably well under seismic loading due to their ductile nature. Unreinforced masonry is a brittle material and therefore performs poorly under seismic loading.

2.2.1 Masonry Structures in Seismic zones

Unreinforced masonry buildings are at risk of collapse during seismic events, due to brittle failure and low resistance to shear and tension. There are three main reasons for human deaths during earthquakes, namely structural collapse, follow-on disasters, such as tsunamis, and non-structural causes (Coburn *et al.*, 1992). Of these three factors, structural collapse or damage to buildings are the primary cause of injury and casualties during an earthquake. It is responsible for 75% of deaths, and up to 90% if follow-on disasters are excluded. It was found that more than 50% of the structures that collapsed were masonry structures, while reinforced concrete (RC) and timber buildings were significantly less.

Figure 2.2 illustrates the typical diagonal shear-crack pattern that occurs in ULM buildings due to seismic events. The different failure mechanisms are discussed in Section 2.2.2.



(a) Two storey masonry building after an earthquake (Churilov and Dumova-Jovanoska, 2011).



(b) Multi-storey building after an earthquake. (Council *et al.*, 2003)

Figure 2.2: Damage to multi storey buildings due to earthquakes, are predominantly diagonal shear failure.

2.2.2 In-Plane Failure modes of ULM walls

According to Tomažević (1999) there are three typical in-plane failure modes for URM walls under seismic loading, namely sliding shear, diagonal shear and flexural failure; these modes of failure can be seen in Figure 2.3.

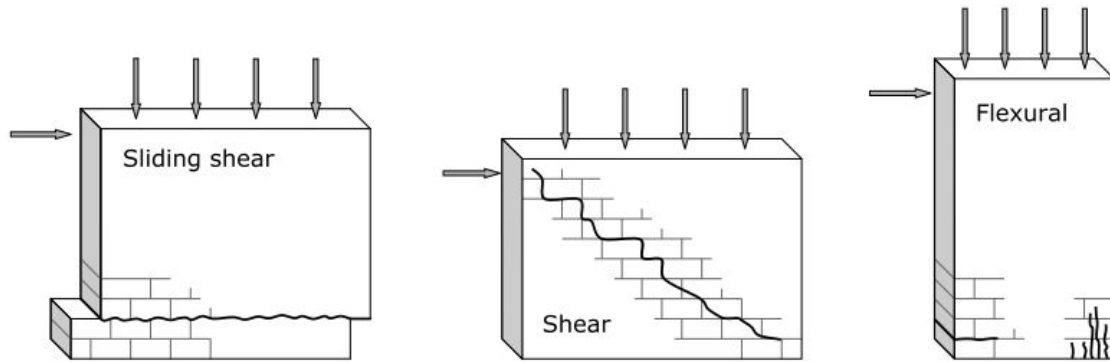


Figure 2.3: Failure modes of URM walls (Tomažević, 1999)

Sliding shear failure occurs when there is a low vertical load applied to the wall and/or the mortar is of poor quality. *Diagonal shear failure* occurs when the applied load, that can be in a combination of vertical and horizontal loads causes internal stresses that exceed the in-plane tensile and shear strength. This failure can pass through a combination of the masonry joints and the masonry units. This mode of failure is common under seismic loading. *Flexural failure* occurs when there is sufficient shear resistance and a high bending moment, as typically occurs in taller walls.

2.3 Previously researched/developed retrofitting techniques

Retrofitting refers to adding something to an already existing element in order to enhance or add certain favourable behaviour. In the case of this study, the in-plane shear resistance and the ductility of masonry walls need to be improved in order to better withstand seismic events. This has been done in various ways, as discussed in the following sections.

2.3.1 Near Surface Mounted reinforcements

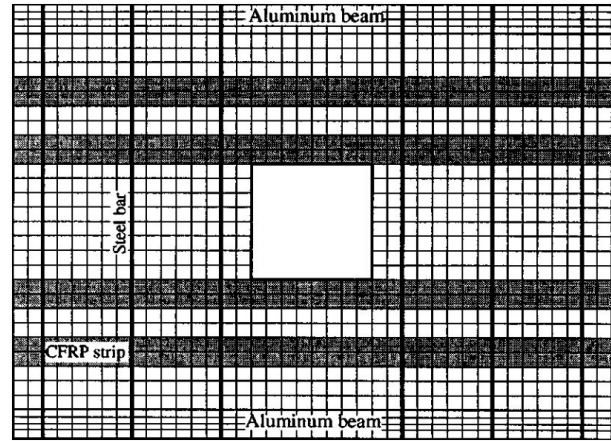
ElGawady *et al.* (2006) investigated the effect that near surface mounted (NSM) reinforcement overlay has on the lateral strength and ductility of 1600 x 730 mm masonry infill panels. Steel bars with a 4 mm diameter and a mesh size of 100 mm were fixed on either one or both sides of the masonry infill panel as seen in Figure 2.4(a). The total thickness of the shotcrete was kept constant at 40 mm. A cyclic loading was applied. The retrofitting increased the lateral strength of the masonry infill panel by a factor of 3. A more ductile behaviour was observed from the infill panels that were retrofitted on both sides. A disadvantage of NSM is that there was a significant amount of shotcrete run off, and the steel mesh is labour intensive to install. This results in NSM being a costly retrofitting method.

2.3.2 Carbon Fibre Reinforced Polymer strips

The effect carbon fibre reinforced polymer (CFRP) strips have on masonry infill panels was investigated by van Zijl and de Vries (2005) and is shown in Figure 2.4(b). The aim of the study was to preserve structural serviceability. The CFRP strips were glued to the masonry infill panel with a cement-based glue. CFRP strips successfully controlled the cracks despite being retrofitted only on the one side. However, cracks of about three times the size formed on the unreinforced side, in comparison to the reinforced side. The disadvantages of CFRP strips are that they can debond and serve no structural purpose, as well as being not aesthetically pleasing.



(a) Near Surface Mounted reinforcement (ElGawady *et al.*, 2006)



(b) Failure modes of URM walls (van Zijl and de Vries, 2005)

Figure 2.4: Retrofitting techniques for masonry infill panels.

2.3.3 Engineered Cement-based Composite overlays

Dehghani *et al.* (2015) conducted a study on the ability of fibre reinforced engineered cement-based composite (ECC) to increase the shear strength and energy absorption of masonry infill panels. The dimensions of the masonry panels were 450 mm x 450 mm x 105 mm, and the total ECC overlay thickness varied from 5 mm to 30 mm, single and double sided retrofitting. It was concluded that the shear strength increased by 1.5 to 2.8 times, and the energy absorption increased about 35 times. The failure mode shifted from brittle failure to pseudo-brittle failure, therefore the overlay added ductility to the masonry infill panel. No premature debonding occurred, implying there is a good bond between the ECC and the masonry substrate as no anchorage was provided.

Lin *et al.* (2014) also conducted studies on the effect ECC has on masonry wallettes. The masonry wallettes dimensions were 1200 mm x 1200 mm, and varied in thickness from 100 mm to 470 mm. The ECC overlay thickness applied varied from 10 mm to 50 mm, at 10 mm increments. The study concluded that the shear strength of the retrofitted masonry wallettes increased by 1.3 to 5.14 times. The in-plane ductility was increased by 2.2 on average. The effect of ECC decreased at triple leaf wallettes and larger, and the shear strength increase decreased with each added ECC layer.

2.3.4 Strain Hardening Cement based Composite bonded overlay

De Beer (2016) developed a sprayable cement-based composite (SHCC) mix that is based on the ECC mix done by Lin *et al.* (2014). SHCC increased the in-plane shear resistance by 4.65 for a single-leaf wall with a 30 mm overlay, and by 1.69 for a double-leaf wall with a 15 mm overlay. Further studies were done by De Jager (2018) that found a 100% increase in in-plane shear resistance, but no increase in ductility. The advantages of SHCC as a possible retrofitting solution is that SHCC is cost effective, non intrusive to the inhabitants, easy to apply and does not require highly skilled labour. The disadvantage is that additional measures have to be taken to increase the ductility as discussed in Section 2.8.2.

2.4 SHCC Material Properties

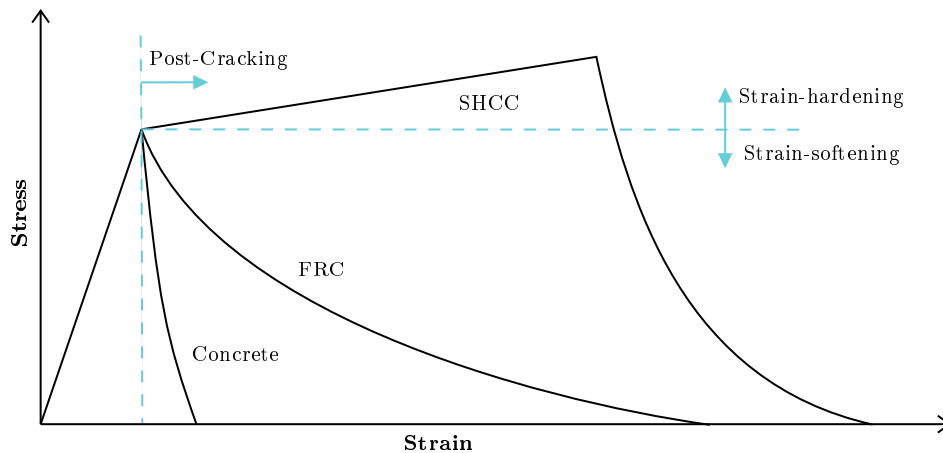
This section discusses the properties of previously developed SHCC that was cast into moulds, as this is standard practice for manufacturing structural elements. Sprayable SHCC is discussed in Section 2.5.

SHCC was designed to be able to withstand tensile loading and can undergo strains of 3% up to 6%,

in comparison to regular concrete with strains of 0.01%. It was observed that SHCC has an increase in strength post-cracking, as well as multiple cracking resulting in high energy absorption and higher ductility.

2.4.1 Tension

A schematization of how concrete, fibre reinforced concrete (FRC) and SHCC behaves under tension is illustrated in Figure 2.5. The three materials behave similarly before cracking, however post-cracking concrete has a brittle failure, FRC undergoes strain-softening, and SHCC has strain-hardening followed by strain-softening.



Note: In order to interpret the graph easier the strain up to the first crack point was magnified, as well as the post-cracking of the concrete.

Figure 2.5: Schematic illustration of tensile stress-strain comparison of Concrete, FRC and SHCC

Cracks form at the weakest point in the material matrix. If there are no fibres in the material matrix, the material fails, such as for normal concrete. For FRC the crack bridging capacity of the fibres is less than that of the concrete cracking strength. As the strain increases the crack widens and the load is reduced, therefore no multiple cracking occurs (Boshoff, 2007). In the case of SHCC, the fibres bridging the crack are able to sustain the load. Therefore as the strain increases the load also increases, the next crack will form at a point that is stronger than the first cracking point. This is a pseudo strain-hardening phenomenon. Strain-softening ultimately occurs when the load exceeds the crack bridging capacity of the fibres. A localized crack will form and strain-softening will start. Li *et al.* (2001) found that strain-hardening could occur at up to and exceeding 4% strain. The multiple cracking characteristic of SHCC results in the material having high ductility and toughness. There are two requirements for multiple cracking to occur (Lin and Li, 1997). Firstly, the fibre crack bridging capacity has to be larger than the cracking strength of the material matrix. Secondly, steady state cracking has to occur instead of unstable Griffith cracking that occurs in quasi brittle materials such as concrete.

The unloading and reloading behaviour of SHCC is important with regard to seismic loading. This behaviour was tested by Boshoff (2007) and is illustrated in Figure 2.6. As the tensile strain increases the stiffness reduces during loading and unloading, but it can still reach the ultimate stress and strain. This is an advantageous property of SHCC for seismic loading, as the ultimate stresses and strains are still reached in spite of the stiffness reduction. The fundamental period of the structure increases as the stiffness decreases, leading to lower base shear forces while energy is still being dissipated with each loading cycle.

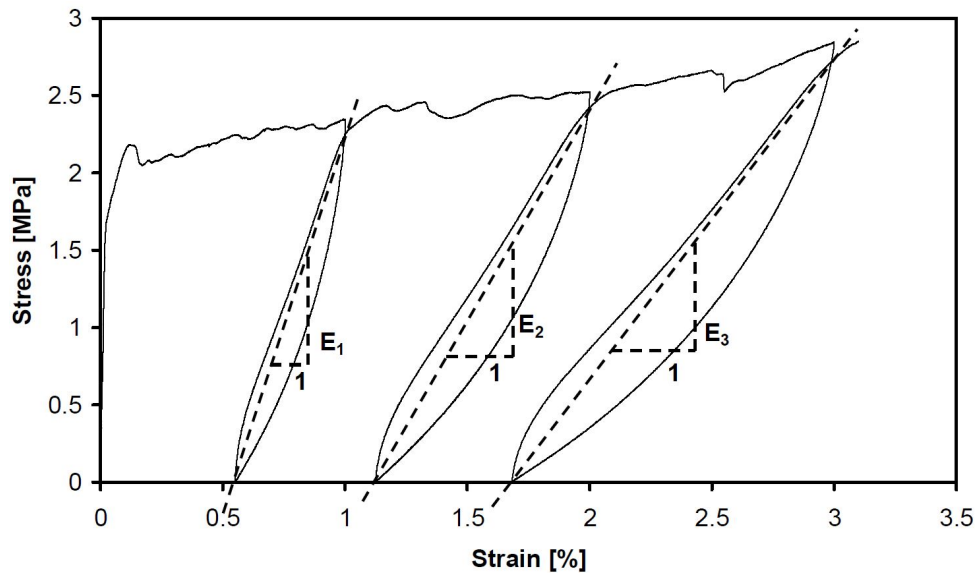


Figure 2.6: Unloading and reloading tensile behaviour Boshoff (2007)

2.4.2 Compression

The compression characteristics for SHCC is similar to that of concrete. The stresses are initially linear elastic, followed by post peak strain softening. Typical SHCC compressive strength ranges between 20 MPa and 40 MPa cube strength. The compressive strength is approximately 10 times the tensile strength (Visser, 2007).

2.4.3 Elastic Modulus

Studies done by Shang (2006) show SHCC to have an E-modulus of between 7 GPa and 10 GPa at 14 day strength. This is a relatively low E-modulus, and is mainly due to the relatively low amount of small aggregate content, the absence of large aggregate, and air entrapped in the SHCC mix. The E-modulus at 28 days was found to be double that of at 14 days. The E-modulus was determined by applying the secant method to the direct tensile tests.

2.4.4 Shear Behaviour

Studies done by Shang (2006) on SHCC found a ratio of 2.25 for ultimate shear strength to first cracking strength, and a ratio of 1.5 for ultimate shear strength to ultimate tensile strength. Multiple shear cracks form at an angle equal to or greater than 45° , these cracks are dominated by the principal stress directions. A possible reason for this is the strain-hardening property of SHCC in tension, which enables the reserve compression resistance to be utilized.

2.4.5 SHCC Material Matrix

SHCC and FRC consist of the same materials, namely water, fine aggregate, fibres, binder and chemical additives, but with different ratios. SHCC is an optimal combination of these materials to obtain ductile behaviour under tension. SHCC does not contain coarse aggregate as it negatively affects the ductile behaviour, and discourages even distribution of fibres. Admixtures are incorporated to ensure even distribution of the constituents to enhance fresh state behaviour, and is also advantageous to the hardened state.

Polyvinyl Alcohol (PVA) fibres were used in all research done at SUN that are related to SHCC. PVA fibres have high E-modulus (E) and tensile strength (f_t). Crack bridging fibres slip out as opposed to

breaking, as fibre breaking will lead to brittle failure instead of a ductile failure mechanism. Typical fibre lengths are 12 mm, but a fibre length of 8 mm was used to promote workability and pumpability. The shorter fibre length does not have an adverse negative influence on the ductility provided to the material matrix (De Beer, 2016). Fibre properties are listed in Table 2.1.

Table 2.1: Fibre Properties (Stander, 2007)

Type	E	$f_{t,f}$	$\epsilon_{u,f}$	Length	Diameter
	[GPa]	[GPa]	[%]	[mm]	[mm]
PVA-REC15	37	1.6	6	8	0.04

The binder used was a combination of Ordinary Portland Cement (OPC CEM I 52.5 N) and Fly Ash (FA) (De Beer, 2016). Adding admixtures changes either the fresh, early age and/or the hardened state of the mix to obtain certain advantageous properties. The admixtures that were used are Methyl Cellulose, that is a viscous agent, and a Superplasticiser. Fine silica sand with a maximum particle size of 0.2 mm was used; this is the same as in the research done by Paul (2015). It is important to use a fine aggregate as it aids in the strain-hardening properties of SHCC.

2.5 Spray-able SHCC development

De Beer (2016) developed SHCC that can be sprayed onto masonry through shotcrete. A small amount of Calcium Aluminate Cement (CAC) was used to obtain the ideal viscosity development rate. The SHCC developed can be sprayed onto masonry with little to no run-off, significant overlay thickness variability (10 mm - 60 mm), and aesthetically pleasing finishing after it is towelled.

2.5.1 Fresh Properties

For sprayable SHCC to be effective it should be cohesive enough to be pumped through the shotcrete machine without segregating, and viscous enough to adhere to the masonry once it is applied (Bruedern *et al.*, 2009; Kim *et al.*, 2003). CAC can be used to enhance the viscosity and cohesion of fresh SHCC. Two deformability tests were done by De Beer (2016), one without external vibration and one with external vibration in accordance to ASTM (2010). Deformability before (γ) and after (Γ) external vibration is calculated as in Equation 2.5.1, with $d_0 = 100$ mm in which d_1 is the maximum diameter and d_2 is the perpendicular diameter before external vibration. D_1 and D_2 are the same diameters after external vibration was added.

$$\gamma = \frac{(d_1 \times d_2) - d_0^2}{d_0^2} \quad (2.5.1)$$

Adequate cohesion and viscosity were found at a deformability of $\gamma < 0.3$ and $\Gamma < 1.3$, for an overlay thickness of up to 50 mm. At $\Gamma = 1.1$, the maximum thickness of 80 mm was achieved. However for $\Gamma < 1.1$ the SHCC could not be pumped as the workability was too low. De Beer (2016) found an optimal CAC dosage of 5% of Secar 51, with 51% alumina.

2.5.2 Hardened Properties

The only two tests that can determine the tensile strength of SHCC is the Direct Tensile Test (DTT), and the Uniaxial Tensile Test (UTT) (Boshoff, 2007). The main difference between the two tests is the shape of the specimens. The DTT has a cylindrical specimen and the UTT has a dumbbell shaped specimen. De Beer (2016) found that at a lower FA content a higher tensile strength was obtained, but the average ultimate tensile strain reduced. A FA to cement ratio of 140% was selected for its

high strain capacity, which is important for seismic resistance. The DTT results showed that the CAC percentage had no clear influence on the hardened properties of the SHCC. The properties that were tested with the DTT are the average tensile strength at first crack (\bar{f}_c), average ultimate tensile strength (\bar{f}_u), and average ultimate tensile strain capacity ($\bar{\epsilon}_u$). Both cast and sprayed specimens were tested and it was found that the sprayed specimens had overall lower resistance. The average ultimate tensile stress was 26.1% lower and the ultimate tensile strain was 32.1% lower than the cast specimens. The Young's Modulus for both were 15.26 GPa, as calculated using Equation 2.5.2, where σ_{tf} is the first crack stress, σ_0 is the pre-stress that is usually taken as 0.1 MPa, $\epsilon_{(\frac{1}{3}\sigma_{tf})}$ is the strain at σ_{tf} , and ϵ_0 is the strain at σ_0 .

$$E_{SHCC} = \frac{\frac{1}{3}\sigma_{tf} - \sigma_0}{\epsilon_{(\frac{1}{3}\sigma_{tf})} - \epsilon_0} \quad (2.5.2)$$

It was concluded that the average tensile strain of 2.26% for the sprayed samples was sufficient. The final mix design that De Beer (2016) used is given in Table 2.2.

Table 2.2: SHCC mix properties

Cement	Fly ash	CAC	Sand	Water	Fibre	SP	VMA	Total
420	620	21	540	365	2%	2.2	0.8	1995 kg/m^3

2.5.3 Shrinkage

De Beer (2016) tested the effect shrinkage would have on the SHCC overlay and whether or not debonding would occur due to shrinkage. It was concluded that restrained shrinkage does not have a detrimental effect on the SHCC overlays bonded to the masonry wall. No debonding between the SHCC overlay and the masonry substrate was observed as well as no localized cracks in the SHCC overlay, unlike in normal mortars (Chilwesa, 2012; Beushausen and Chilwesa, 2013).

2.6 Finite Element Analysis in Diana

It is important to have a extensive understanding of the structure that needs to be modelled and the software that is used for the modelling, namely Diana 10.2. The basic finite element problem is as in Equation 2.6.1, where $\{F\}$, and $\{F_o\}$ are the reaction force and applied force respectively, and $[K]$ and $\{d\}$ are the stiffness and displacement of the structure respectively.

$$\{F\} - \{F_o\} = [K]\{d\} \quad (2.6.1)$$

2.6.1 Crack Modelling

There are two different methods to model cracks in Diana, discrete and smeared (DIANA FEA BV, 2006).

The *discrete crack* model is a crack modelled directly by separating the mesh elements with a geometric discontinuity. This is a difficult and computer intensive approach to crack modelling.

The *smeared crack* model models the crack distributed over the element with anisotropic characteristics. There are three different ways to implement this in Diana. (a) Rots' Element Based Method (Rots, 1988), the crack bandwidth h is dependent on the element size, shape and the type of interpolation

function that is used. For two dimensional elements $h = \sqrt{2A}$, or $h = \sqrt{A}$, for low order and higher order interpolation respectively, where A is the area of the element. (b) Govindjee's Projection Method (Govindjee *et al.*, 1995), the crack bandwidth h is the projected length of the element containing the crack, whereby this method takes into account the element size, crack orientation, and element aspect ratio. (c) Direct Input, the crack bandwidth h can be entered directly by the user to guide the algorithm program.

The smeared crack model with Rots' method was used as it is not computationally intensive.

2.6.2 Materials

There are various different material models available in Diana. For this study the Rankine-Hill material model was considered for the masonry. For SHCC the Rankine-Rankine model, i.e. Total Strain Based material model was used. All the information in this section was obtained from DIANA FEA BV (2006) unless stated otherwise.

2.6.2.1 Rankine-Hill

The Rankine-Hill material model has tension softening, and compression hardening followed by softening characteristics, as illustrated in Figure 2.7. The Hill type yield surface provides the compression hardening characteristic, meaning that as the external force/stress increase, the resistance increases as well .

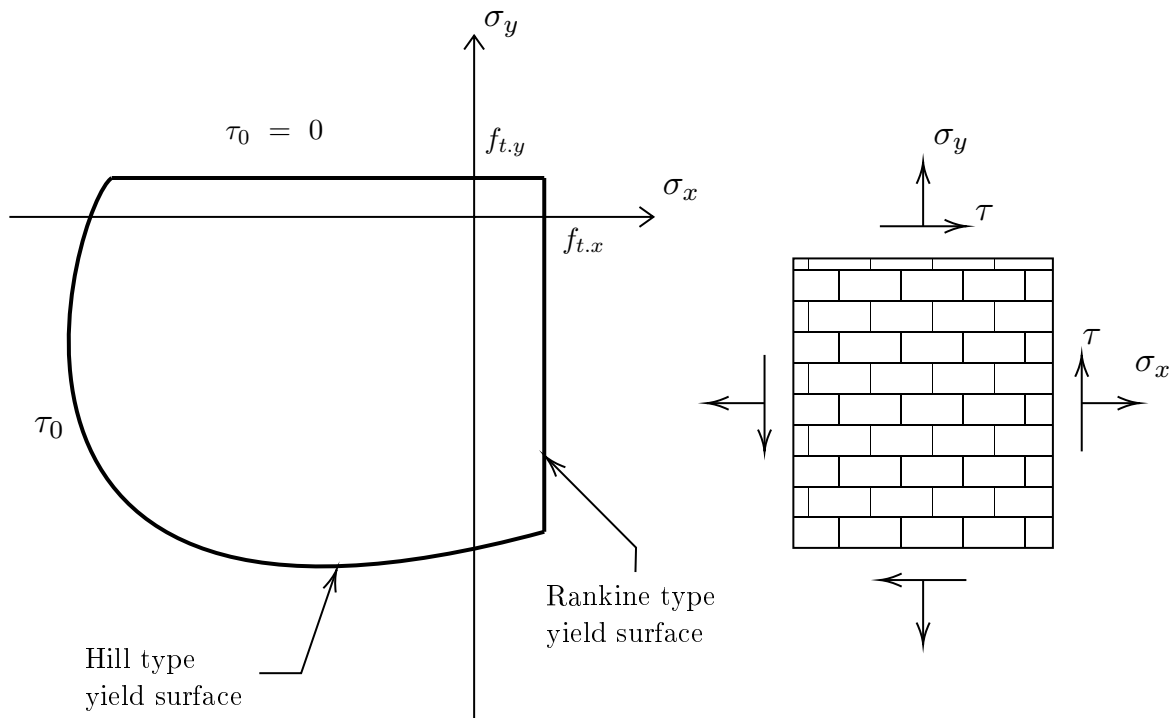


Figure 2.7: Rankine-Hill yield condition

The original Rankine yield criterion produces numerical complications with the undefined gradients for the yield surface. The original yield type is replaced by a hyperbola, as in Equation 2.6.2, with asymptotes at $\sigma_x = f_{tx}$ and $\sigma_y = f_{ty}$. The parameter μ describes the distance from the hyperbola to the asymptotes, as in Figure 2.8.

$$f_{hyp} = \sqrt{\frac{1}{2}\xi^T P_t \xi + \mu^2 + \frac{1}{2}\pi^T \xi} \quad (2.6.2)$$

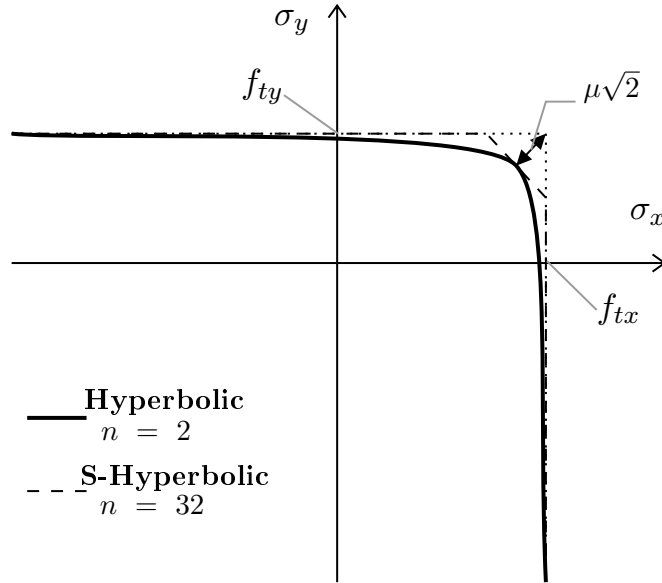


Figure 2.8: Rankine tension yield approximation

But by using this hyperbolic function, the uniaxial tension in the x direction is not perpendicular to the original Rankine yield type criterion. This induces compression stresses in the y direction. Equation 2.6.2 can be adjusted to a super-hyperbola as in Equation 2.6.3. Where $\xi_x = \sigma_x - \sigma_{t.x}$ and similarly, $\xi_y = \sigma_y - \sigma_{t.y}$.

$$f_{shyp} = \frac{\xi_x + \xi_y}{2} + \sqrt{\left(\left(\frac{\xi_x + \xi_y}{2}\right)^n + \mu^n\right)^{2/n} + \alpha\tau_{xy}^2} \quad (2.6.3)$$

Only the range of σ_x and σ_y is influenced by n , that also influences the apex rounding. A residual tensile strength in both directions of $5\mu/2$ is chosen. This is because the tensile strength cannot be equal to zero due to tension softening. μ can be calculated as in Equation 2.6.4, where μ_{tol} is predefined by the user.

$$\mu = \frac{2\mu_{tol}}{5} \min(f_{tx}, f_{ty}) \quad (2.6.4)$$

The parabolic hardening and softening compression curves are illustrated in Figure 2.9. The equations for the respective curves are given in Equations 2.6.5 to 2.6.7. Isotropic hardening is assumed up to peak strength at the plastic strain (κ_p). However the compression softening is governed by the respective orthogonal fracture energy, $G_{f_{c.i}}$. Fracture energy is the amount of energy released per area of crack surface formed. Computationally, the fracture energy determines the rate of the reduced resistance as the crack widens, in continuum description distribution over a crack band. All of the stresses are in terms of $\sigma_{c.i}$, and are as follows: $\sigma_{m.i} = \frac{1}{2}\sigma_{c.i}$, $\sigma_{i.i} = \frac{1}{3}\sigma_{c.i}$ and $\sigma_{r.i} = \frac{1}{7}\sigma_{c.i}$. It is important to note that $\sigma_{r.i}$ is different in Diana than that of the original derivation by Lourenco (1996) where $\sigma_{r.i} = \frac{1}{10}\sigma_{c.i}$.

$$\sigma_{1i}(\kappa_c) = \sigma_{i.i} + (f_{c.i} - \sigma_{i.i}) \sqrt{\frac{2\kappa_c}{\kappa_p} - \frac{\kappa_c^2}{\kappa_p^2}} \quad (2.6.5)$$

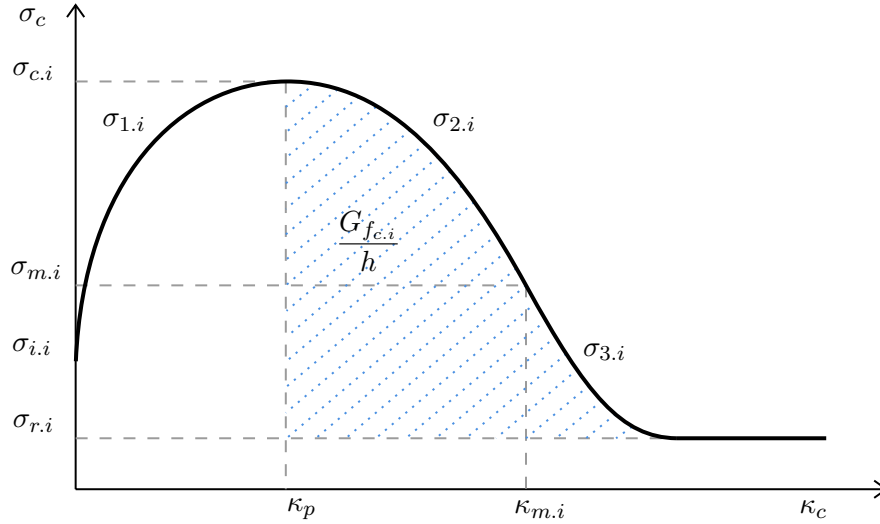


Figure 2.9: Hardening Softening law of Hill behaviour

$$\sigma_{2,i}(\kappa_c) = f_{c,i} + (\sigma_{m,i} - f_{c,i}) \left(\frac{\kappa_c - \kappa_p}{\kappa_{m,i} - \kappa_p} \right)^2 \quad (2.6.6)$$

$$\sigma_{3,i}(\kappa_c) = \sigma_{r,i} + (\sigma_{m,i} - \sigma_{r,i}) \exp \left(2 \left(\frac{\sigma_{m,i} - f_{c,i}}{\kappa_{m,i} - \kappa_p} \right) \left(\frac{\kappa_c - \kappa_{m,i}}{\sigma_{m,i} - \sigma_{r,i}} \right) \right) \quad (2.6.7)$$

The plastic strain ($\kappa_{m,i}$) is calculated in Equation 2.6.8. Provided that the condition in Equation 2.6.9 is met, this is to avoid snap-back and a reduction in the strength limit, $\sigma_{c,i}$.

$$\kappa_{m,i} = \frac{75}{67} \frac{G_{f_{c,i}}}{h f_{c,i}} + \kappa_p \quad (2.6.8)$$

$$\kappa_{m,i} \geq \frac{f_{c,i}}{E_i} + \kappa_p \quad (2.6.9)$$

The h in Equation 2.6.8 and Figure 2.9, is the equivalent element size. It has an upper limit given in Equation 2.6.10, to ensure that compression in the material is calculated accurately. The equivalent element size can be calculated in terms of the element area, A_e , as $h = \alpha_h \sqrt{A_e}$, where α_h is equal to $\sqrt{2}$ for linear elements and 1 for quadratic elements.

$$h \leq \frac{G_f E}{f_t^2} \quad (2.6.10)$$

This material model was selected by De Jager (2018) to model the masonry as it accounts for the elastic and inelastic orthotropy of the masonry walls.

2.6.2.2 Rankine-Rankine

The Rankine-Rankine material model, also referred to as the Total strain based crack model in Diana, is a smeared approach for the fracture energy. The Poisson effect is not taken into account at a cracked state, as it no longer exists.

The tension behaviour can be modelled in various different ways, all are related to crack bandwidth. The functions based on fracture energy are the linear softening curve, exponential softening curve, as in Figure 2.10, non linear softening curve according to Hordijk (1991), the European CEB-FIP Model Code (du Béton, 1993), fib Model Code for Concrete structures (Taerwe *et al.*, 2013), and

Japan Society of Civil Engineers (JSCE, 2010). The tension behaviour functions that are not related to fracture energy are the constant tensile behaviour, brittle behaviour, linear behaviour based on ultimate strain, multi-linear behaviour, tensile failure mode for FRC, non-linear behaviour based in ultimate strain (Ferreira, 2013), multi-linear behaviour based in relative total displacement and general user-supplied function.

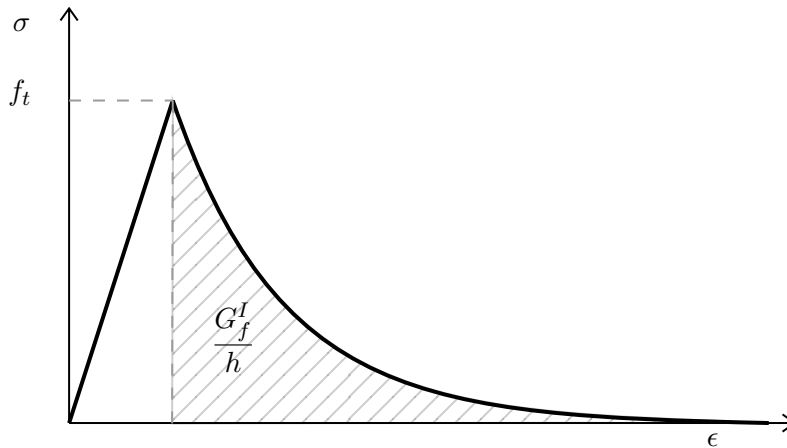


Figure 2.10: Exponential Tension softening curve for the Total Strain crack model

The predefined compression curves in Diana are the constant, brittle, linear hardening, saturation hardening, Thorenfeldt (1987) and the parabolic curve.

The Rankine-Rankine material model was selected to model the SHCC as it gives the best representation of the behaviour of SHCC and the tension-hardening behaviour was captured by defining a high fracture energy (De Jager, 2018).

2.6.2.3 Coulomb Friction Interface

Behaviour on the interface between parts of a masonry structure is mostly governed by friction between the parts. The Coulomb friction interface describes the total relative displacement rate between two parts and can be reversible or irreversible. The material model can be described by the yield and plastic potential surface. The Coulomb friction criteria are illustrated in Figure 2.11, where c is the cohesion, ϕ the friction angle, f_t the tensile strength, t_t the tangent traction and t_n the normal traction. The dilatancy angle (ψ) defines the increment in plastic volumetric strain per plastic deviatoric strain increment, i.e. the rate of plastic volume increase upon plastic shearing in the Mohr-Coulomb model and is comparable to the friction angle.

2.6.3 Mesh Elements

For plane analysis Diana offers mainly two types of mesh element, namely triangular and quadrilateral elements, as illustrated in Figure 2.12. The interpolation order can be linear or quadratic as illustrated in Figure 2.13. It is important to select the correct mesh size. Elements that are too large can overestimate the model stiffness and elements that are too small cause the model to be computationally intensive without adding new information. To avoid this a mesh dependency analysis has to be done. The material model may also constrain the mesh size as discussed for the Rankine-Hill model in Section 2.6.2.1.

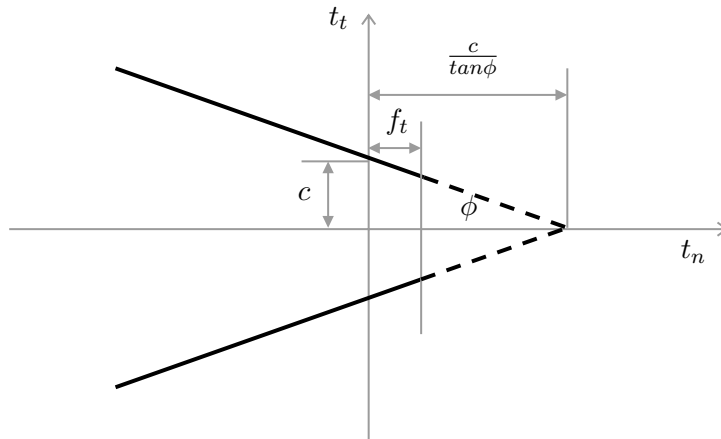
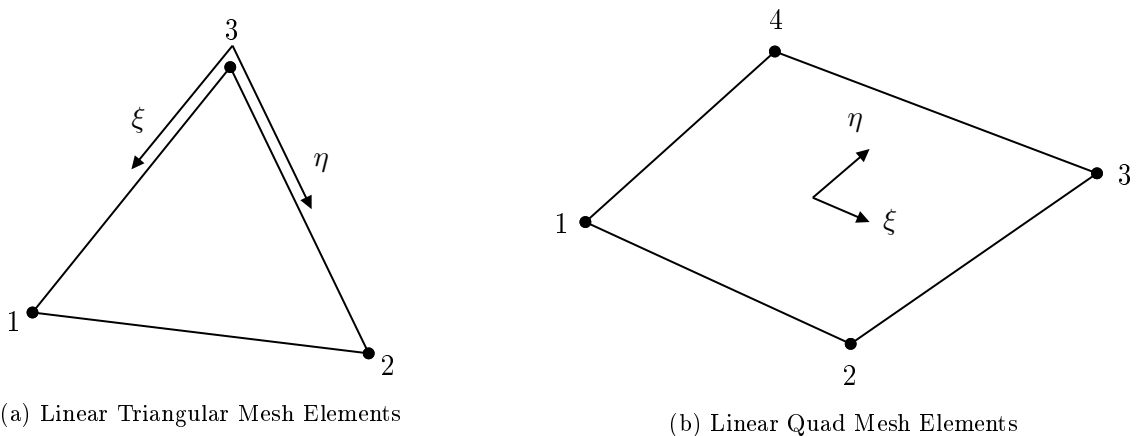


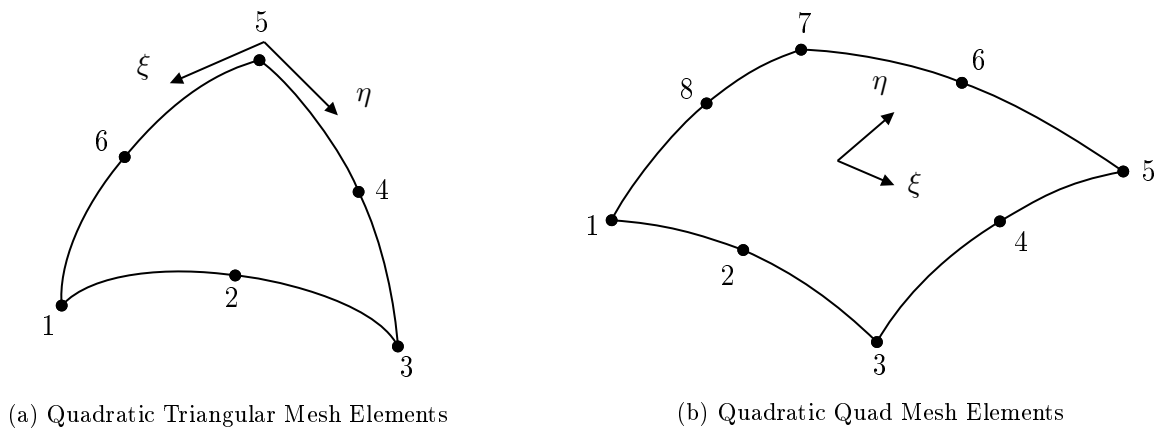
Figure 2.11: Coulomb friction criteria



(a) Linear Triangular Mesh Elements

(b) Linear Quad Mesh Elements

Figure 2.12: Linear Mesh Elements



(a) Quadratic Triangular Mesh Elements

(b) Quadratic Quad Mesh Elements

Figure 2.13: Quadratic mesh elements

2.6.4 Interface

An interface element is an element between two other elements that have geometric and material properties. The interface elements describe how two elements are connected to one another. Figure 2.14 illustrates the interface element between two quadratic triangular elements.

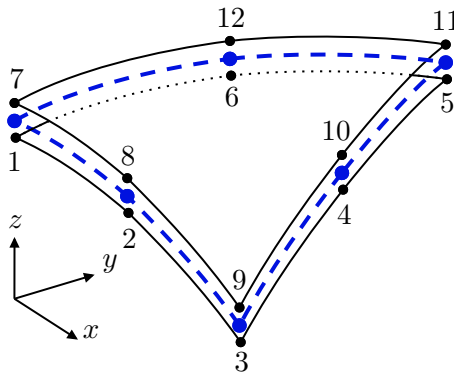


Figure 2.14: Quadratic Triangular Interface element

2.6.5 Modelling Approach

There are three types of masonry modelling approaches namely micro, meso and macro modelling. With micro modelling a masonry wall is modelled as the bricks, the mortar and and interface between the bricks and mortar. A meso approach is a simplified micro model, where bricks are modelled as elastic elements and the mortar is modelled as the interface between the bricks. For a macro model the characteristics of the bricks and mortar are represented by each element. These three models are illustrated in Figure 2.15.

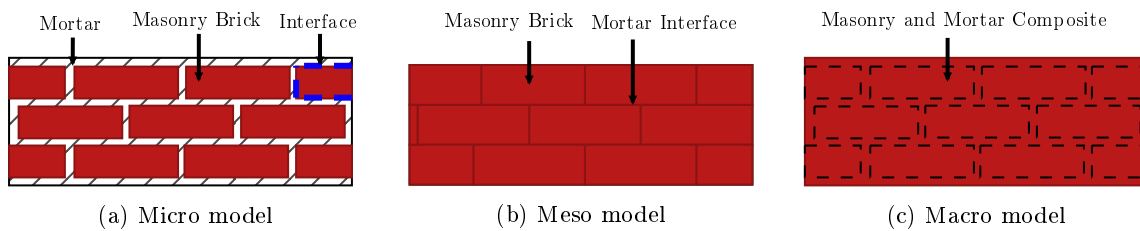


Figure 2.15: Different modelling approaches

The macro model was selected by De Jager (2018). Although this model does not capture the detailed failure mechanisms, it is sufficient to capture the global failure of the masonry walls. The macro model is also advantageous for larger scale models.

2.6.6 Non-linear Analysis

When there is no longer a linear relationship between the force and displacement vectors, a non-linear analysis procedure is required. In a non-linear analysis an incremental-iterative approach is followed. Equilibrium has to be reached within each increment, i.e. the internal forces must equal the external forces ($\vec{f}_{int} = \vec{f}_{ext}$). Residual, or 'out-of-balance' forces (\vec{g}), as calculated in Equation 2.6.11, can occur with each increment. The increment will continue to iterate until the residual forces are zero, or within a certain tolerance, where $\Delta\vec{u}$ is the incremental displacement.

$$\vec{g}(\Delta\vec{u}) = \vec{f}_{ext}(\Delta\vec{u}) - \vec{f}_{int}(\Delta\vec{u}) \quad (2.6.11)$$

Figure 2.16 illustrates the general iteration process.

2.6.6.1 Solution Method

There are various ways to solve Equation 2.6.1. The solution methods in Diana consist of Direct and Iterative solution methods. The Parallel Direct Sparse Solver was used in the analysis done by De Jager

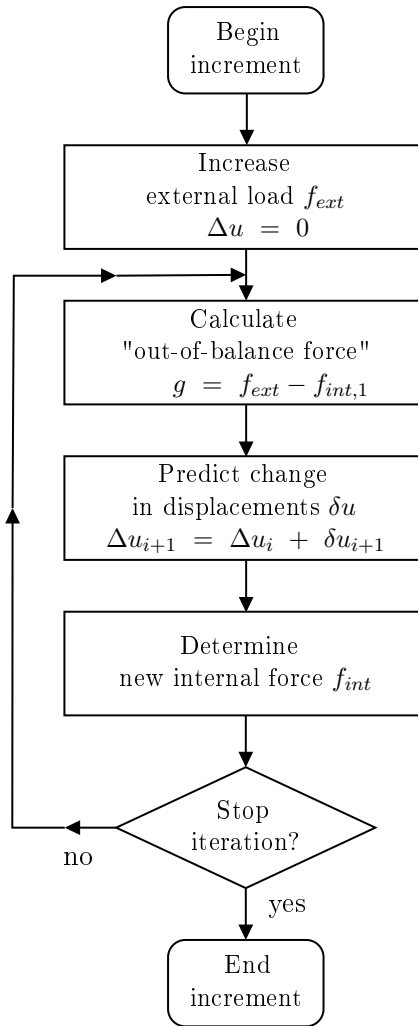


Figure 2.16: Iteration Process

(2018) due to its computational efficiency when solving large sparse symmetric and un-symmetric linear system of equations. Other available solution methods in Diana is the Sparse Cholesky, Factorization and Fill-in and various iterative solution methods.

2.6.6.2 Iterative Procedures

Due to lack of equilibrium in an increment, a pure incremental solution can lead to inaccurate solutions, unless the step sizes are very small. To minimize the inaccuracies an iterative process is used. In an iterative solution the displacement increment ($\Delta\vec{u}$), is computed in a series of iterative increments ($\delta\vec{u}$) until equilibrium is reached within a prescribed tolerance. The incremental displacement is as in Equation 2.6.12.

$$\Delta\vec{u}_{i+1} = \Delta\vec{u}_i + \delta\vec{u}_{i+1} \quad (2.6.12)$$

The main difference between the different iteration procedures is the way in which the incremental displacement ($\delta\vec{u}$) is calculated. The stiffness matrix, \mathbf{K} , represents some linearised relation between the force and displacement vectors. The stiffness matrix is formulated differently for each procedure and can change in every iteration. The iterative increments can be derived directly by the symbolic Equation 2.6.13, where \vec{g}_i is the residual force at the start of the increment i .

$$\delta\vec{u}_i = \mathbf{K}_i^{-1}\vec{g}_i \quad (2.6.13)$$

Diana has various iterative procedures, namely *Newton-Raphson*, *Quasi-Newton*, *Linear* and *Constant Stiffness*.

The *Newton-Raphson* method has two sub-methods, regular and modified. The difference between the two methods is the point at which the tangential stiffness matrix \mathbf{K}_i , as in Equation 2.6.14, is calculated.

$$\mathbf{K}_i = \frac{\partial \vec{g}}{\partial \Delta \vec{u}} \quad (2.6.14)$$

For the *Regular Newton-Raphson* method, the stiffness in Equation 2.6.14 is calculated for each iteration, even if equilibrium has not been reached. A visual representation of this is illustrated Figure 2.17(a). The method converges within a few iteration steps, but is computationally intensive as the stiffness matrix has to be calculated and Equation 2.6.13 solved for each iteration. The method is also prone to fail due to divergence.

The *Modified Newton-Raphson* method calculates the stiffness in Equation 2.6.14 only at the start of each increment. Therefore the stiffness is always based on an equilibrium state. The method takes more steps as illustrated in Figure 2.17(b), but the iterations are computed faster.

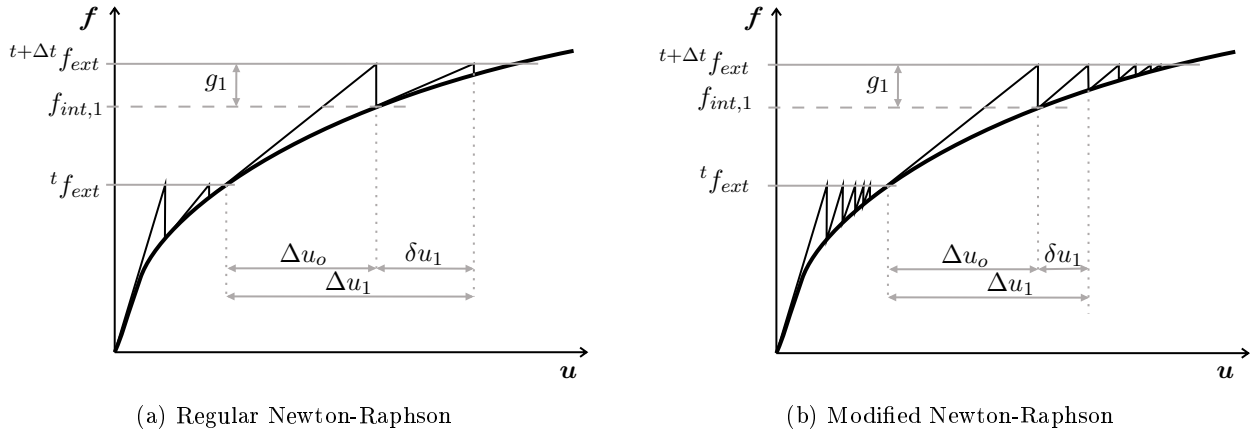


Figure 2.17: Newton-Raphson

The *Quasi-Newton* or *Secant* method calculates the stiffness as in Equation 2.6.15. Where the change in residual force vector is calculated as in Equation 2.6.16. This is illustrated in Figure 2.18.

$$\mathbf{K}_{i+1} \delta \vec{u}_i = \delta \vec{g}_i \quad (2.6.15)$$

$$\delta \vec{g}_i = \vec{g}_{i+1} - \vec{g}_i \quad (2.6.16)$$

Equation 2.6.13 is then used to calculate the next iterative increment. For multi-degree of freedom systems the secant stiffness matrix is not unique. The *Broyden*, *Broyden-Fletcher-Goldffard-Shanno* (BFGS) and *Crisfield* secant methods are implemented in Diana.

In case the previous methods become unstable or certain desirable characteristics need to be retained the *Linear* and *Constant* methods can be used.

The *Linear Stiffness* method uses an initial stiffness matrix throughout the whole iteration process. The stiffness matrix also remains symmetric, unlike the tangential stiffness matrix. It is however slow to converge and can become unstable after bifurcations.

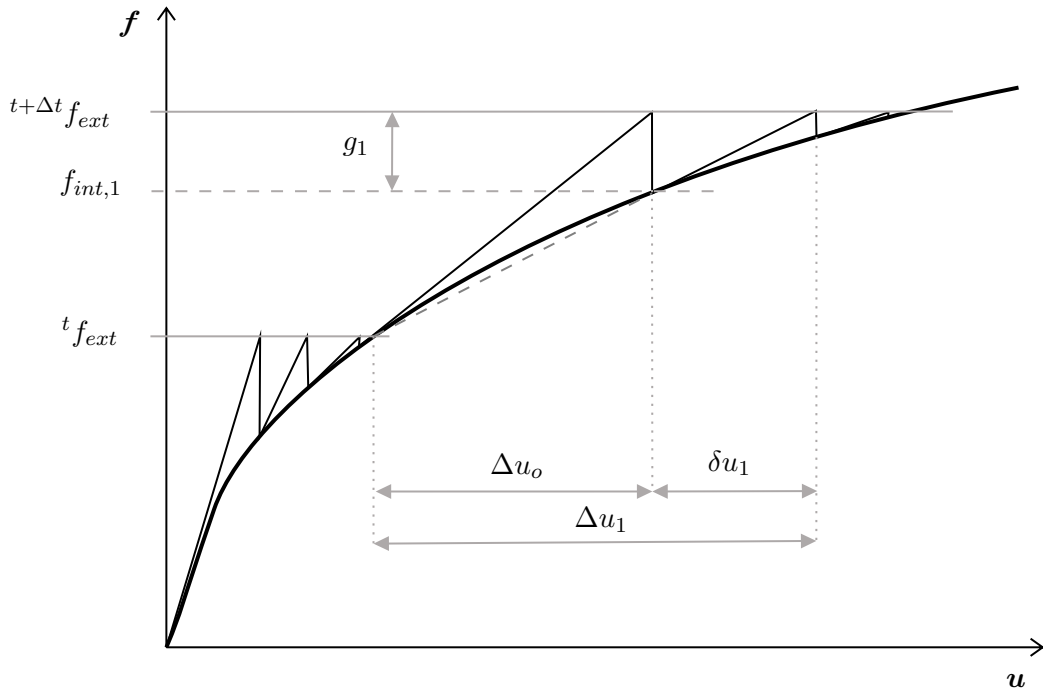


Figure 2.18: Quasi-Newton (Secant) iteration

The *Constant Stiffness* method follows up on Newton-Raphson or the Secant method and uses the last calculated stiffness matrix. This may be used when the methods have failed or can be in different phases.

2.6.6.3 Incremental Procedures

Incremental Procedures determine the step size of each increment. These procedures consists of *Load*, *Displacement* and *Arc-length* controlled.

The *Load Controlled* procedure is when the load is incrementally applied at the start of each increment and the displacements are calculated. This procedure can over-predict the displacements. *Displacement Control* is used when displacements are prescribed and applied incrementally. If the load displacement curve becomes almost horizontal the displacement steps can become very large. Figure 2.19 illustrates the Load and Displacement procedures.

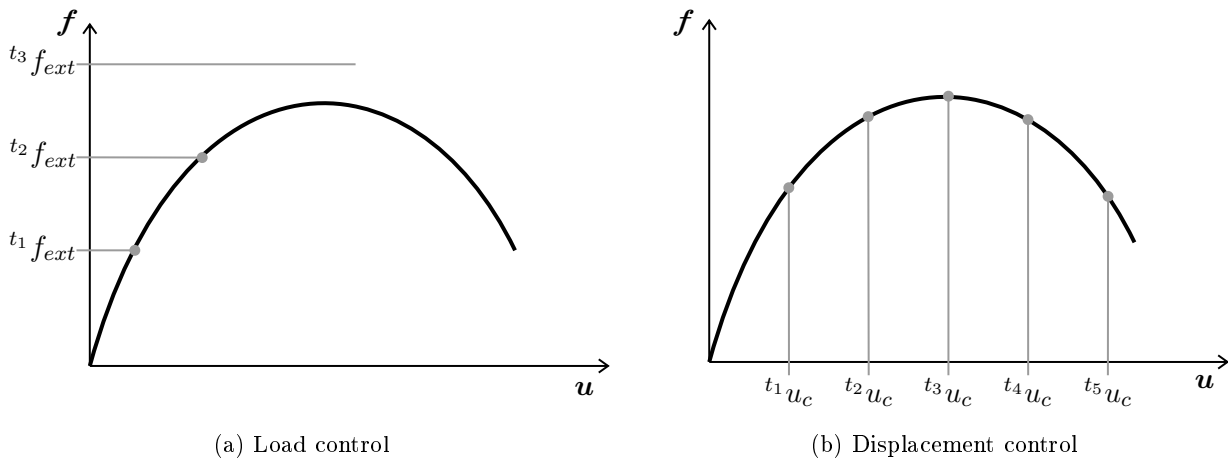


Figure 2.19: Load and Displacement control

Arc-Length Controlled procedures adapt the increment size in order to limit the norm of the displacement increment. The problems that arise from the load and displacement controlled increments can be overcome by the Arc-Length controlled increment. This method is able to analyse the *snap-through* behaviour as in Figure 2.20(a), as well as the *snap-back* behaviour in Figure 2.20(b), that the displacement control fails to analyse.

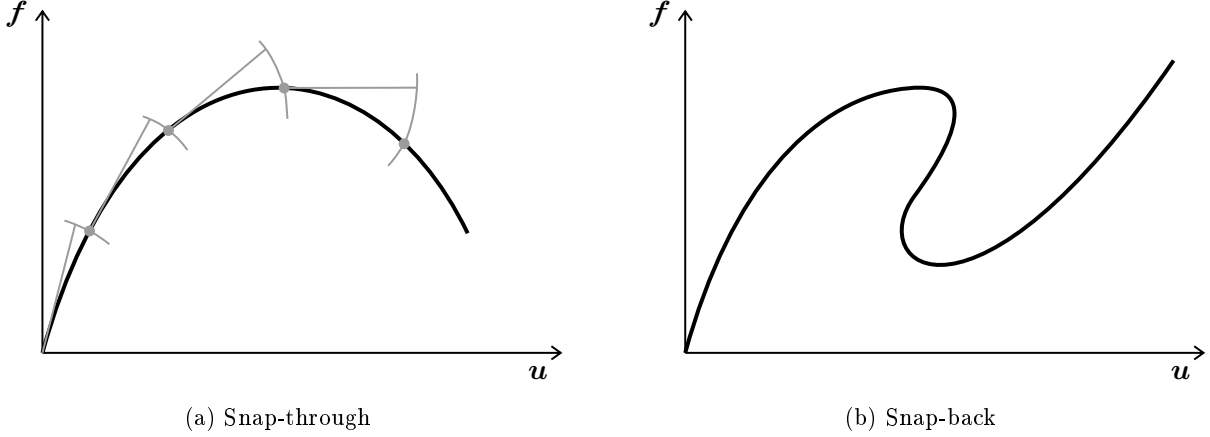


Figure 2.20: Arc-length control

2.6.6.4 Convergence Criteria

Convergence Criteria are norms that are used to determine when the iterative procedure has reached a satisfactory equilibrium state. If the maximum number of iterations is exceeded or divergence occurs, the iteration process will be terminated. The divergence and convergence detections are based on the same norms. The user specifies the tolerance value of the chosen convergence norm. It is important that the specified tolerance is within reasonable bounds. A tolerance that is too large will lead to divergence from the equilibrium path and deliver inaccurate results, too small tolerance will result in too many steps being taken to reach equilibrium. The convergence criteria available in Diana are the *Force*, *Displacement*, *Energy* and *Residual Norms*. The items used for these norms are specified in Figure 2.21.

Force Norm measures the ratio of the iteration out-of-balance force relative to the initial imbalanced force as in Equation 2.6.17. This convergence norm can avoid unnecessary iterations by detecting convergence right away, due to the reference norm being known before the displacements are predicted.

$$\text{Force norm ratio} = \frac{\sqrt{\vec{g}_i^T \vec{g}_i}}{\sqrt{\vec{g}_0^T \vec{g}_0}} \quad (2.6.17)$$

The *Displacement norm* measures the ratio of the iteration displacement increment relative to the initial displacement increment by using Equation 2.6.18. One additional iteration is necessary to check convergence.

$$\text{Displacement norm ratio} = \frac{\sqrt{\delta \vec{u}_i^T \delta \vec{u}_i}}{\sqrt{\Delta \vec{u}_0^T \Delta \vec{u}_0}} \quad (2.6.18)$$

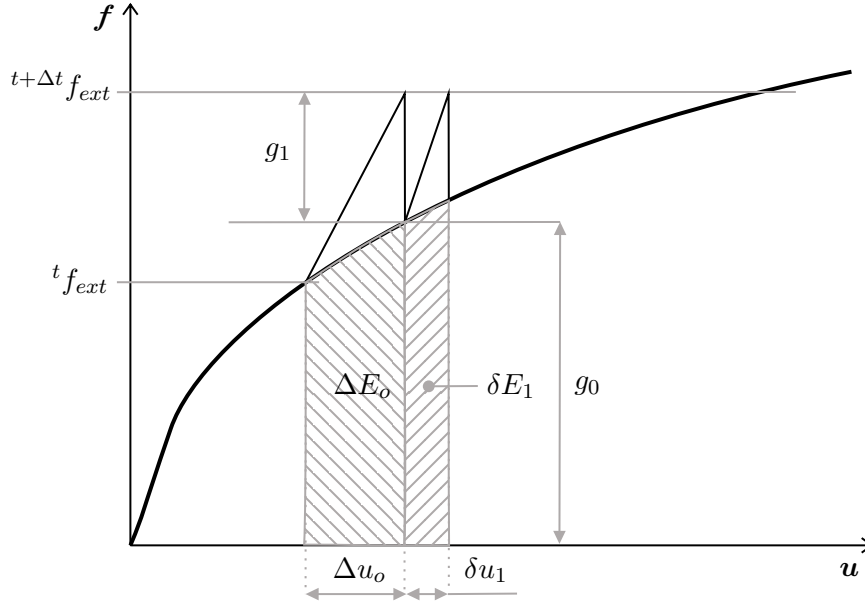


Figure 2.21: Norm Items

Energy norm takes into account the internal forces and relative displacements. It is calculated as in Equation 2.6.18. The energy norm also requires one additional iteration to test for convergence.

$$\text{Energy norm ratio} = \left| \frac{\delta \vec{u}_i^T (\vec{f}_{int,i+1} + \vec{f}_{int,i})}{\Delta \vec{u}_0^T (\vec{f}_{int,1} + \vec{f}_{int,0})} \right| \quad (2.6.19)$$

Residual norm takes the prescribed boundary conditions into account, unlike the Force norm which does not. Equation 2.6.20 is used to calculate the Residual norm, where \vec{g}_n is the residual forces from the previous step's last iteration. This is taken as zero for the first step in Diana.

$$\text{Residual norm ratio} = \frac{\left| \sqrt{\vec{g}_i^T \vec{g}_i} - \sqrt{\vec{g}_{i-1}^T \vec{g}_{i-1}} \right|}{\left| \sqrt{\vec{g}_0^T \vec{g}_0} - \sqrt{\vec{g}_n^T \vec{g}_n} \right|} \quad (2.6.20)$$

2.7 Modal Analysis

All the information in this section was obtained from Strasheim *et al.* (2018). Modal analysis is the response of a structure under no external dynamic loading. The aim of a modal analysis is to find the modes shapes, and eigenfrequencies of a structure, should it be displaced and released to oscillate freely.

For a linear multi degree of freedom system, the dynamic equilibrium equation is as in Equation 2.7.1. Where $[M]$, $[C]$ and $[K]$ are the mass, damping and stiffness matrices respectively, $\{f\}$ is the force vector and, $\{x\}$, $\{\dot{x}\}$ and $\{\ddot{x}\}$ are the displacement, velocity and acceleration vectors respectively.

$$[M] \cdot \{\ddot{x}\}(t) + [C] \cdot \{\dot{x}\}(t) + [K] \cdot \{x\}(t) = \{f\}(t) \quad (2.7.1)$$

Due to no external force being applied for a modal analysis, and if damping is neglected, Equation 2.7.1 can be simplified into:

$$[M] \cdot \{\ddot{x}\}(t) + [K] \cdot \{x\}(t) = \{0\} \quad (2.7.2)$$

To solve Equation 2.7.2, it is assumed that the response is in the form of $\{u\}(t) = \{\tilde{u}\}e^{i\omega t}$. Substituting this simplifies Equation 2.7.2 to:

$$([K] - \omega^2[M]) \cdot \{\tilde{u}\} = \{0\} \quad (2.7.3)$$

The only solution that will result in $\{\tilde{u}\}$ being non zero is if

$$\det([K] - \omega^2[M]) = 0 \quad (2.7.4)$$

Therefore the eigenvalues (ω) can be solved, as well as the eigenvectors accompanying each eigenvalue, this gives the mode shapes of the structure. The nodal displacements can be obtained from the mode shapes, and from the displacements the reaction forces, stresses and other results can be obtained.

Equation 2.7.5 is used to calculate the displacements at each degree of freedom (DOF), where u_n is the displacement, f_n^* is the normalized applied force, k_n^* is the normalized stiffness vector, n refers to the number of the DOF.

$$u_n = \frac{f_n^*}{k_n^*} \quad (2.7.5)$$

The normalized applied force is calculated as in Equation 2.7.6, where $\{\phi_n\}$ is the normalized eigenvectors for each mode, $m_{n,eff}^*$ is the effective modal mass and A_d is the accidental load.

$$f_n^* = \{\phi\}_n \cdot m_{n,eff}^* \cdot \{A_d\} \quad (2.7.6)$$

The effective modal mass and normalized mass is calculated as in Equation 2.7.7 and 2.7.8 respectively.

$$m_{n,eff}^* = \Gamma_n^2 m_n^* \quad (2.7.7)$$

$$\Gamma_n^2 = \frac{\{\phi_n\}^T [M] \{\iota\}}{\{\phi_n\}^T [M] \{\phi_n\}}$$

$$m_n^* = \{\phi_n\}^T [M] \{\phi_n\}$$

$$k_n^* = \{\phi_n\}^T [K] \{\phi_n\} \quad (2.7.8)$$

2.8 Previous Research on SHCC as a Retrofitting Technique

As discussed in Section 2.1, there is a need to retrofit ULM buildings to better withstand seismic events. A possible solution is to retrofit these buildings with SHCC. The effect SHCC has on masonry walls was tested by De Beer (2016), the experimental setup that was used is illustrated in Figure 2.22. The setup consists of the masonry wall (1150 mm x 935 mm) supported by concrete beams at the top and bottom. The steel beam on top is used to distribute the load induced by rods on both sides of the steel beam. The forces induced by the rods are to represent loads of upper stories. A rod pair

was placed in the middle of the beam and two rod pairs are at the end of the beam as illustrated in Figure 2.22. The force in the middle rod pair was kept constant by the coil while the forces in the two end rod pairs were increased as the displacement increased. The force increase in the last two rod pairs was necessary to ensure shear failure. The shear resistance of the masonry wall was measured at the point where the steel beam was incrementally displaced. A total displacement of 10 mm and 20 mm was applied to the masonry wall, and the masonry retrofitted with SHCC respectively.

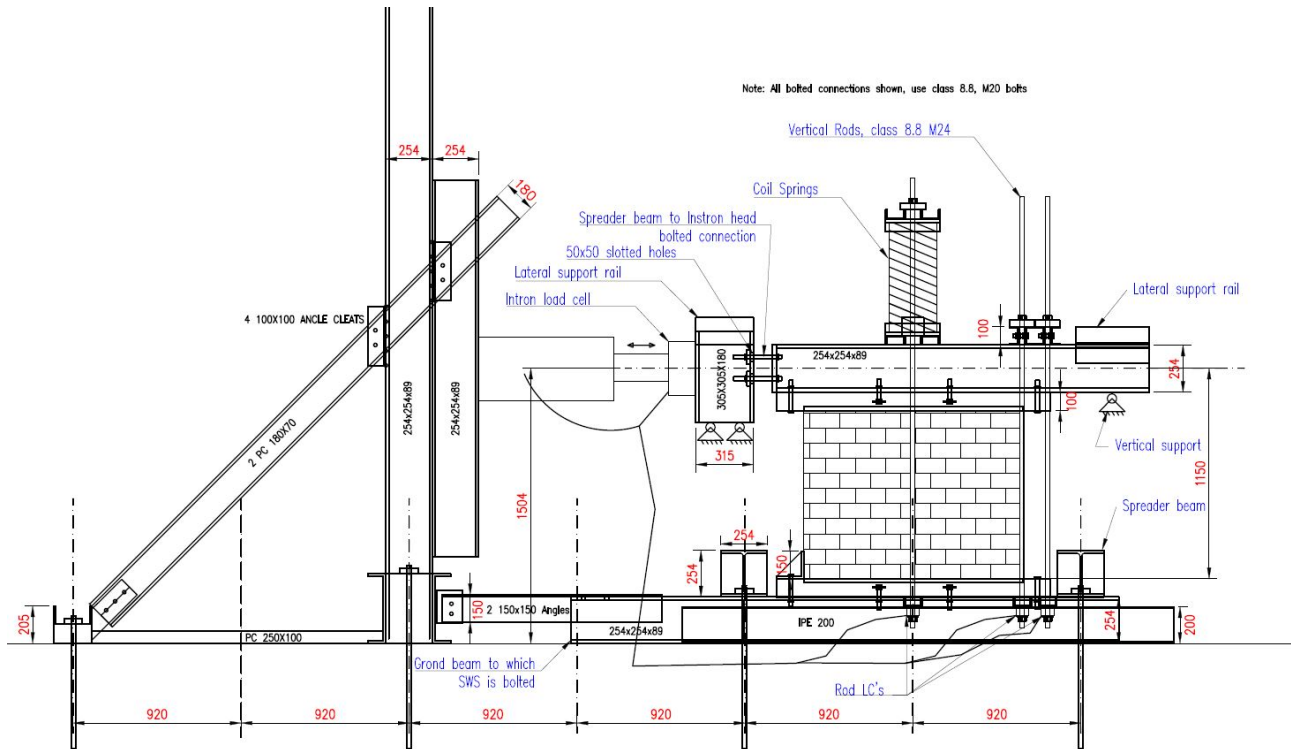


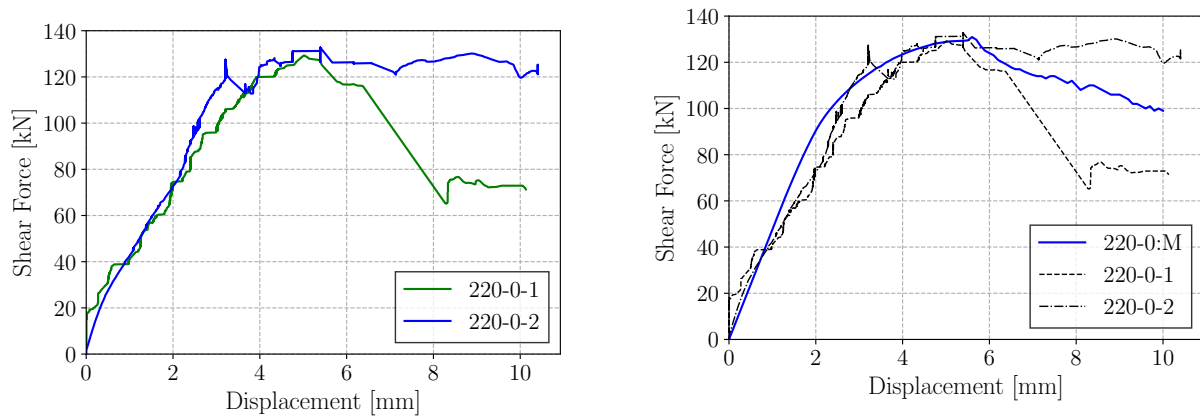
Figure 2.22: Experimental setup (De Beer, 2016)

De Beer (2016) designed the SHCC mix, as discussed in Section 2.5, to have ideal characteristics for a sprayable retrofitting application. The wet mix properties were so that the mix was sprayable, cohesive and had a high viscosity. The hardened properties of the mix was that of typical SHCC, i.e. strain hardening followed by strain softening.

Various material properties of the SHCC, the mortar and the masonry bricks were tested by De Beer (2016). The Young's modulus of SHCC was calculated to be 15.26 GPa, the tested average tensile strength was 2.19 MPa. The average shear strength was 5.06 MPa, that is roughly 1.5 times the tensile strength. It was found that the SHCC had a tensile strain capacity between 3% and 6% in comparison to 0.01% of normal concrete. The shear bond strength between SHCC and masonry is 2.30 MPa with a friction coefficient of 1.08. The cube compressive strength of the mortar was on average 20.23 MPa, and the compressive strength of the bricks was 44.5 MPa on average.

Five full scale tests were done by De Beer (2016), two double leaf masonry wall (220 mm) tests with no SHCC overlay, and three tests with 15 mm SHCC overlay. The shear force over displacement for the masonry and the retrofitted masonry tests are illustrated in Figures 2.23(a) and 2.24(a) respectively. De Jager (2018) did a FE analysis of the masonry wall, the shear force over displacement obtained from the FE analysis is illustrated in Figure 2.23(b). It can be seen that the model is a good representation of the full scale tests. De Jager (2018) also replicated the full scale test of De Beer (2016), namely 220-15-4, and did a FE analysis of the masonry wall retrofitted with SHCC. The shear force over displacement for the experimental test and FEA can be seen in Figure 2.24(b). The analysis captures

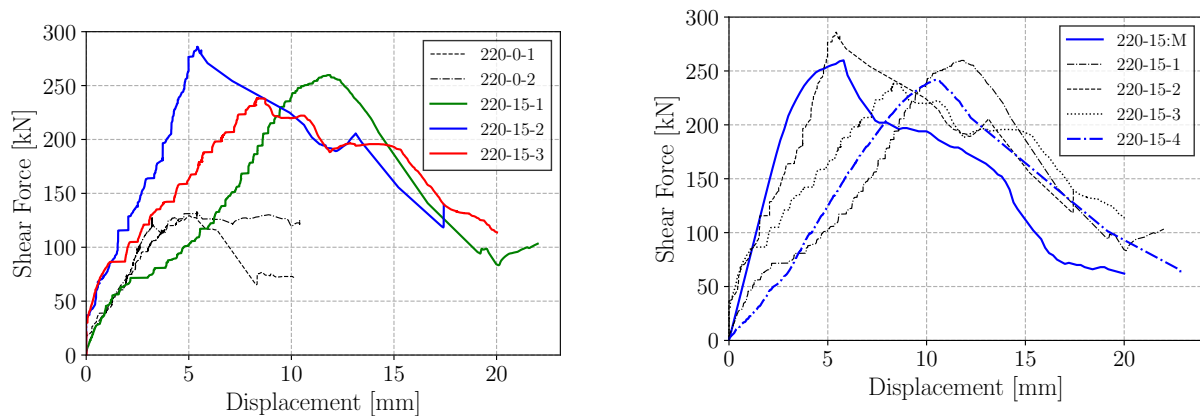
the peak forces and the post peak response, although the elastic response is more stiff than the actual tests, the model still gives a good representation of the full scale tests.



(a) Full scale test results that was done by De Beer (2016)

(b) Full scale test results in comparison to the FEM results (De Jager, 2018; De Beer, 2016)

Figure 2.23: Shear force over displacement of the full scale tests and a comparison to the FEM results for a double leaf masonry wall with no SHCC overlay.



(a) Full scale test results that was done by De Beer (2016)

(b) Full scale test results in comparison to the FEM results (De Jager, 2018; De Beer, 2016)

Figure 2.24: Shear force over displacement of the full scale tests and a comparison to the FEM results for a double leaf masonry wall with a 15 mm SHCC overlay.

With regards to the notation used in Figure 2.23 and Figure 2.24, the first number refers to the masonry wall thickness, that will be 220 mm throughout. Second is the overlay thickness, either 0 for no overlay or 15 for a 15 mm SHCC overlay. The third part refers to the number of the test, as some of the same tests were repeated, or a 'M' that refers to the results of the FE analysis done by De Jager (2018).

2.8.1 Ductility Factor

The ductility factor is used to validate or measure whether or not the retrofitting provided sufficient ductility to improve seismic resistance. The ductility of a structure refers to the ability of a structure to deform into the plastic region without failing. The ductility factor, (μ), is calculated as in Equation 2.8.1 (Mahmood and Ingham, 2011), and the parameters are illustrated in Figure 2.25. This factor

was used by De Beer (2016) and De Jager (2018) to determine the effect the SHCC overlay has on the overall ductility of the masonry. The ductility of a structure is important for seismic resistance.

$$\mu = \frac{\delta_u}{\delta_y} \quad (2.8.1)$$

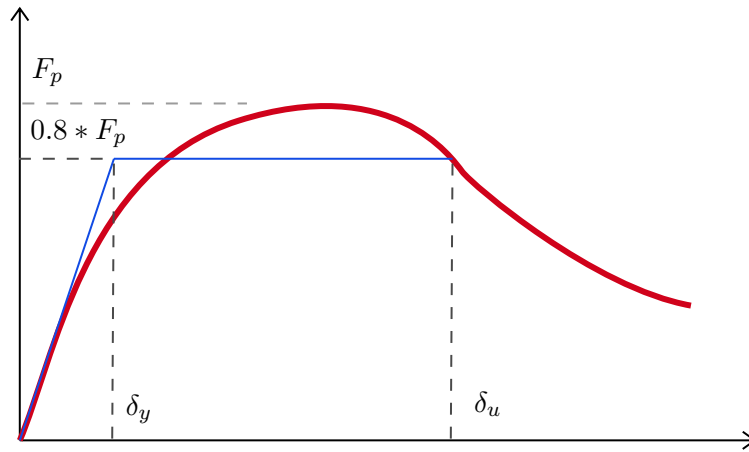


Figure 2.25: Ductility equation value illustration

De Jager (2018) found that the SHCC overlay increased the shear resistance but not the ductility of the retrofitted masonry walls. The calculated ductility factors are discussed in Section 2.8.3 and listed in Table 2.3.

There are a few shortcomings associated with the ductility factor. Although it gives an indication of the wall's ductility it is in terms of a percentage of the maximum shear force and gives no indication of the maximum shear resistance. Therefore a structure can show high ductility but have a very low shear resistance.

2.8.2 Debonding Strip Theory

De Jager (2018) found that the SHCC overlay increased the shear resistance of the masonry wallets, but the ductility did not increase. He implemented debonding strips to improve the ductility based on Luković *et al.* (2014) findings on SHCC overlays. Luković *et al.* (2014) conducted tests on small concrete beam specimens with a SHCC overlay on the tension side. The beam specimens had smooth and rough surface finishings. Luković *et al.* (2014) found that the specimens with a smooth surface developed more cracks and had higher energy dissipation in comparison to the rough surface specimens. Debonding occurred between the SHCC overlay and the substrate, this can be seen in Figure 2.26, where the SHCC overlay is at the bottom and (a) to (c) varies in surface roughness.

The debonding reduced the constraints on the overlay and enabled a higher cracking capacity for the SHCC overlay, and therefore higher energy dissipation. It is still important to have a good bond between the SHCC overlay and the substrate, as uncontrolled debonding of the overlay will cause the overlay to have no structural contribution. This concept was implemented by De Jager (2018) by adding debonding strips between the masonry substrate and SHCC overlay as illustrated in Figure 2.27.

2.8.3 Energy Contribution Factor

An energy contribution factor (ECF) was developed by De Jager (2018). The factor is used to numerically illustrate the change in energy dissipation of the SHCC overlay without debonding strips in

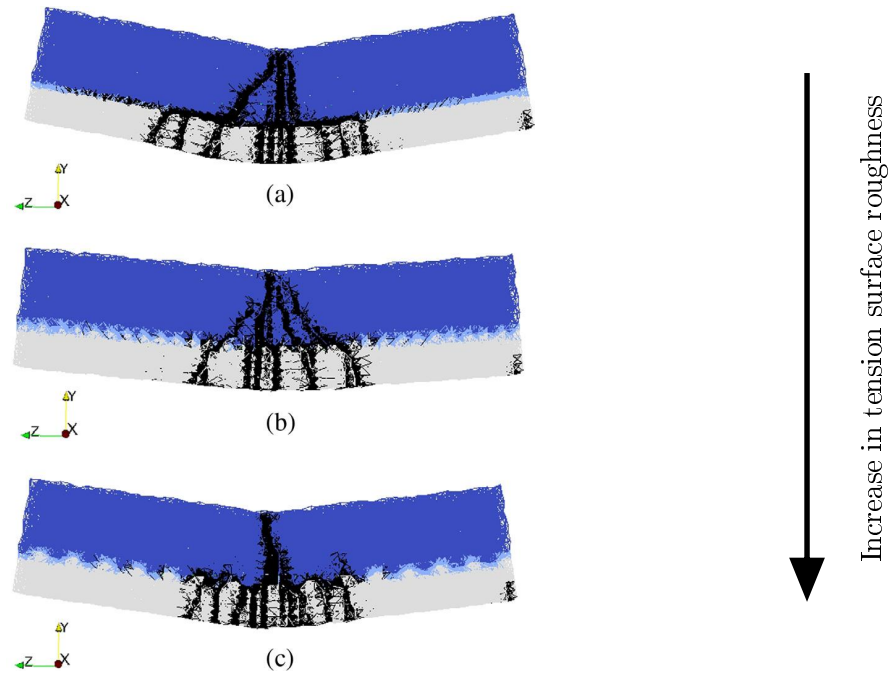


Figure 2.26: SHCC specimens fracture patterns (Luković *et al.*, 2014)



Figure 2.27: Debonding strips on the masonry wall (De Jager, 2018)

comparison to when debonding strips are added between the SHCC overlay and the masonry substrate. The ECF is calculated as in Equation 2.8.2, and the variables for the equation is illustrated in Figure 2.28.

$$ECF = \frac{\delta_{su} - \delta_{sy}}{\delta_{ru} - \delta_{ry}} \quad (2.8.2)$$

De Jager (2018) tested debonding strips with a 75 mm width at a 150 mm spacing (75-150) and strips with 100 mm width and a 200 mm spacing. A FE analysis was done on the 75-150 strips. A summary of all the shear force versus displacement results obtained is illustrated in Figure 2.29. Delamination of the debonded SHCC overlay occurred due to the concrete beam inducing compression in the SHCC overlay. This was prevented by cutting 20 mm gaps in the SHCC overlay at the top and bottom. The

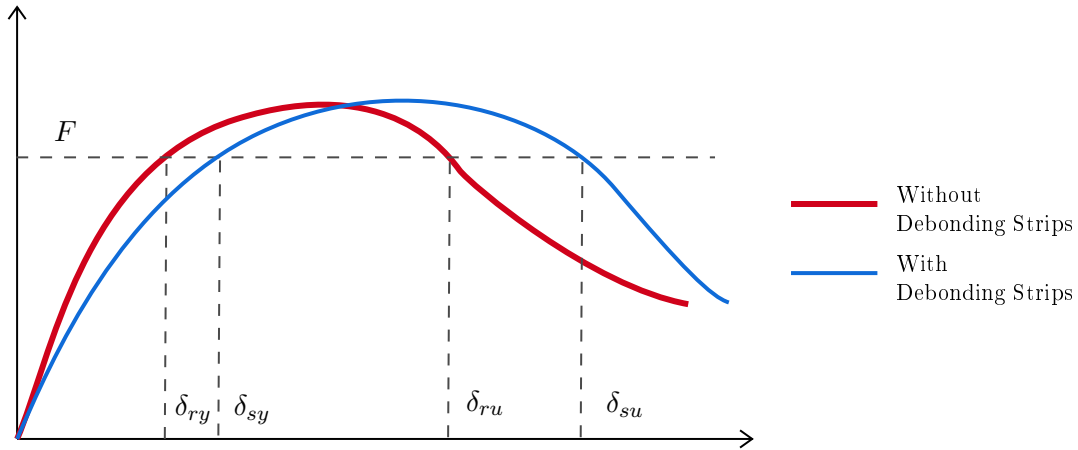


Figure 2.28: Energy Contribution Factor parameters

shear force against displacement for the two experimental tests with debonding strips that did not delaminate are illustrated in Figure 2.29.

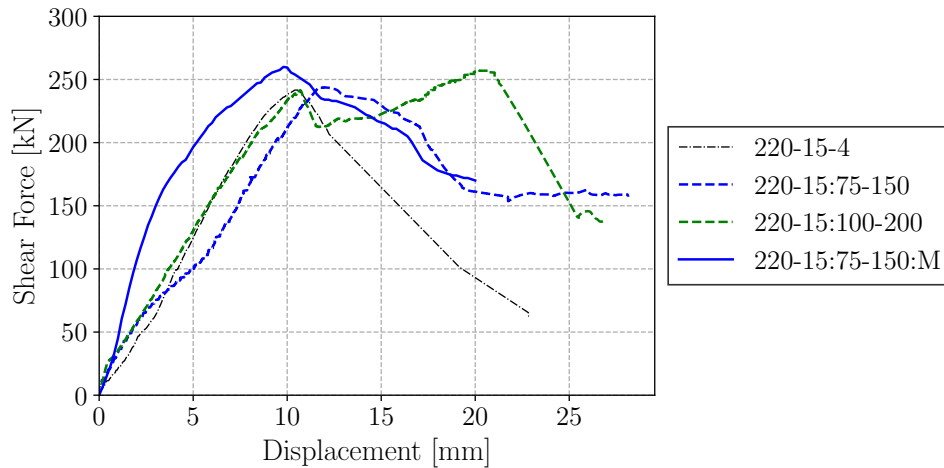


Figure 2.29: Shear force against displacement for the experimental tests and FEA with debonding strips done by De Jager (2018)

Table 2.3 lists the ductility factors for all the tests and it can be seen that there is a general increase in ductility with the addition of the debonding strips. The debonding strips also increased the energy dissipation of the retrofitted walls as listed in Table 2.4. It was therefore concluded by De Jager (2018) that the debonding strips increased the ductility of the masonry walls, provided that delamination of the overlay is prevented.

Table 2.3: Ductility Factors (De Jager, 2018)

Specimen	δ_y (mm)	δ_u (mm)	μ	F_p (kN)
Numerical				
220-0	2.6	9.1	3.5	131.3
220-15	2.9	7.3	2.6	259.9
220-15:75-150	4.4	16.8	3.6	260.0
Experimental				
220-0	3.1	6.8	2.2	129.2
220-15	8.8	13.2	1.5	241.7
220-15:75-150:1	6.8	16.8	2.5	218.9
220-15:75-150:2	8.8	17.6	2.0	243.8
220-15:100-200	8.8	23.5	2.7	257.0

Table 2.4: ECF values at different forces (De Jager, 2018)

F_i	75-150 (avg.)		100-200
	Numerical	Experimental	Experimental
175	1.54	1.31	2.28
200	2.35	1.32	3.10
225	2.31	1.94	3.36

Chapter 3

Finite Element Model Development

In this chapter the development of in-plane, quasi-static finite element models of the experimental test configurations is discussed. Detail is given regarding the geometry, material models, boundary conditions, loading, meshing and analysis procedures.

3.1 Finite Element Model Setup

Previous tests done by De Beer (2016) and De Jager (2018), as well as the Finite Element (FE) models of De Jager (2018) were discussed in Section 2.8. The results of these tests and analyses form the basis of this study. The FE analyses were replicated and developed further using Diana 10.2. A schematization of the FE model is illustrated in Figure 3.1 illustrating the boundary conditions and the applied loading.

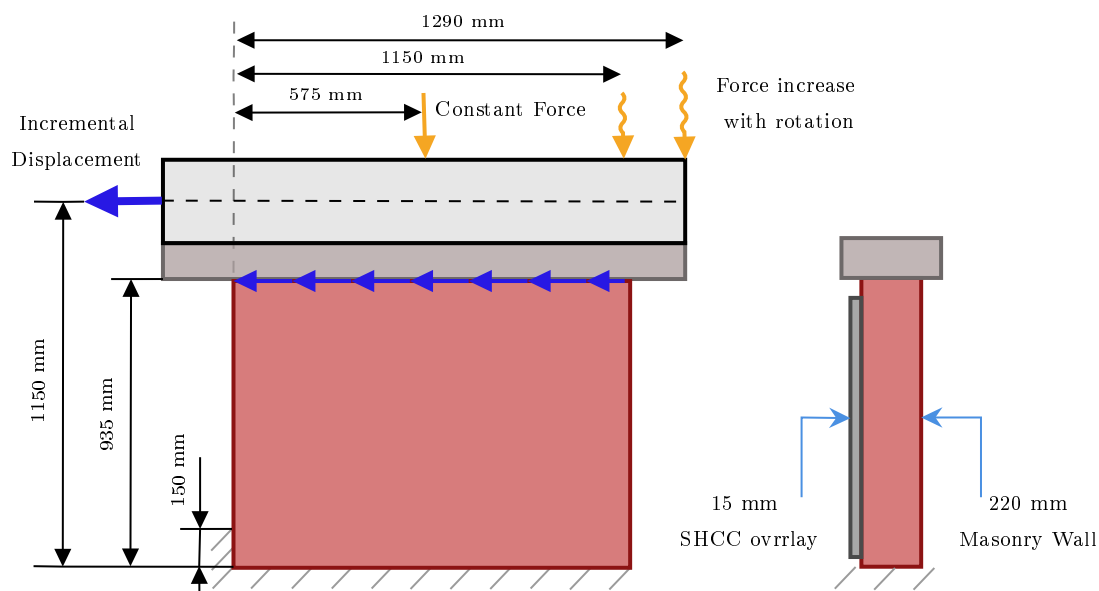


Figure 3.1: Basic setup of full scale shear wall test

3.1.1 Geometry

The geometry of the model consists of the masonry, SHCC, steel beam, concrete beam, and the steel rod pairs. All of the elements were modelled as 3D membranes, except the rods that were modelled as 3D lines. The masonry and SHCC have a thickness of 220 mm and 15 mm respectively and face

dimensions of 1150 x 935 mm for both. The concrete beam has dimensions of 1500 x 100 x 400 mm. The steel beam is a H254 x 254 x 89 beam at 1500 mm length. The steel beam was divided into three sections, namely the top and bottom flange and the web. This was done to have the correct cross-sectional area and moment of inertia for the beam. The rods have a cross-sectional area of 5 mm^2 , and a length of 1295.4 mm.

3.1.2 Boundary Conditions

The boundary conditions applied to the model were based on the full scale tests done by De Beer (2016) and De Jager (2018). The bottom of the masonry and rods were restrained in the horizontal and vertical directions. The out of plane displacement for the whole model was restrained as only in-plane behaviour was considered. The point where the displacement is applied is also constrained in the direction of the displacement, this is done due to the way Diana calculates imposed displacements. To accurately simulate the application of the imposed load, a link was defined on the edge of the steel beam where the displacement is applied and defined that the edge follows the imposed displacement in the horizontal direction.

3.1.3 Loading

The entire model is subjected to gravitational loading, which was applied as a global load, with the gravitational acceleration taken as 9.81 m/s^2 . The rods were pre-tensioned before the incremental displacement was applied, with initial loading as in Table 3.1. These forces were implemented in the model by applying point loads at the top of the steel beam. In the experimental tests done by De Beer (2016), the forces in Rod 1 stayed constant due to the coil, and the forces in Rods 2 and 3 increased as the displacement increased, this is illustrated in Figure 3.2. The rod pairs are grouped together in the figure and the total force for each rod pair is illustrated. This had to be taken into account in the model.

Table 3.1: Initial and end forces for the Rods

	Initial Force	Final Force
Rod 1	30 kN	30 kN
Rod 2	13 kN	74 kN
Rod 3	15 kN	122 kN

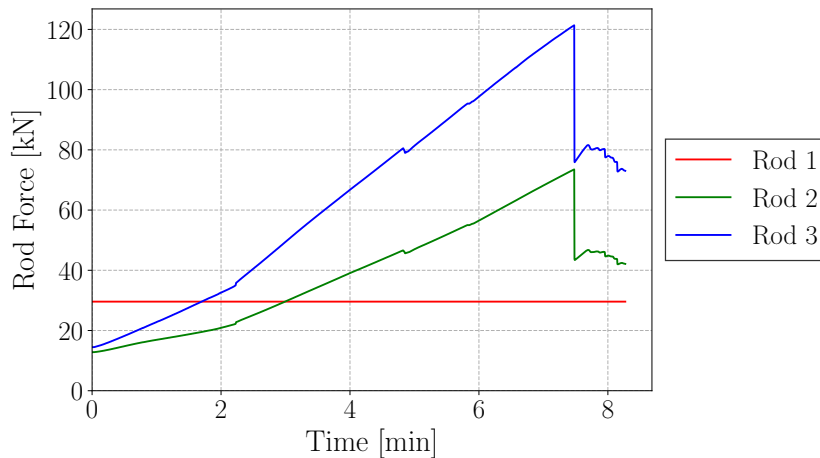


Figure 3.2: Rod forces

A total displacement of 17.62 mm was applied in a total of 100 increments, which differs from the total displacement of 20 mm applied by De Beer (2016) and De Jager (2018) in the experimental and numerical tests. This is due to the way the increase in rod forces are modelled. The forces in Rod pairs 2 and 3 can only be modelled accurately up to 17.62 mm displacement, as only the linear force increase can be taken into account and the sudden decrease in the rod forces can not be modelled. This is due to the model being set up as displacement increments and not as time increments. The initial and final rod forces are listed in Table 3.1. The rod forces are increased incrementally along with the displacement, see Section 3.1.6 for full discussion on the analysis.

3.1.4 Materials

The material values provided in this section were obtained from the experimental tests done by De Beer (2016). The parameters that were omitted from testing are indicated in grey in Tables 3.2 to 3.5. These parameters were obtained by changing the unknown parameters within realistic bounds until the correct failure mechanisms and shear force against displacement curves were obtained. The unknown parameters for the masonry and SHCC describes the material failure properties. It was found that some parameters were dependent on one another, this was also the case in research done by De Villiers (2019).

3.1.4.1 Masonry

A Rankine-Hill smeared crack model, as discussed in Section 2.6.2.1, was used for the masonry material model. This material model can take into account the elastic and plastic orthotropic characteristic of masonry. The material values implemented in Diana are listed in Table 3.2. The crack bandwidth specification was that of Rots (1988) and the crack rate dependency model was that of Wu and Bažant (1993), with $k_0 = 0.05$, $k_1 = 0.05$, and $dk_r/dt = 3$.

Table 3.2: Rankine-Hill model parameters for masonry

Symbol	Value	Description
E	1500 N/mm ²	Young's modulus
ν	0.2	Poisson's ratio
ρ	2100 kg/m ³	Mass density
ft_x	0.1 N/mm ²	Tensile strength (x)
ft_y	0.1 N/mm ²	Tensile strength (y)
fc_{ux}	18 N/mm ²	Compression strength (x)
fc_{uy}	18 N/mm ²	Compression strength (y)
Gt_x	0.05 N/mm	Fracture energy in tension (x)
Gt_y	0.15 N/mm	Fracture energy in tension (y)
Gc_x	0.35 N/mm	Fracture energy in compression (x)
Gc_y	0.35 N/mm	Fracture energy in compression (y)
ϵ_u	0.0006	Ultimate compressive strain
μ_{tol}	0.01	Relative residual tensile strength
m	8	Super-hyperbolic Rankine-Hill parameter
n	8	Super-hyperbolic Rankine parameter

3.1.4.2 SHCC

A Rankine-Rankine Total strain based crack model was used for the SHCC. This model was chosen to simulate the experimental results within reasonable bounds. A high fracture energy was used to capture the elastic perfectly-plastic behaviour of SHCC, this approach adequately represents the strain-hardening of the SHCC. A smeared rotational crack model was specified. The tension behaviour was

modelled with the exponential tensile curve, as discussed in Section 2.6.2.2. The material values that were used are listed in Table 3.3. The crack bandwidth was prescribed to match the finite element representative size, according to Rots (1988). The linear hardening compression curve was selected to simulate compression, and the JSCE 2012 Figure 2.2.5 (JSCE, 2010) reduction model was implemented for the reduction model due to lateral cracking.

Table 3.3: Rotating smeared crack material model parameters for SHCC

Symbol	Value	Description
E	15260 N/mm^2	Young's modulus
ν	0.2	Poisson's ratio
ρ	2100 kg/m^3	Mass density
f_t	7 † N/mm^2	Tensile strength
G_{ft}	10 N/mm	Fracture energy
f_{tR}	3 † N/mm^2	Residual tensile strength
f_c	20 N/mm^2	Compressive strength
H	0.2 N/mm^2	Hardening modulus

† This is higher than than the values published by De Beer (2016) in order to match the experimental results

3.1.4.3 Interface

The interface between the masonry and SHCC was modelled with a Coulomb friction material model. The material properties that were specified are listed in Table 3.4.

Table 3.4: Coulomb friction interface material parameters

Symbol	Value	Description
k_n	1e+09 N/mm^3	Normal stiffness modulus
k_{t_x}	1e+08 N/mm^3	Shear stiffness modulus (x)
k_{t_y}	1e+08 N/mm^3	Shear stiffness modulus (y)
c	2.3 N/mm^2	Cohesion
ϕ	1.07 rad	Friction angle
ψ	1.07 rad	Dilatancy angle

3.1.4.4 Concrete and Steel

The concrete and steel beams were modelled as linear elastic materials to limit the complexity of these elements as they are not the focus of the numerical tests. The material parameters are summarized in Table 3.5.

Table 3.5: Concrete and Steel linear elastic material parameters

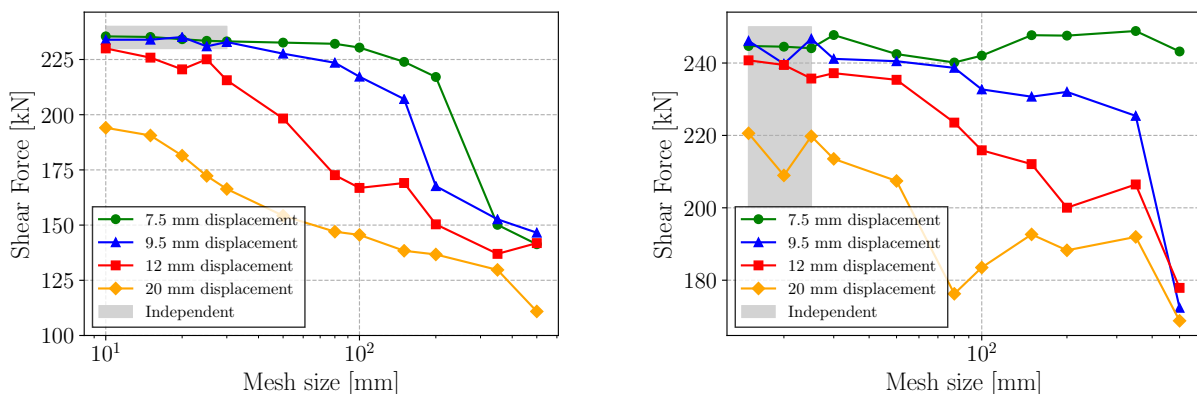
Symbol	Concrete	Steel	Description
E	28 GPa	200 GPa	Young's modulus
ν	0.15	0.3	Poisson's ratio
ρ	2350 kg/m^3	7850 kg/m^3	Mass density

3.1.5 Mesh

The appropriate mesh size and element type for the FE model was determined by conducting a mesh dependency analysis. The relevant mesh elements available in Diana is discussed in Section 2.6.3. Only the quadratic elements were considered, as well as different numerical integration schemes, namely normal or high. The shear force was measured at different displacements and plotted against the element size. This was done to determine at what element size the model starts yielding stable shear resistance.

The quadrilateral element with normal (2x2) integration showed no significant trend, and its results are not reliable. Figure 3.3(a) illustrates the shear force against mesh size for the high (3x3) integration scheme, this gives an indication of the mesh dependency of the model. The results started to yield mesh independent behaviour for displacements up to 9.5 mm with a maximum mesh size of 30 mm as illustrated in Figure 3.3(a). The results are still mesh dependent and unreliable for higher displacements, as indicated by the upward trend for the 12 mm and 20 mm displacements.

The quadratic triangular element's mesh dependency was only tested with high integration. There is no difference in the integration levels in Diana (DIANA FEA BV, 2017b), as three integration points are used throughout. Figure 3.3(b) shows that reliable results can be obtained for all the displacements with an element size of 25 mm or smaller. The final mesh layout for the 220 wall model is illustrated in Figure 3.4, using an element size of 25 mm.



(a) Quadrilateral elements, ranging in size from 10 mm to 500 mm

(b) Triangular elements, ranging in size from 15 mm to 500 mm

Figure 3.3: Mesh dependency of quadrilateral and triangular elements with high integration

3.1.6 Analyses

A non-linear phased analysis approach, comprising two phases was used. Phase one first applied the gravity loading followed by the initial rod forces. Both of these were solved using Regular Newton-Raphson equilibrium iteration, with an energy convergence norm. Phase two first applied the results from Phase one, followed by a load step analysis, in 0.01 steps increments, of the incremental displacements and rod force increase. Phase two is solved using Secant-BFGS equilibrium iteration with an energy convergence norm. Both phases use a Parallel Direct Sparse solution method. The loads are listed in their respective Phases in the applied order in Table 3.6.

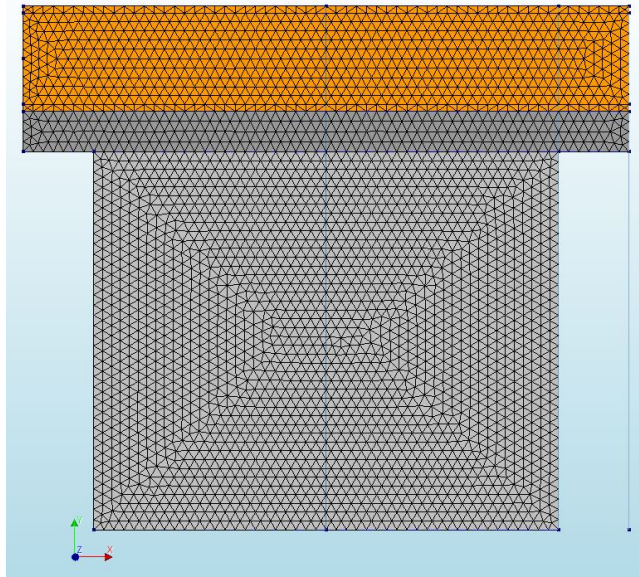


Figure 3.4: 25mm Triangular mesh of the shear wall model

Table 3.6: Loads applied in the respective Phases

	Own Weight	Initial Rod	Displacement	Increased Rod
Phase 1	1	1		
Phase 2			1	1

3.2 FEM of Debonding Strips

De Jager (2018) found that the SHCC significantly increases the shear resistance of the masonry walls, but does not increase the ductility of the masonry walls, which is critical for seismic resistance. Debonding strips were added to improve the ductility, as discussed in Section 2.8. Figure 3.5 illustrates how the finite element model was set up in Diana. It is similar to the model in Section 3.1, except for the debonding strips that were added by defining a weak interface between the masonry substrate and the SHCC overlay along each strip. The debonding strip width is denoted as w and the centre to centre spacing as s .

3.2.1 Geometry

The geometry is the same as discussed in Section 3.1.1, except for the added debonding strips. Two experimental tests were done by De Jager (2018), one test had a strip with of 75 mm at a 150 mm spacing (75-150), and the second had a strip with of 100 mm at a 200 mm spacing (100-200). Only the 75 mm strips are discussed as the 100 mm strips have similar results.

3.2.2 Debonding Strip Interface

A Coulomb friction material model was also used for the debonding strip interface and the material properties for the interface between the SHCC and masonry at the debonded area are as listed in Table 3.7. The material properties are defined in such a way to ensure a weak bond between the SHCC overlay and the masonry substrate.

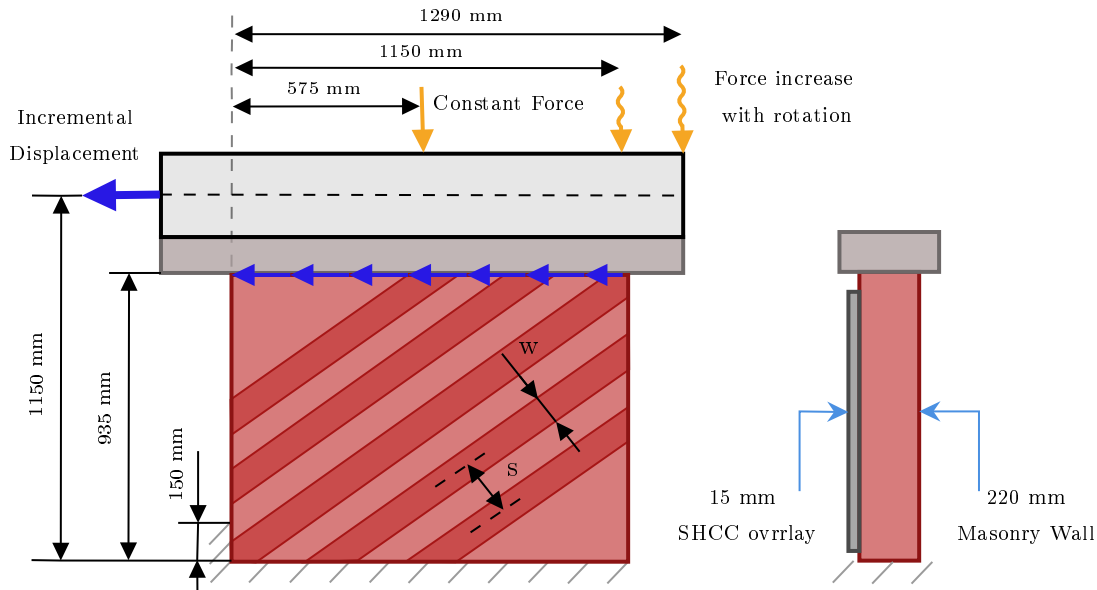


Figure 3.5: Basic setup of the full scale shear wall test with debonding strips

Table 3.7: Coulomb friction interface material parameters for debonding strips

Symbol	Value	Description
k_n	$1e-06 N/mm^3$	Normal stiffness modulus
k_{t_x}	$1e-05 N/mm^3$	Shear stiffness modulus (x)
k_{t_y}	$1e-05 N/mm^3$	Shear stiffness modulus (y)
c	$2.3 N/mm^2$	Cohesion
ϕ	$1.07 rad$	Friction angle
ψ	$1.07 rad$	Dilatancy angle

3.3 Output Results

In order to determine whether the numerical model gives a good representation of the experimental tests, certain values and failure mechanisms have to be measured and compared. Firstly the failure mechanisms were checked for diagonal shear by considering the principal strain (E1) distribution over the masonry substrate and the SHCC overlay. It is important to note that the experimental tests showed an early tension crack at the bottom right hand corner. The shear force as a function of displacement is known for the experimental tests and the numerical models have to reflect similar distribution and characteristics.

3.4 FE Model Summary

The FE model with the masonry alone was modelled to simulate the results that were obtained in the experimental tests done by De Beer (2016). As not all of the masonry material properties that are required in the Rankine-Hill material model were known from experimental tests, these had to be obtained numerically. Similarly the Rankin-Rankine material parameters for the SHCC were determined by modelling the masonry, with the now known material parameters, retrofitted with SHCC and using the experimental results of De Beer (2016) and De Jager (2018). Lastly the debonding strips were also modelled with all the material parameters now known.

Chapter 4

Finite Element Model Results

This section discusses the numerical results obtained from the models described in the previous chapter. The results are compared to experimental and previously obtained numerical data.

4.1 Masonry Wall

This section discusses the results obtained for the numerical test with the 220 mm masonry substrate with no retrofitting and compared to the two experimental tests done by De Beer (2016).

Figure 4.1 illustrates the shear force against displacement (220-0:N) obtained by the numerical model for the masonry substrate with no retrofitting. The numerical results are shown in comparison to the results obtained from the experimental tests done by De Beer (2016) and the numerical model of De Jager (2018) (220-0-M). It can be seen that the numerical model is initially overly stiff but shows a good correlation to the experimental results by capturing the failure mechanism of test 220-0-1, as well as the maximum shear force of both experimental tests.

The shear force against displacement graph does show post peak jumps in the shear force. This is mainly due to stiffness reduction when shear slipping occurs, followed by a stiffness increase due to a friction increase induced by the compressive forces in the rods. There were also no sporadic modes in the FE model, confirming that the model is not numerically unstable.

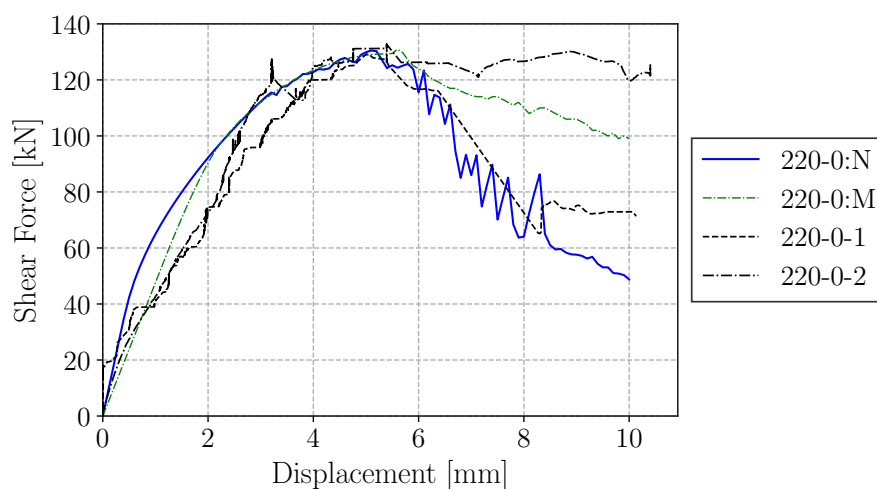


Figure 4.1: Shear force against displacement for the Masonry wall with no retrofitting

The principal strain (E1) distribution at different displacements is illustrated in Figure 4.2. This shows that the model captures the typical diagonal shear failure of the experimental tests. At 1 mm displacement the flexural shear failure is more prominent at the bottom right-hand corner, this was the case for the experimental test as well. At 2 mm displacement diagonal shear failure becomes more prominent and the masonry has started to fail but still has not reached the ultimate shear resistance that occurs at about 5 mm displacement with a shear resistance of 130 kN. At 10 mm displacement the masonry wall has failed completely in diagonal shear and experiences toe crushing.

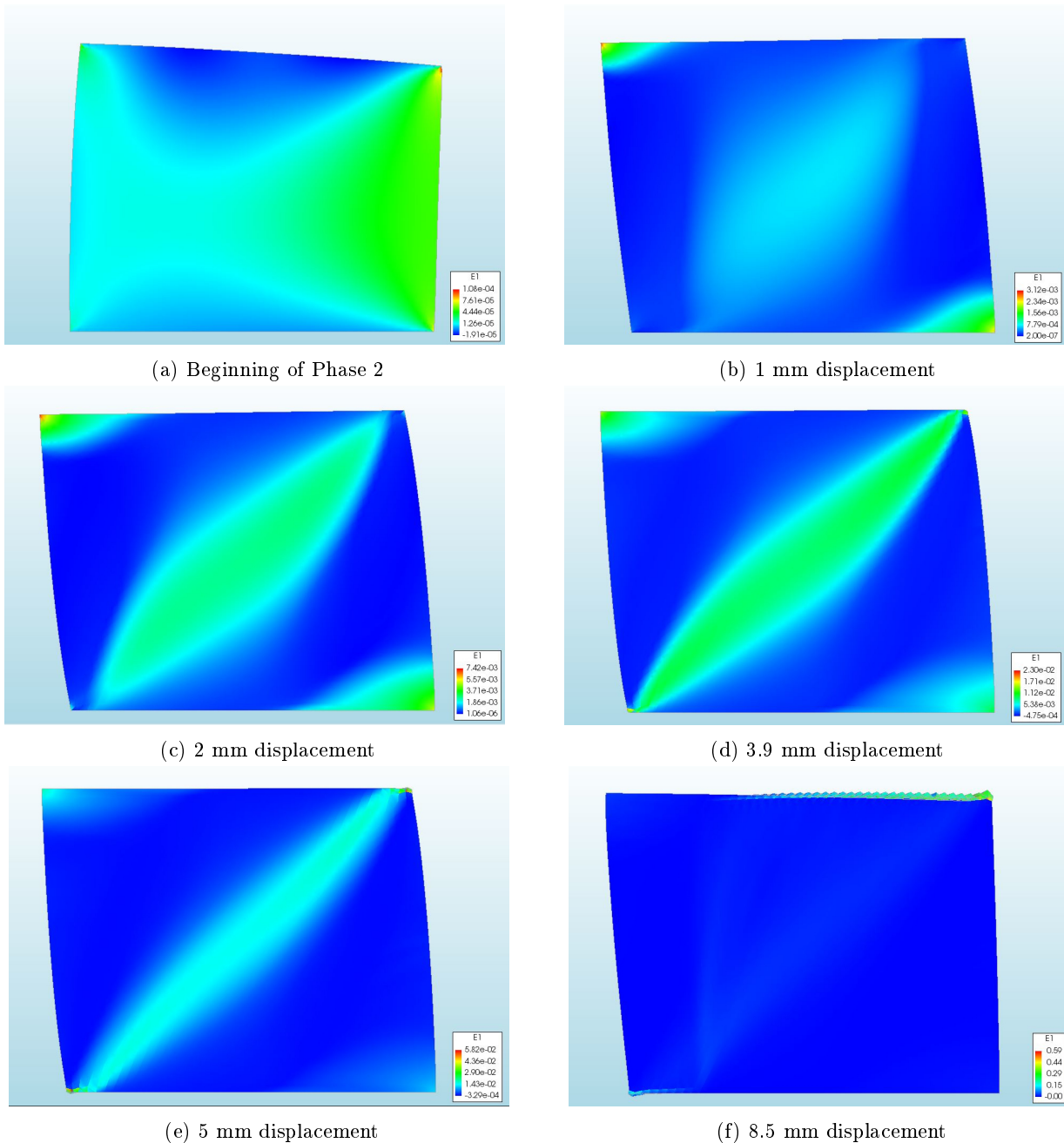


Figure 4.2: Principal strains (E1) for the masonry wall with no retrofitting at the respective displacements.

The ductility of the masonry wall with no retrofitting for the experimental tests were calculated to be 1.82 on average with a coefficient of variation of 0.187. The numerical test gave a ductility of 3.28, which is significantly higher than the experimental tests. This high ductility of the computed response

is not apparent by visual inspection of Figure 4.1. The numerical model represents the 220-0-1 test the closest, with a ductility of 2.16. The difference in ductility is mainly due to the numerical model being initially overly stiff. The numerical model of the masonry gives a good representation of the experimental results and captures the key behaviour of masonry walls.

4.2 SHCC retrofitting

This section discusses the masonry model developed in the previous section, retrofitted with SHCC. It is compared to four experimental results. The material parameters for SHCC were based on the values tested by De Beer (2016) and the omitted parameters were obtained through numerical fitting.

The shear force against displacement for the numerical model of the 220 mm masonry substrate retrofitted with a 15 mm SHCC overlay is illustrated in Figure 4.3, in comparison to the results of the experimental tests (De Beer, 2016; De Jager, 2018) and the numerical model (De Jager, 2018). It can be seen that the numerical model is overly stiff in comparison to the experimental data. This is to be expected as numerical models are generally more stiff than the actual model and the masonry model, as discussed in the previous section, exhibited similar behaviour. The numerical model gives a good representation of the experimental data by capturing the average maximum shear resistance of 261 kN and a similar failure mechanism.

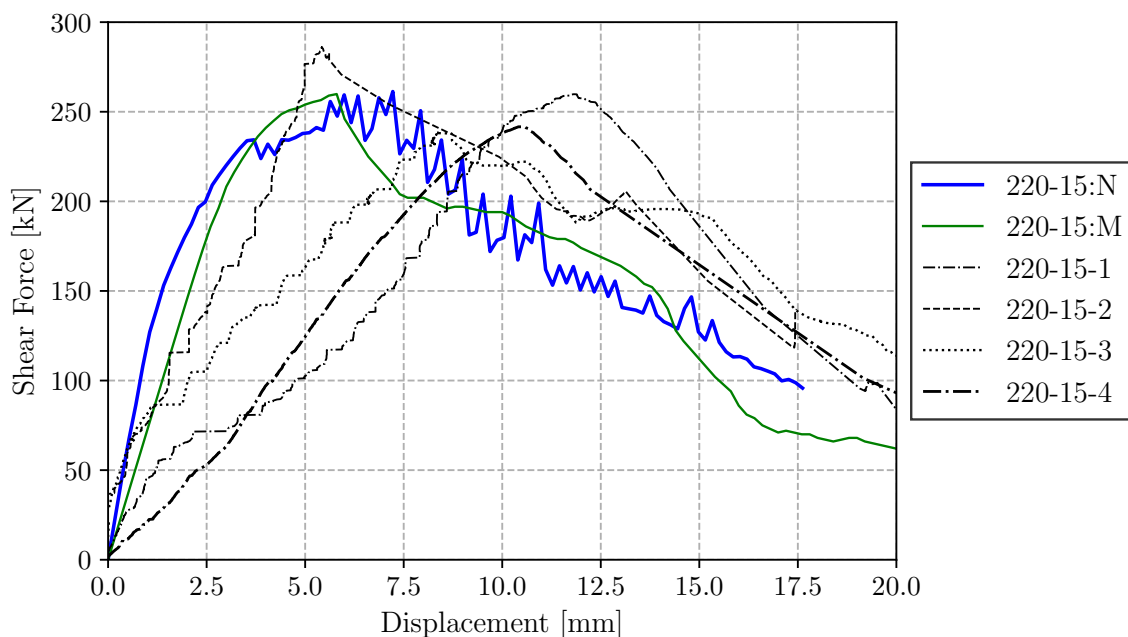


Figure 4.3: Shear force against displacement for the masonry wall retrofitted with an SHCC overlay

The distribution of the principal strains (E1) in the SHCC overlay is illustrated in Figure 4.4 at the different displacements as indicated and shows that the numerical model captures the failure mechanism of the experimental tests. The different displacements illustrated represent points of interest regarding the strain distribution and the shear-force against displacements graph. Figure 4.4(a) shows the strain distribution before the displacement is applied, Figure 4.4(b) illustrates the principal strain distribution at a 2.47 mm displacement before the ultimate shear resistance is reached and no cracking has occurred in the SHCC overlay. The initial flexural shear failure can also be observed. With a first cracking strain of 3%, the SHCC overlay starts to crack at about 5 mm displacement and shows the typical diagonal shear cracking in Figure 4.4(c) to 4.4(e). Toe crushing starts to occur after 11 mm displacement and is illustrated in Figure 4.4(f).

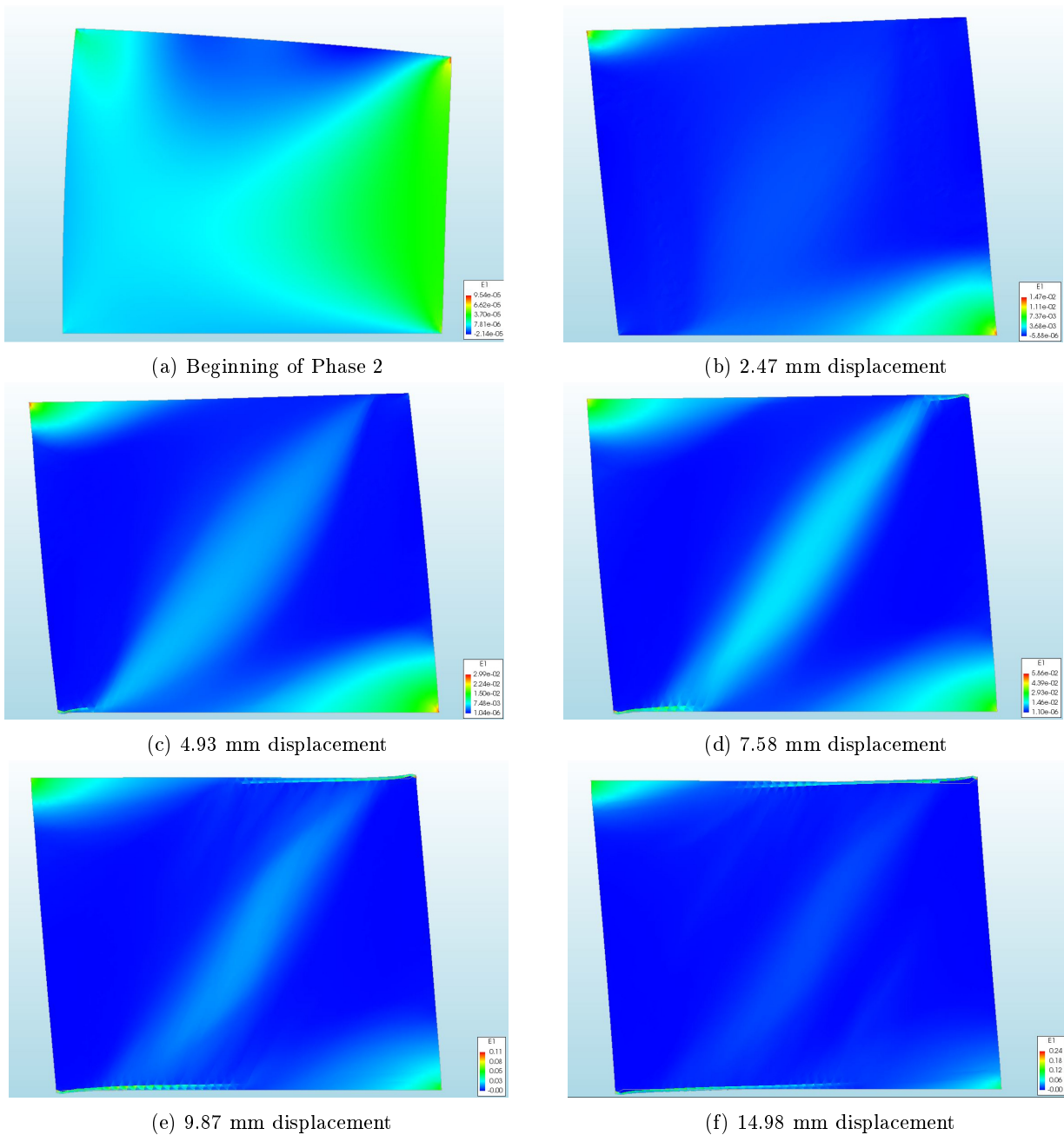


Figure 4.4: Principal strains (E1) in the SHCC overlay at different displacements.

Figure 4.5 illustrates the tractions in the interface between the masonry substrate and the SHCC overlay. The same displacements are used for the tractions as for the strain illustrations to show the comparison between the two. The tractions give a good illustration of the force distribution between the masonry substrate and the SHCC overlay and where there are force concentrations. It can be seen that initially there are uniform tractions throughout the interface before the displacement is applied, except for the top and bottom edges. As the displacement increases, the tractions start to spread out and form concentrations on the diagonal and at the edges, similarly to where there are higher strains. In the end there are large tractions on the top and bottom edges due to the compression induced by the rods and this correlates well with the strain distributions.

The ductility factor of for the masonry substrate retrofitted with a 15 mm SHCC overlay for the four experimental tests is on average 1.98 with a coefficient of variation (CoV) of 0.15. The ductility factor for the numerical test is 4.72, meaning that the ultimate displacement is 4.72 times the linearised

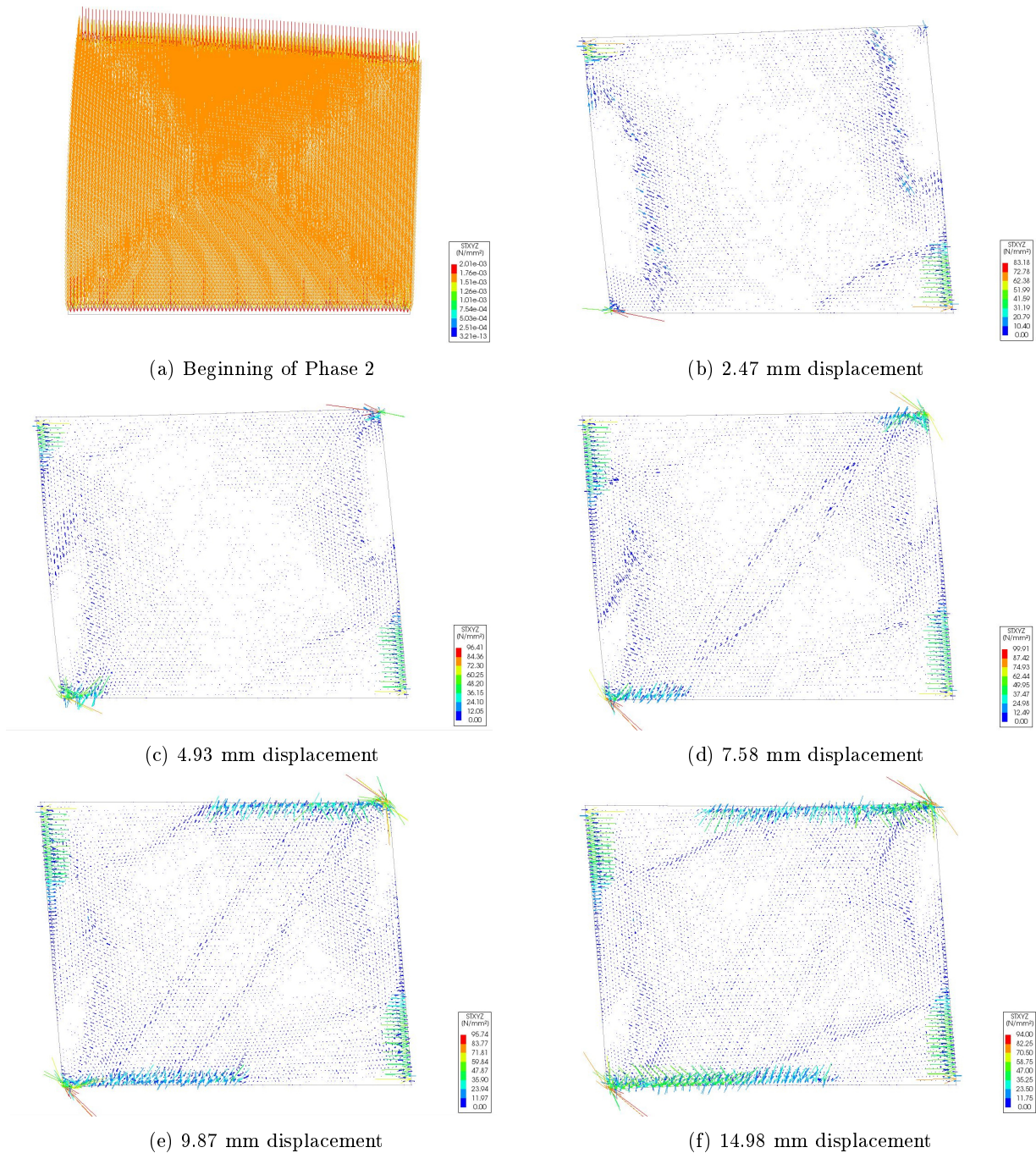


Figure 4.5: Traction in the interface between the masonry substrate and the SHCC overlay at the respective displacements.

yield displacement. This is significantly higher than the experimental results, similar to the masonry numerical model, as discussed in Section 4.1.

4.3 Debonding strips

Adding debonding strips between the SHCC and masonry showed promising results to increase the ductility of the masonry wall from the experimental and numerical tests done by De Jager (2018). The numerical model done by De Jager (2018) was recreated using the material values obtained from the tests done in Sections 4.1 and 4.2, using 75 mm strips at a 150 mm spacing.

The shear-force against displacement obtained from the numerical model is illustrated in Figure 4.6. It is shown in comparison to the numerical results obtained in Section 4.2, the numerical and experimental results obtained by De Jager (2018) and the experimental results for the test with no debonding strips (220-15-4). The numerical model with debonding strips showed a smaller difference in comparison to the model without debonding strips than that of De Jager (2018). This is mainly due to a difference in the material parameters used.

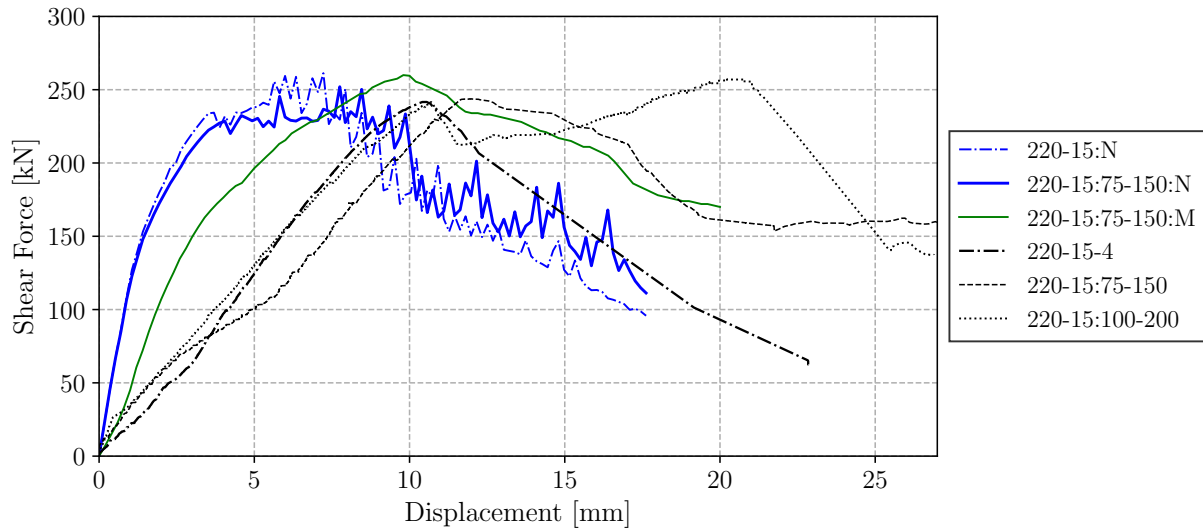


Figure 4.6: Shear force against displacement for the Masonry wall with SHCC overlay and debonding strips

Figure 4.7 illustrates the shear-force against displacement of the numerical model for the retrofitted masonry wall with and without 75-150 debonding strips. It can be seen that the numerical model indicates a slight increase in ductility, from 1.98 to 2.04, and a higher shear resistance at the end tail of the graph.

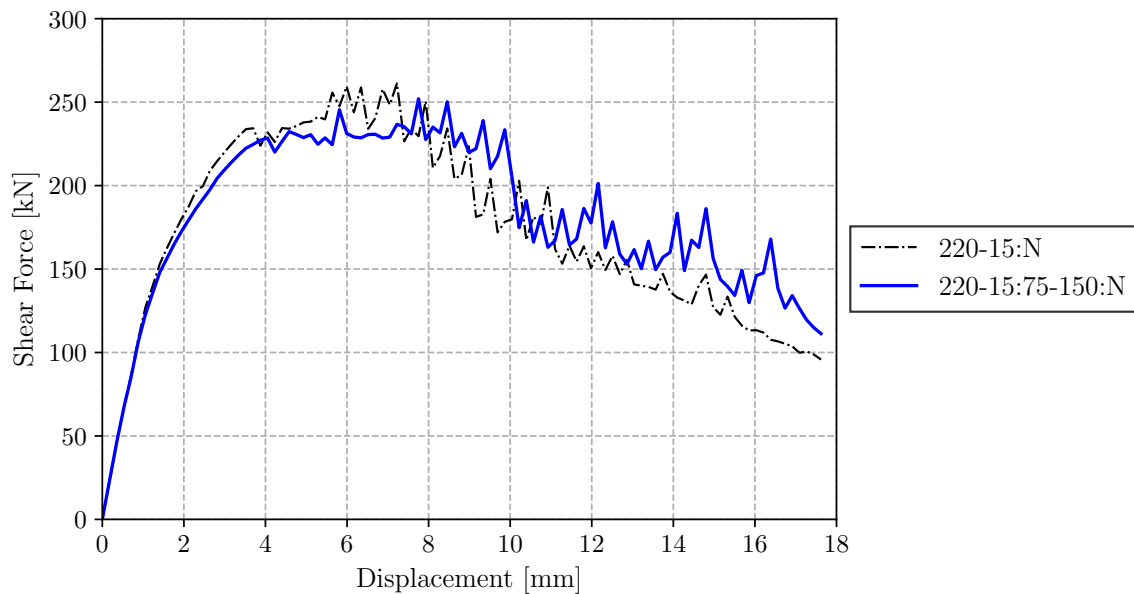


Figure 4.7: Shear force against displacement for the Masonry wall with SHCC overlay and 75-150 debonding strips obtained from the numerical models

The principal strains (E1) in the SHCC overlay are illustrated in Figure 4.8 and shows a similar distribution as without debonding strips. The major difference is that there are strain concentrations on the strip edges due to higher stresses on the edges caused by the debonding strips. The diagonal shear failure mechanism is also captured in the model, along with the failure mechanisms discussed in Section 4.2.

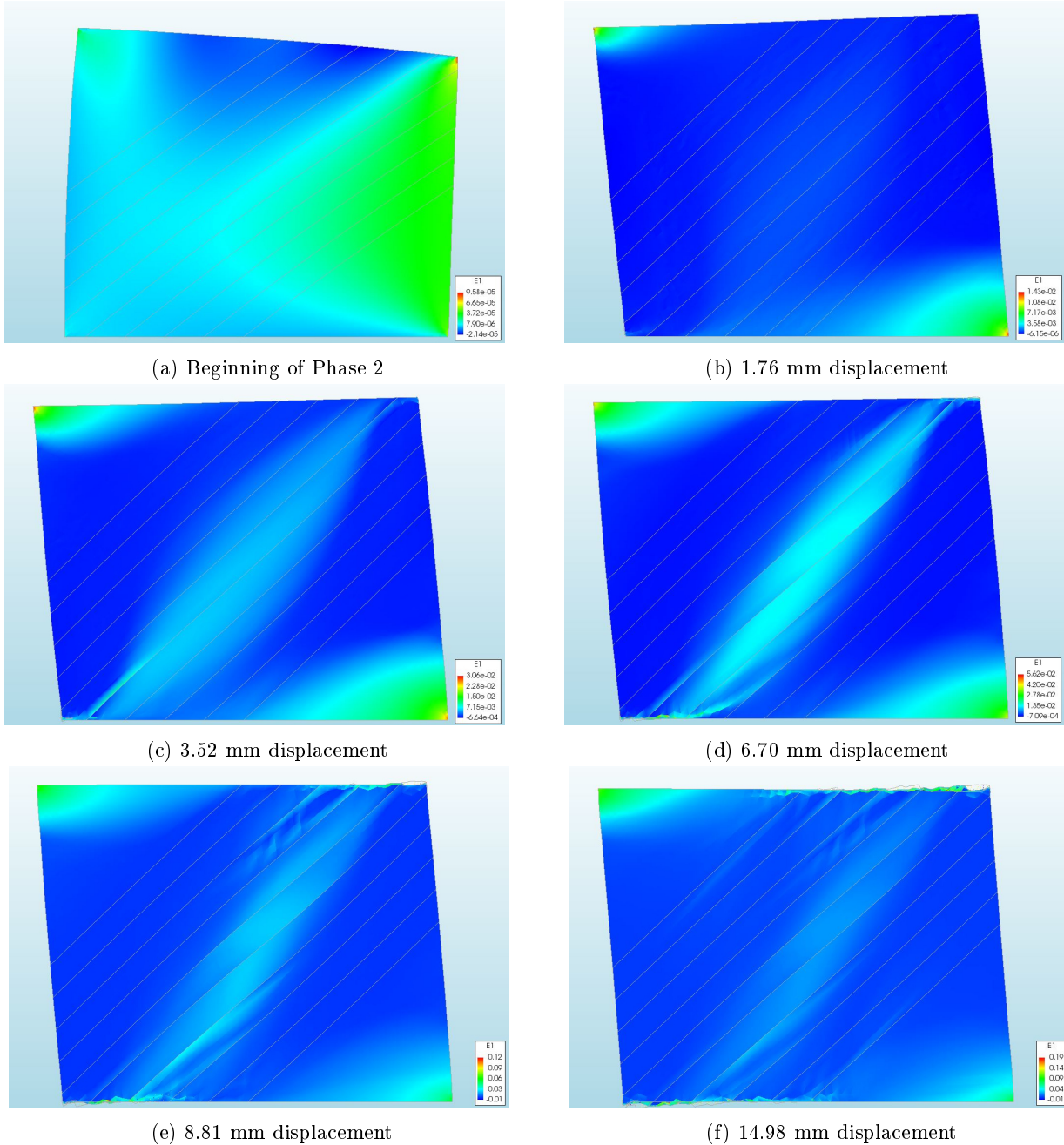


Figure 4.8: Principal strains (E1) in the SHCC overlay at different displacements for the masonry wall retrofitted with SHCC and debonding strips.

Figure 4.9 illustrates the tractions between the masonry substrate and the SHCC overlay. The effects of the debonding strips can be seen clearly, as there are no tractions between the masonry and SHCC on the debonding strips, but a higher concentration of tractions at the strip edges. This is especially prominent in Figure 4.9(a). The concentration of tractions on the strip edges correlates with the strain concentrations.

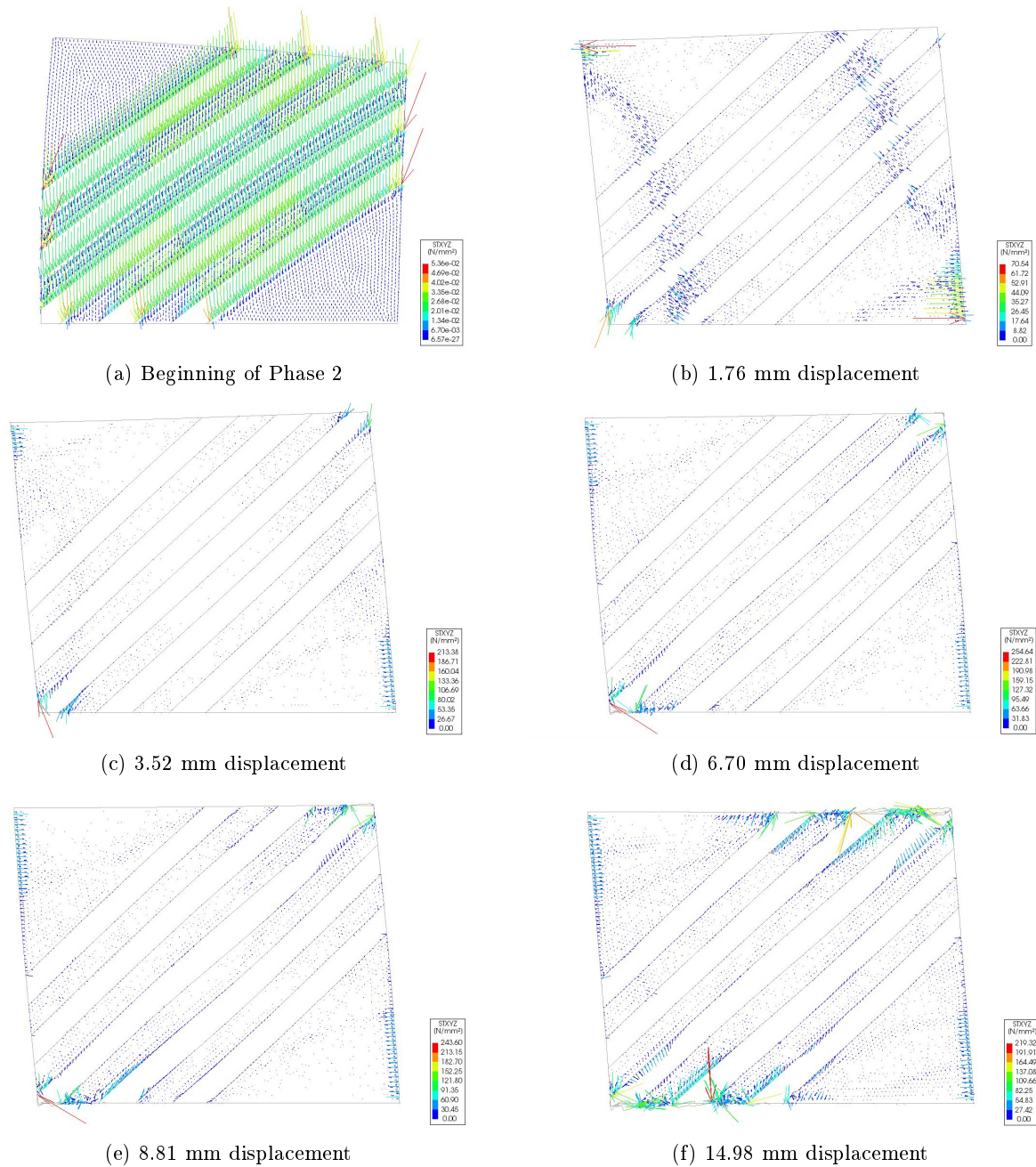


Figure 4.9: Traction in the interface between the masonry substrate and the SHCC overlay at different displacements for the retrofitted masonry wall with 75-150 debonding strips.

The ductility for the experimental test with 75-150 debonding strips is 2.04, which is not much higher than the ductility of 1.98 for the test with no debonding strips. The experimental test with 100-200 debonding strips did however increase the ductility to 2.82. For the numerical test with 75-150 debonding strips the ductility was calculated as 5.68, in comparison to a ductility of 4.72 without debonding strips. Therefore the numerical model does capture the ductility increase within reasonable bounds.

The ductility factor does not give a representation of the maximum shear resistance of the wallettes. Therefore the wallettes could have a high ductility but a low shear resistance. Due to the shortcomings of the ductility factor, the ECF is also used. The ECF can be calculated at different shear-forces to give a better comparison of how the debonding strips alter the behaviour of the masonry wall for the respective shear forces. The ECF for the experimental and numerical tests are listed in Table 4.1. It

shows that the debonding strips increase the energy dissipation of the masonry wall and the numerical model captures this behaviour to some extent.

Table 4.1: Energy Contribution Factors

Strips	Force	175 kN	200 kN	225 kN
75-150	Experimental	1.36	1.62	1.97
	Numerical	1.15	1.12	1.22
100-200	Experimental	2.28	3.02	5.09

4.4 Chapter Conclusion

The masonry model gave a good representation of the experimental results and captured the shear resistance against displacement response adequately. The various failure mechanics especially the diagonal shear failure of the experimental test was also clearly indicated by the numerical model.

The shear resistance against displacement gives a higher initial stiffness and shows that the SHCC retrofitting increases the ductility of the masonry wall, which was not the case for the experimental tests. The ductility values are summarized in Table 4.2. Even though the shear resistance against displacement gave a ductility increase it still gives a reasonable representation of the experimental results.

The debonding strip model captured the failure mechanisms of the experimental tests as well as the increase in ductility and energy dissipation of the debonding strips.

Table 4.2: Ductility Summary

Test	$\bar{\mu}_{experimental}$ (CoV)	$\mu_{numerical}$
Masonry	1.82 (0.187)	3.28
SHCC	1.98 (0.15)	4.72
Strips: 75-150	2.04	5.68
Strips: 100-200	2.82	

It is important to note that there is only two different experimental tests on debonding strips and therefore the available data is limited and the influence of debonding strips is not clear. The experimental test with 75-150 strips showed very little increase in ductility, while the numerical model captures a ductility increase. The ECF was significantly improved in the experimental results but not captured as well in the numerical results. The numerical model is also not sensitive to the strip widths and spacings, but the experimental data is too limited to conclude the influence the strip width and spacing will have on the ductility and ECF.

The material models and analysis procedure are now used to numerically analyse larger structures as discussed in the following chapter.

Chapter 5

Full Scale Model Development

The numerical models developed in the previous chapter are used to model a representative building. The aim is to qualitatively evaluate how SHCC retrofitting will effect the seismic resistance of the buildings.

5.1 Representative Building

There are many multi-story ULM buildings in the Western Cape, South Africa. Figure 5.1 illustrates a typical ULM building in the Cape Flats area. These types of buildings are at risk should a seismic event occur. Van der Kolf (2014) conducted 3D seismic analyses on these buildings and found that they would fail in a seismic event. These are the typical buildings that need to be retrofitted to withstand seismic events. Simplified models of the buildings were analysed in this research, with and without SHCC retrofitting, to determine the full scale effect SHCC will have on a building.



Figure 5.1: Buildings in the Cape Flats area

5.2 Geometry Simplification to 2D model

The residential building as illustrated in Figure 5.1 consists of three floors, with a 250 mm thick slab at each floor. The roof has wooden trusses with steel sheeting. The staircases were omitted from the structure as it does not contribute any structural support. The outer load-bearing walls are all double-leaf walls (220 mm) and the inner walls are single-leaf walls (110 mm), but are not load-bearing (Van der Kolf, 2014). The figure illustrates different wall thickness, but the wall thickness is simplified to 220 mm and 110 mm to disregard the cavity between the walls. The building has to be simplified to a 2D model in order to use the models developed in Chapter 3 and 4. The model was also simplified by using symmetry as the geometry and loading is repetitive and symmetrical throughout the building as seen in the floor plan shown in Figure 5.2. The out of plane behaviour was also not considered.

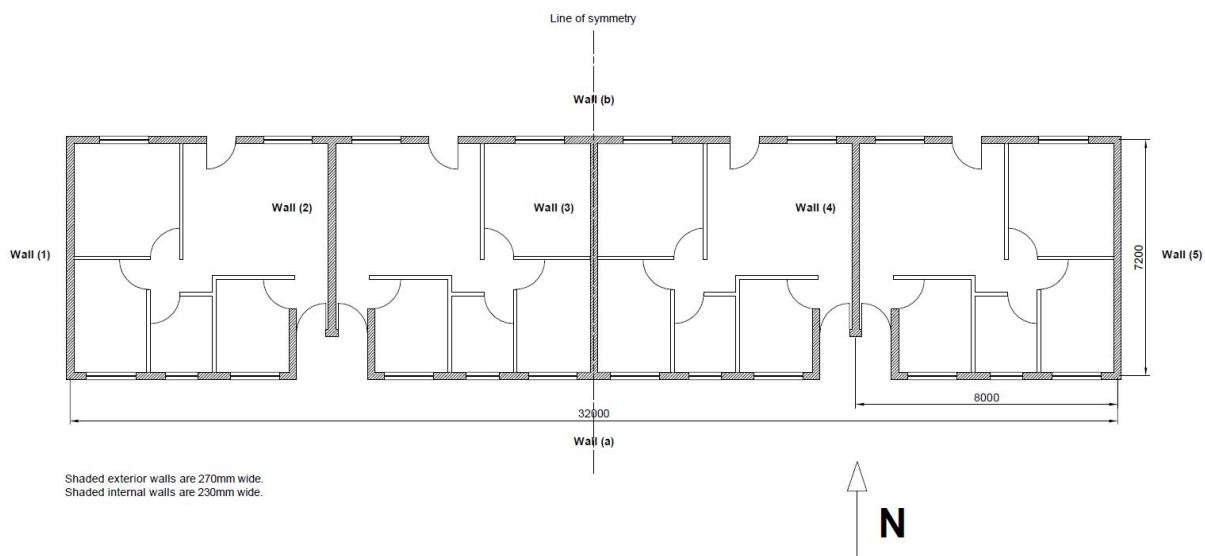


Figure 5.2: General floor plan of the buildings in the Cape Flats area Van der Kolf (2014)

Two different sides of the building were modelled to give a representation of how the building would act as a whole. The *East side*, as illustrated in Figure 5.3, was modelled to capture the behaviour of a continuous wall with no openings, the wall also has no in-plane support of adjacent buildings. As seen in the floor plan of the building, this wall is repeated three times throughout the building and two other walls are similar, but have a higher stiffness. The wall on the East side was chosen to be modelled, due to half of the floor loading acting on the wall in comparison to the inner walls. This is a more conservative approach since lower external compressive force on the masonry lowers its resistance, as per definition of the Rankine-Hill material model. Note that the East side wall is the same as on the West side, but will be referred to as the East side.

The *North side* was selected to capture the behaviour of a full scale wall with openings. The North side had a total length of 32 m, but was simplified to a 8 m length, as illustrated in Figure 5.4. The in-plane support due to the total length of 32 m caused different behaviour in comparison to the East side and has to be taken into account in the simplified model. The North and South sides have similar properties, but the North side was selected due to the upper storeys that have a higher stiffness, and the openings are not on the edges of the model as would be the case for the South side. The higher stiffness of the upper floors increase the fundamental frequency of the structure and increase the quasi-static seismic loading on the base.

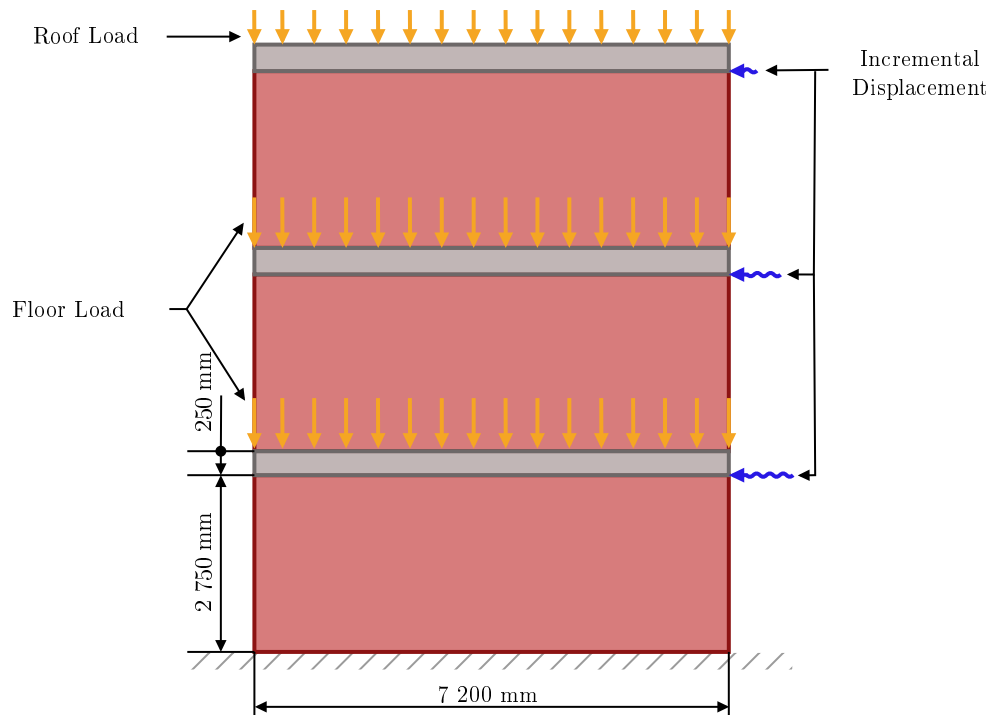


Figure 5.3: East side view illustration of the full scale building with the loading and boundary conditions

5.3 Boundary Conditions

The boundary conditions for both models were applied in order to replicate the global behaviour as close as possible. The out of plane displacements were prevented to obtain only the in-plane response. The horizontal and vertical displacements were fixed at the bottom edge of the ground floor as illustrated in Figures 5.3 and 5.4. A support was defined at each point where the incremental displacements were applied, this is due to the way Diana analyses an induced displacement.

5.3.1 East side Boundary Conditions

The floor slab on the East side acts as a very stiff membrane due to the out of plane geometry of the slab. The thickness of the slab was modelled as 220 mm and the out of plane stiffness had to be replicated by assigning a link between the node where the incremental displacement is applied and the face of the slab to follow the horizontal displacement of the displaced node at each floor respectively. This link ensures that the incremental displacement of the slab is evenly distributed over the whole masonry wall for each floor without constraining the rotation of the slab.

5.3.2 North side Boundary Conditions

Similarly to the East side, the slab's horizontal displacement had to be linked to the node where the incremental displacements were applied to account for the out of plane thickness. In addition to this the vertical displacement was linked to the node and the rotational displacement was completely prevented for each floor respectively. This was done to account for the boundary conditions imposed by the adjacent structure that was not considered in the model, as only a 8 m wide section is modelled in stead of the total 32 m.

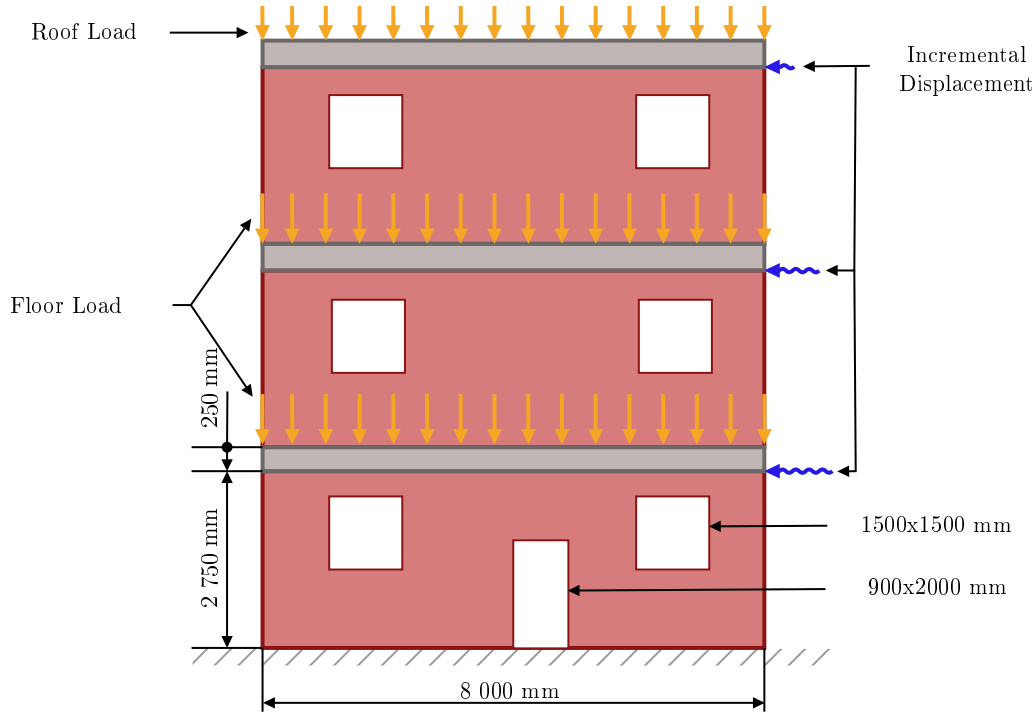


Figure 5.4: North side view illustration of the full scale building with the loading and boundary conditions for the 8 m width

5.4 Loading

The roof and floor loading was determined according to the SANS 10160-1 (2011) design code, and the incremental displacement was calculated by doing a simplified modal analysis for both models.

5.4.1 Service Limit State Design

The service limit state, as defined in SANS 10160-1 (2011), was used to determine the floor and roof loading. Equation 5.4.1 was used where γ is the applicable partial factor, ψ is the combination factor, G is the self weight of the structure, Q is the imposed load and A_d is the seismic action.

$$\sum_{j \geq 1} \gamma_{G,j} \times G_{k,j} + A_d + \sum_{i \geq 1} \gamma_{Q,i} \times \psi_i \times Q_{k,i} \quad (5.4.1)$$

The partial factors for the self weight and imposed loads are 1.0 and 1.1 respectively and a combination factor of 0.3 was used according to SANS 10160-1 (2011). The densities and loadings that were used are listed in Table 5.1, the slabs are 250 mm thick and a 50 mm screed was assumed.

Table 5.1: Densities and Loadings that were applied (SANS 10160-2, 2011)

Self Weight				Imposed Load	
$\rho_{masonry}$	$\rho_{2\%concrete}$	ρ_{screed}	ρ_{roof}	α_{floor}	α_{roof}
21 kN/m ³	25 kN/m ³	23 kN/m ³	0.25 + 0.17 kN/m ²	0.25 kN/m ²	1.5 kN/m ²

Equation 5.4.1 was used with the values in Table 5.1 to obtain the line loads on the roof and floors for the respective models, the line loads used in the model are listed in Table 5.2.

Table 5.2: Line loads applied in the respective models

	East	North
Roof Loading	$-0.89N/mm$	$-0.98N/mm$
Floor Loading	$-14.13N/mm$	$-8.10N/mm$

5.4.2 Modal Analysis

A modal analysis was done to determine the total displacement of each floor due to a seismic force. The approach as discussed in Section 2.7 was followed. The model was simplified to a three degree of freedom problem as illustrated in Figure 5.5. The mass and stiffness of each floor are grouped together and the seismic force is applied to the bottom floor. This was done for each direction respectively, due to the different stiffness in the respective directions. The stiffness of the slab will ensure that the total displacement is induced throughout the floor, therefore the whole stiffness and mass of the respective in-plane directions were considered to obtain the total displacement at each floor.

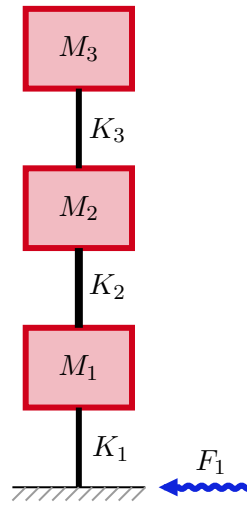


Figure 5.5: Simplified three degree of freedom approach for the modal analysis of the residential building

The mass and stiffness matrices for Equation 2.7.2 are calculated as in Equation 5.4.2 and used to solve the eigenvalues for each direction. The mass for each floor is calculated by using the floor loading as discussed in Section 5.4.1. The stiffness for the respective directions is calculated as $k = 12EI/L^3$ for each floor.

$$[M] = \begin{bmatrix} M_1 & 0 & 0 \\ 0 & M_2 & 0 \\ 0 & 0 & M_3 \end{bmatrix} \quad [K] = \begin{bmatrix} K_1 + K_2 & -K_2 & 0 \\ -K_1 & K_2 + K_3 & -K_3 \\ 0 & -K_3 & K_3 \end{bmatrix} \quad (5.4.2)$$

The eigenvalues for the respective directions were calculated to be as below by solving Equation 2.7.2.

$$\omega_{East} = \left\{ \begin{array}{l} 50.4 \\ 137.7 \\ 188.1 \end{array} \right\} rad/s \quad \omega_{North} = \left\{ \begin{array}{l} 270.7 \\ 739.7 \\ 1010.5 \end{array} \right\} rad/s \quad (5.4.3)$$

The seismic load applied to both the North and East directions is as in Equation 5.4.4, where a is the gravity acceleration.

$$A_d = \begin{Bmatrix} 0.14 a \\ 0 \\ 0 \end{Bmatrix} N \quad (5.4.4)$$

The displacements are calculated by using Equations 2.7.5 to 2.7.8, the total displacements for the respective directions are as in Equation 5.4.5.

$$u_{East} = \begin{Bmatrix} 209.2 \\ 265.2 \\ 280.2 \end{Bmatrix} e^{-3} mm \quad u_{North} = \begin{Bmatrix} 7.2 \\ 9.2 \\ 9.7 \end{Bmatrix} e^{-3} mm \quad (5.4.5)$$

As this method is a simplified method, the displacements used in the models were larger than the calculated values, but the ratios between the floor displacements were kept the same. The final displacements applied in the models are shown in Equation 5.4.6.

$$u_{East} = \begin{Bmatrix} 41.8 \\ 53.0 \\ 56.0 \end{Bmatrix} mm \quad u_{North} = \begin{Bmatrix} 14.5 \\ 18.4 \\ 19.4 \end{Bmatrix} mm \quad (5.4.6)$$

5.5 Mesh

The mesh size of 25 mm for the previous models would cause the full scale models to be unnecessarily computationally intensive. Therefore a new mesh dependency test was done to determine an appropriate mesh size for the full scale models. A similar approach was followed to that in Section 3.1.5, except only a quadratic triangular mesh was considered. Mesh sizes between 50 mm and 500 mm were tested. The shear force against mesh size at different displacements as well as the maximum shear force is illustrated in Figure 5.6. It can be seen that there is different behaviour at the respective displacements. A mesh size of 125 mm was selected for the models due to the maximum shear force obtained at the 2 mm and 9 mm displacement, the shear force is at a minimum for the final displacement, and the 12.2 mm shear force is relatively stable. The 125 mm mesh is an optimal choice as it gives a good representation of the model without being as computationally intensive as for the smaller mesh elements.

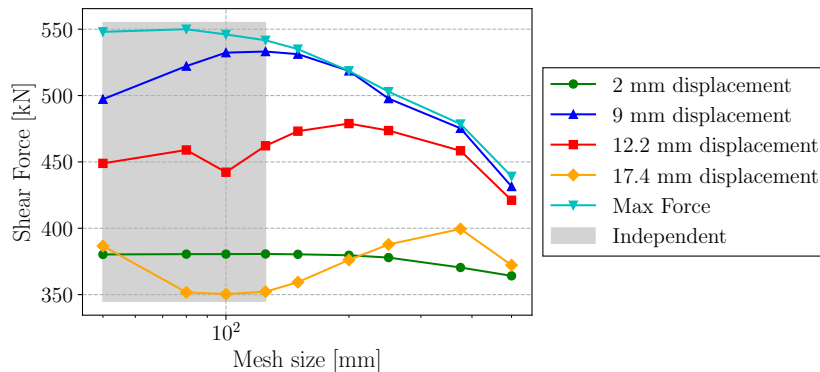


Figure 5.6: Mesh dependency for the full scale models using quadratic triangular elements with high integration

The parabolic hardening softening compression curve for the masonry is illustrated in Figure 5.7. This was obtained using the formulation discussed in Section 2.6.2.1, the material values in Table 3.2 and an

element size of 125 mm was used as input parameters. This is an important consideration to make in order to ensure that the mesh element size is small enough to accurately account for the compression behaviour of the Rankine-Hill material. This was not relevant in the previous models as shear was the dominant force. However this may not be the case for the large models and needs to be taken into account. It was concluded that the 125 mm element size is sufficient to account for the compressive behaviour of the Rankine-Hill material.

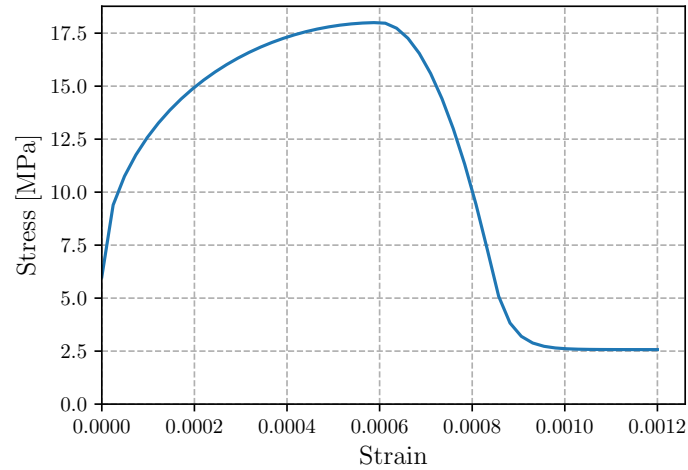
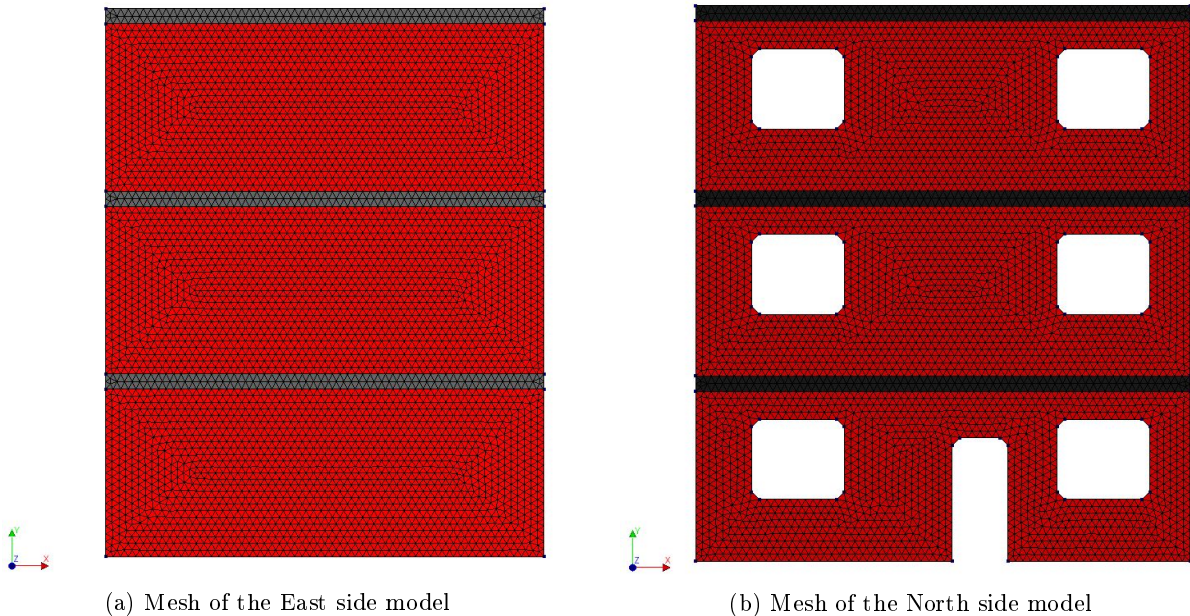


Figure 5.7: Hardening Softening Hill law for the masonry model with 125 mm elements

The mesh used for the East and North sides are illustrated in Figure 5.8. The openings in the North-side model were adapted to chamfer the corners of the openings as illustrated in Figure 5.8(b). This was done to prevent stress concentrations on the corners and causing the model to become numerically unstable. The chamfer size is the same as that of the mesh element size.



(a) Mesh of the East side model

(b) Mesh of the North side model

Figure 5.8: Mesh used for the full-scale models

5.6 Analysis and Output variables

The analysis and output variables were kept the same as that of the previous model discussed in Section 3.1.6 and Section 3.3.

Chapter 6

Full Scale Model Results

This chapter discusses the results obtained from the models developed in Chapter 5 and the retrofitting that were applied in reaction to the results.

6.1 East Side

The East side model as discussed in Chapter 5 was modelled with the masonry alone. The appropriate retrofitting was then applied to the model based on the results.

6.1.1 Masonry

This section discusses the results obtained, with the 220 mm masonry substrate with no retrofitting.

Figure 6.1 illustrates the shear force against displacement for the ground floor of the numerical model. The shear force distribution is similar to that of the wallettes model discussed in Section 4.1, with a maximum shear resistance of 544 kN at 8 mm displacement.

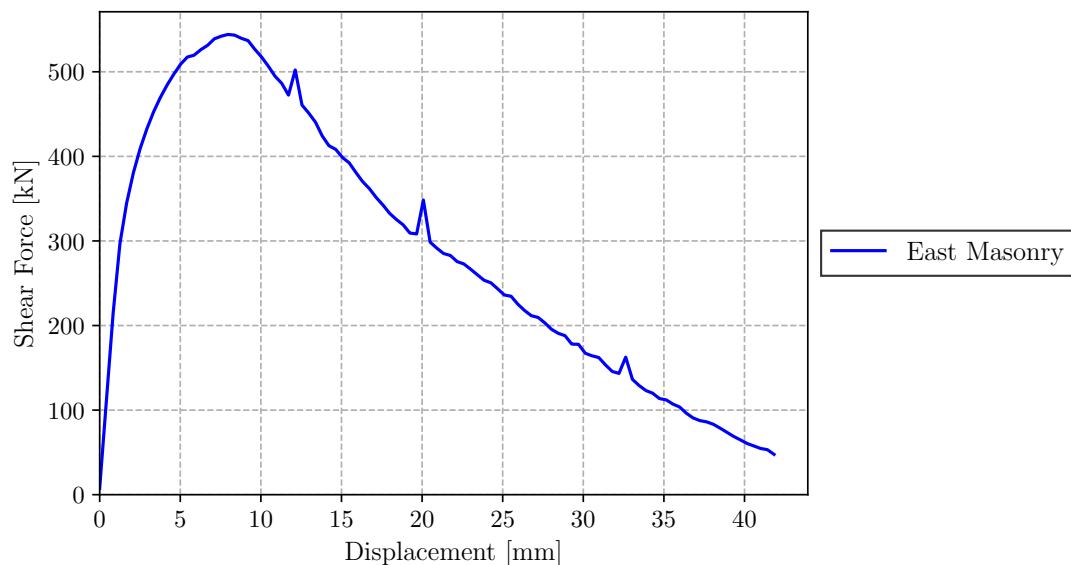


Figure 6.1: Shear force against displacement for the bottom floor of the East side masonry wall with no retrofitting

The ductility of the ground floor masonry wall with no retrofitting is 6.72. This shows a very high ductility, although this is an overestimation as the numerical model shows overly stiff behaviour but this was used as a benchmark for the retrofitted models to give an estimation of the difference between the ductility of the models.

Figure 6.2 illustrates the general trend of the principal strains (E1) in the masonry wall on the ground floor. It can be seen in Figure 6.2(a) that the bottom floor shows the typical diagonal shear cracking over the face of the masonry wall and goes over to toe crushing, as in Figure 6.2(b), after the maximum shear resistance has been reached.

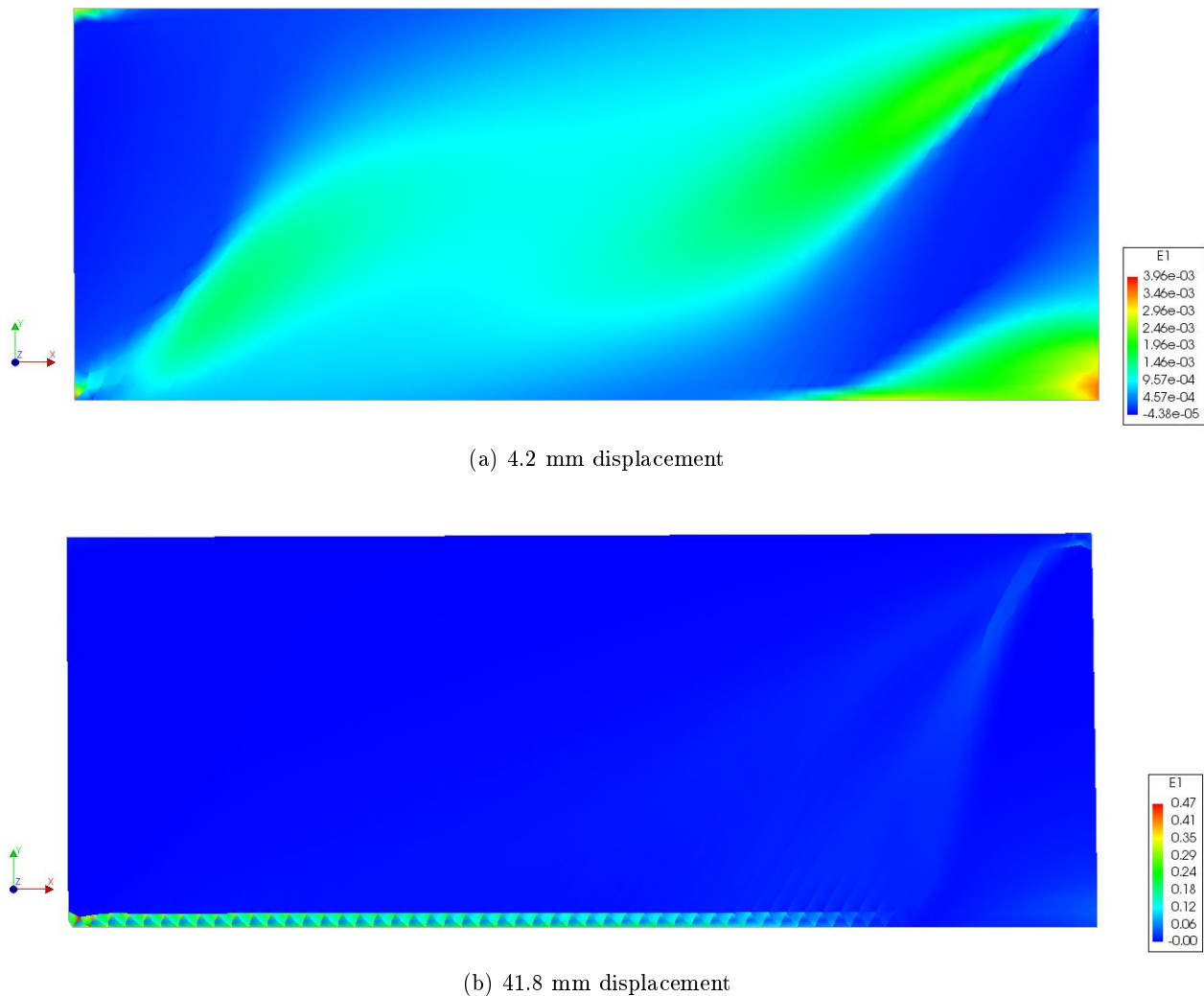


Figure 6.2: Principal strains (E1) in the masonry with no retrofitting on the ground floor of the East side at the respective displacements

6.1.2 SHCC

From the results obtained in Section 6.1.1 it was observed that the maximum strains occurred in the masonry wall of the ground floor. This is also the only wall that showed dominant diagonal shear cracking, therefore only the ground floor was retrofitted with a 15 mm thick SHCC overlay. It is important not to retrofit floors unnecessarily as the additional stiffness would cause the structure to have a higher fundamental frequency leading to higher base loads.

The shear resistance against displacement for the ground floor retrofitted with SHCC is illustrated in Figure 6.3 in comparison to that of the masonry wall alone. The SHCC increased the shear resistance of the masonry wall from 544 kN to 1 586 kN. The ductility is improved from 6.72 to 20.93, this is a significant improvement of the ductility of the masonry wall.

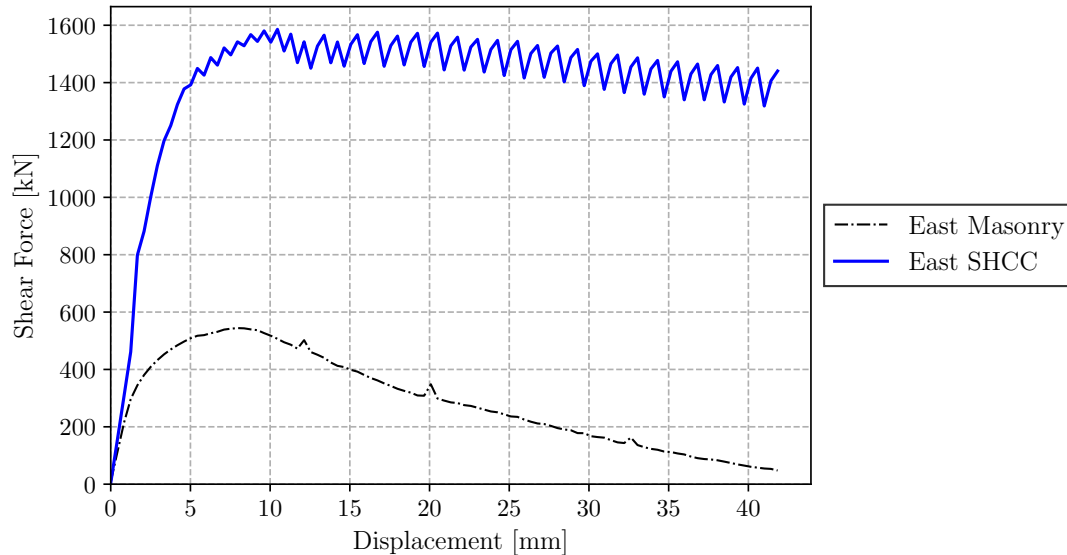


Figure 6.3: Shear force against displacement for the bottom floor of the East side masonry wall with SHCC retrofitting

The principal strain distribution in the SHCC overlay at 41.8 mm displacement is illustrated in Figure 6.4. This is the typical strain distribution in the SHCC overlay throughout the the analysis and the typical diagonal shear cracking does not occur at all throughout the whole analysis. The SHCC changed the failure mechanism of the masonry wall on the East side from a diagonal shear failure to flexural failure. Therefore the added stiffness provided by the SHCC to the ground floor is enough to prevent shear cracking. The flexural failure is a more advantageous failure mechanism for the masonry as it has a high compressive resistance.



Figure 6.4: Principal strains (E1) in the SHCC overlay on the ground floor of the East side at 41.8 mm displacement

Figure 6.5 illustrates the tractions between the SHCC overlay and the masonry substrate at the same displacement as the principal strain illustration. The traction illustrates the flexural failure mechanism and shows that there is very little diagonal shear in the masonry substrate. The toe crushing due to the flexural failure can be seen by the large tractions on the left hand side.

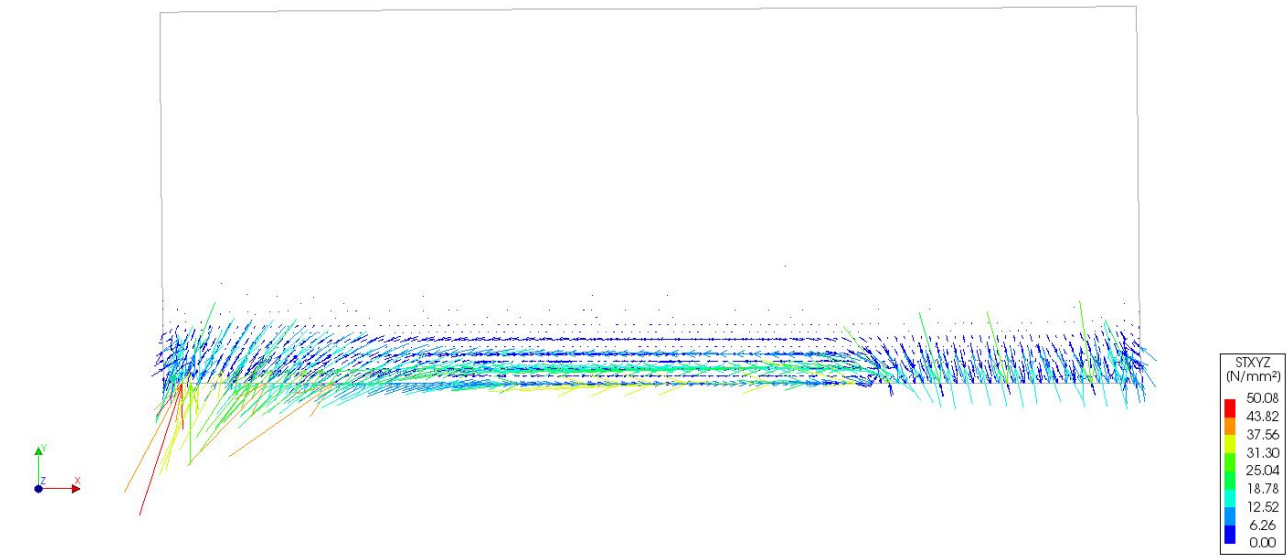


Figure 6.5: Tractions in the SHCC overlay on the ground floor of the East side at 41.8 mm displacement

The SHCC overlay provided enough shear resistance and ductility to the masonry wall that debonding strips are not needed and would also have no effect as there is no diagonal shear cracking and the tractions in the interface are only at the bottom. The SHCC overlay therefore provides sufficient retrofitting to increase the shear resistance by almost 200% and the ductility by 211%.

6.2 North Side

The model for the North side as discussed in Chapter 5 was modelled with masonry alone. Based on the results of this model, the appropriate retrofitting was applied, the results from the retrofitted model was used to determine whether or not debonding strips are required and if so where they are required.

6.2.1 Masonry

This section discusses the results of the model of the North side for a 220 mm masonry wall with no retrofitting. The development of the model is discussed in Section 5.2.

Figure 6.6 illustrates the shear resistance against displacement for the masonry wall on the ground floor with no retrofitting. The 8 m wide masonry wall has a maximum shear resistance of 98.13 kN at 2.5 mm displacement and the shear resistance for the entire 32 m masonry wall is 392.52 kN. The shear resistance against displacement distribution is not as smooth as that of the East side with masonry alone, this is due to the openings in the masonry on the North side. There are also no sporadic modes in the numerical model, confirming that this is not due to numerical instability but the material behaviour.

The ductility of the masonry wall is 5.92, once again this is a high ductility and is due to the stiff behaviour of the numerical model. The ductility was used as a comparison for the retrofitted models.

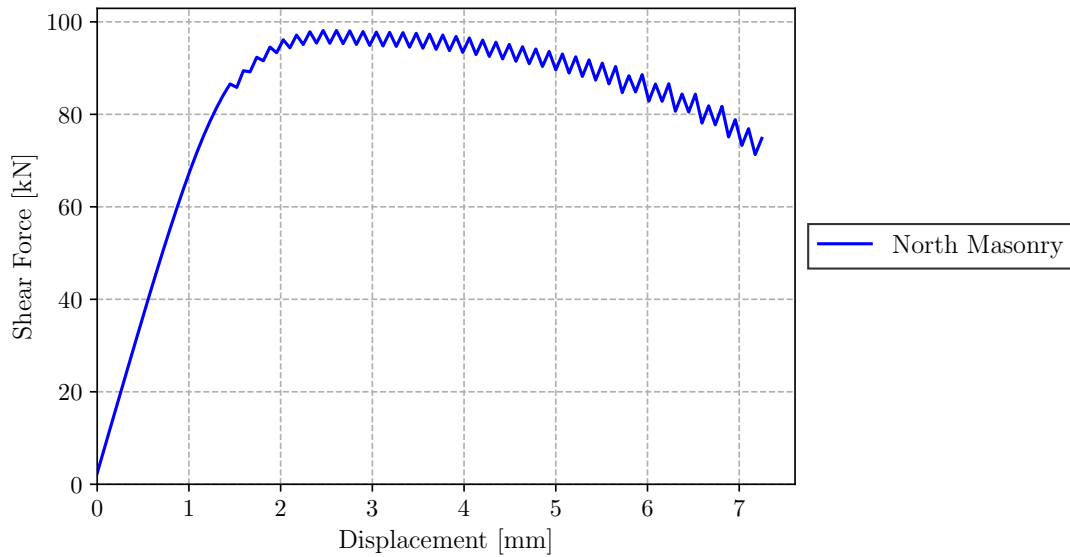


Figure 6.6: Shear force against displacement for the ground floor of the North side masonry wall with no retrofitting

The principal strains (E1) in the masonry wall are illustrated in Figure 6.7 at 7.2 mm displacement. The strain concentrations are dominated by diagonal shear cracking between the openings, specifically from corner to corner, this failure mechanism starts at 1.5 mm and continues till the end of the analysis. Even though the opening corners were chamfered they still capture the strain concentrations and results in a similar shear resistance against displacement distribution in comparison the the un-chamfered openings. The North side masonry wall shows more localised diagonal shear cracking in comparison to that of the East side masonry wall, with no retrofitting, that shows a diagonal shear cracking over the whole wall.

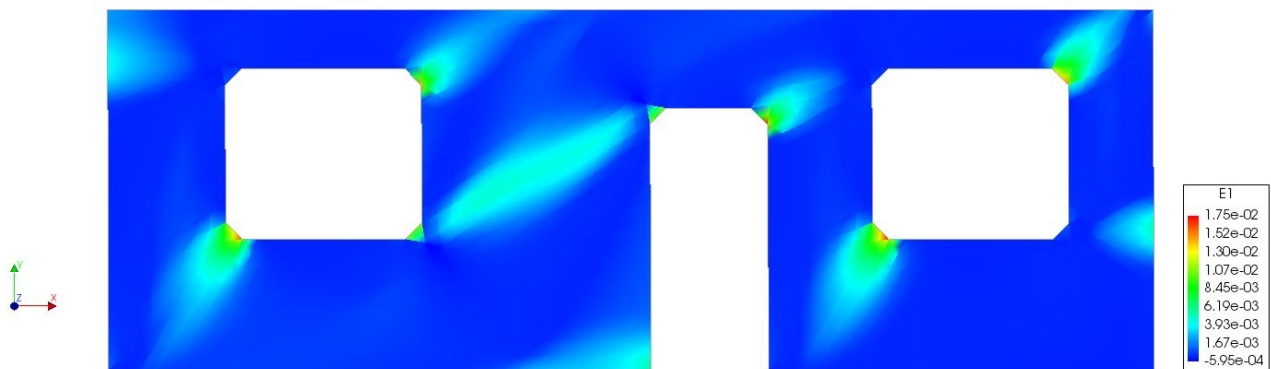


Figure 6.7: Principal strains (E1) in the 220 mm masonry wall on the ground floor with no retrofitting on the North side at 7.2 mm displacement

6.2.2 SHCC

The model discussed in Section 6.2.1 was retrofitted with a 15 mm SHCC overlay on the ground floor as the masonry on this floor had significantly higher strains in comparison to the upper storeys.

The shear resistance against displacement for the ground floor retrofitted with a SHCC overlay is illustrated in Figure 6.8. The SHCC overlay increased the shear resistance of the ground floor from

98.13 kN to 406.06 kN for the 8 m wide model. The ductility of the wall was reduced from 5.92 to 4.71, this is not advantageous and can possibly be improved by adding debonding strips between the masonry substrate and the SHCC overlay.

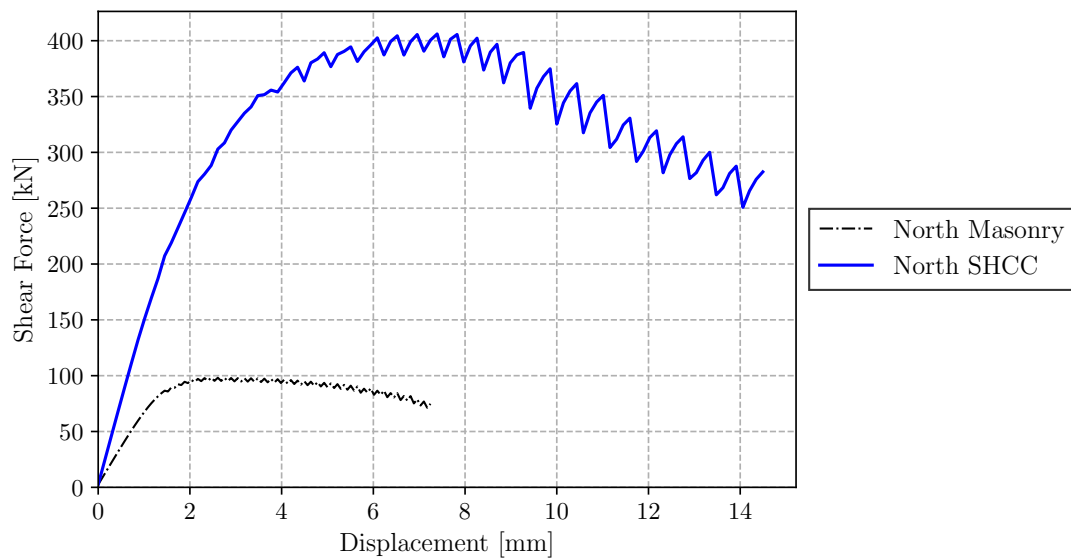


Figure 6.8: Shear force against displacement for the ground floor on the North side with the masonry retrofitted with SHCC on the ground floor alone

The principal strains (E1) in the SHCC overlay is illustrated in Figure 6.9 at 14.5 mm displacement. It can be seen that it shows a similar diagonal strain distribution as the masonry wall with no retrofitting. The SHCC retrofitting did not change the failure mechanism of the masonry wall to flexural failure as for the East side, this is due to the different boundary conditions imposed by the rest of the building. The North side therefore still undergoes diagonal shear failure.

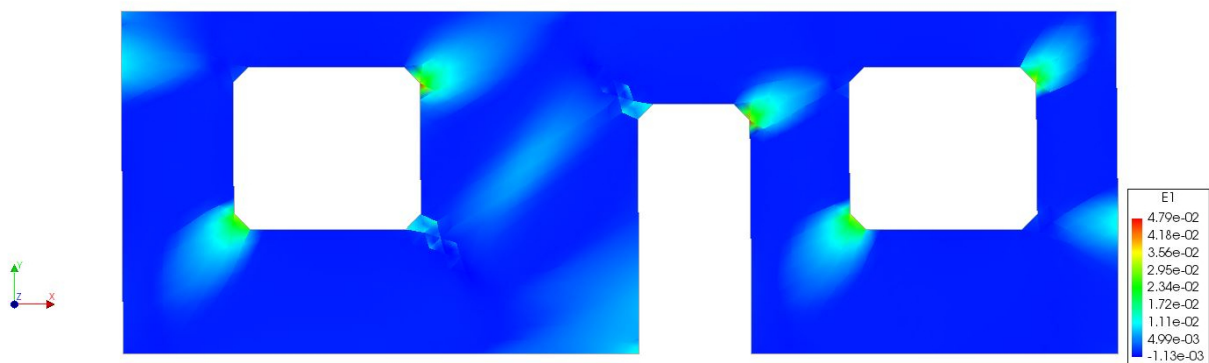


Figure 6.9: Principal strains (E1) in the SHCC overlay on the ground floor of the North side at 14.5 mm displacement

The tractions in the interface between the SHCC overlay and the masonry substrate are illustrated in Figure 6.10 for the same displacements as in Figure 6.9. The highest tractions are on the edges of the ground floor, but there is still a distribution over the face of the interface, unlike the concentrated tractions in the interface of the East side as discussed in Section 6.1.2.

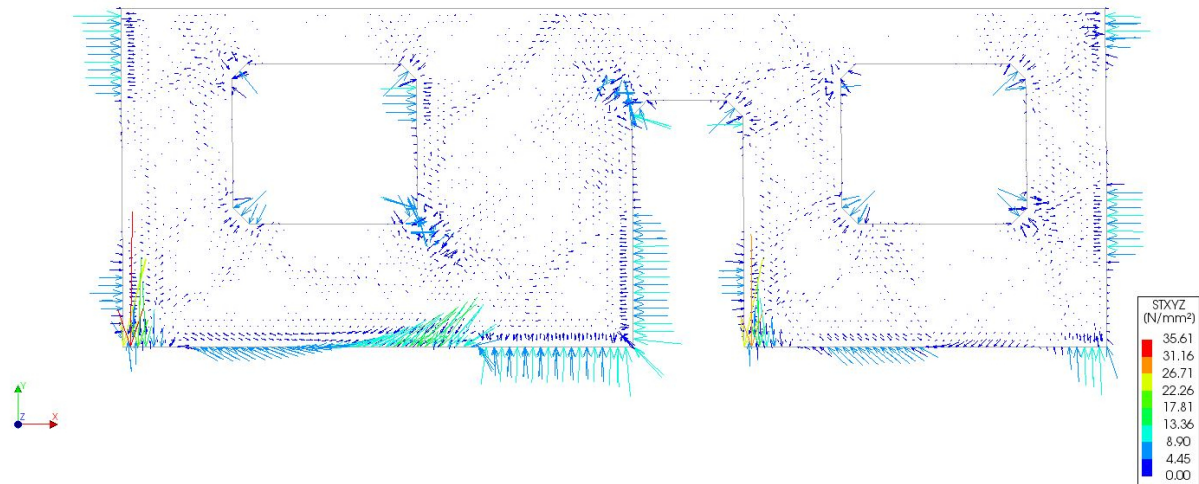


Figure 6.10: Tractions in the interface between the SHCC overlay and the masonry substrate on the ground floor of the North side at 14.5 mm displacement

By adding the SHCC overlay to the ground floor the shear resistance was increased by 313%, but the ductility was reduced by 25%.

6.2.3 Debonding strips

The SHCC overlay improved the shear resistance of the masonry wall, but it did not improve the ductility, therefore debonding strips were applied between the masonry substrate and the SHCC overlay on the diagonals where high strains occurred. Figure 6.11 illustrates where the strips were applied, the strips had a width of 75 mm and a spacing of 150 mm. These are the same strip dimensions that were used for the numerical models in Section 3.2 and the strips were also implemented in the model in the same way.

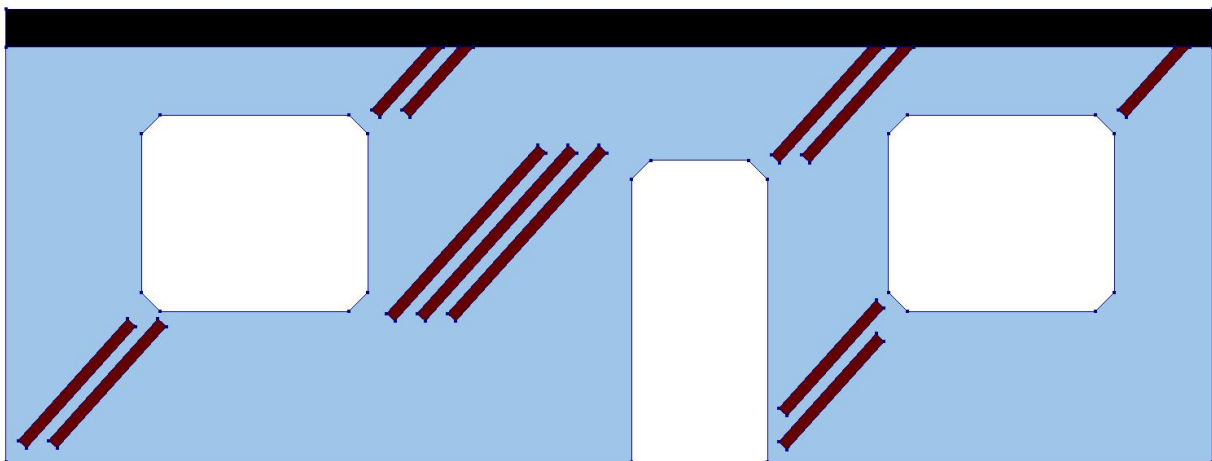


Figure 6.11: 75-150 debonding strips applied to the ground floor of the North side

The shear resistance against displacement for the ground floor retrofitted with a SHCC overlay with debonding strips is illustrated in Figure 6.12 in comparison to the resistance of the masonry wall alone and retrofitted with a SHCC overlay.

The debonding strips had little effect on the masonry wall in comparison to the retrofitted masonry wall. By adding the debonding strips the maximum shear resistance was increased from 406.06 kN to

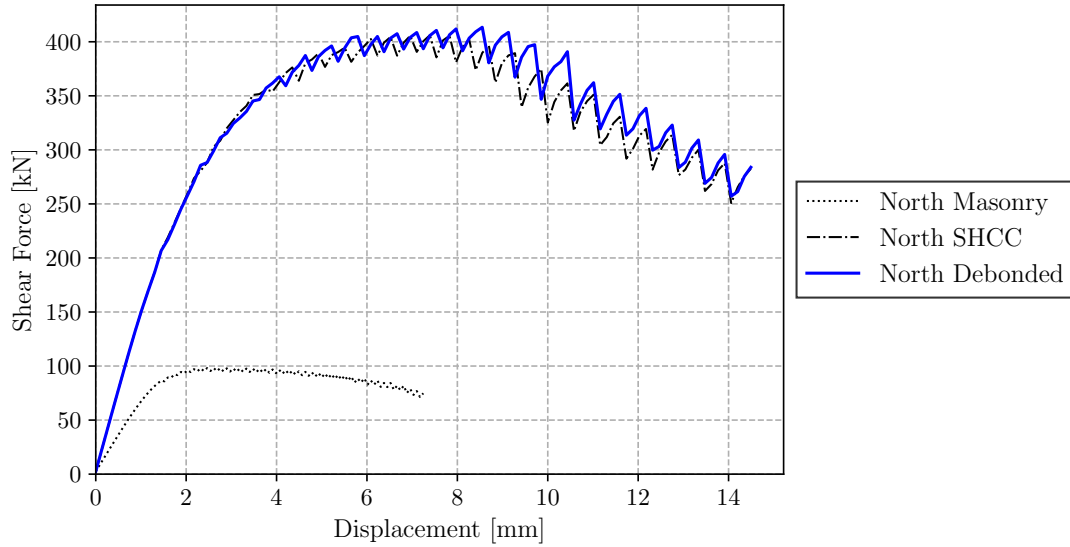


Figure 6.12: Shear force against displacement for the ground floor retrofitted with SHCC and debonding strips on the North side

413.43 kN, and the ductility from 4.7 to 5.1, but it is still less than the ductility of the masonry alone, which has a ductility of 5.9. The ECF at a shear force of 350 kN was 1.11, meaning that the debonding strips only contributed 11% more to the energy dissipation in comparison to the SHCC overlay with no debonding strips. In reality this could be a lot higher as the numerical models in Section 4.3 also showed low ECF values in comparison to the experimental tests. The small by adding the debonding strips could also be due to the debonding strips comprising of a small portion of the total wall face in comparison to the smaller tests.

The principal strain distribution in the SHCC overlay and the tractions in the interface are similar to that of Section 6.2.2, with the exception of the strain and traction concentrations on the debonding strip edges and no tractions in the strip interface as in Section 4.3 for the small numerical tests with debonding strips.

6.3 Chapter Conclusion

The masonry model for the East side gave the typical diagonal shear cracking of the ground floor. The retrofitted SHCC overlay changed the failure mechanism from diagonal shear failure to flexural failure. The ductility and shear resistance was also improved significantly as listed in Table 6.1, it was therefore not needed to add debonding strips to the wall on the East side.

Table 6.1: Ductility factors and maximum shear resistance of the representative building

		Masonry	SHCC	Debonding
East	μ	6.7	20.93	-
	F_s [kN]	544.14	1 585.78	-
North	μ	5.92	4.71	5.12
	F_s [kN]	98.13	406.6	413.44

The numerical model of the masonry on the North side showed diagonal shear cracking between the openings as is typically the case for multi-storey masonry buildings. By retrofitting the ground floor the shear resistance was improved significantly but the ductility was reduced as listed in Table 6.1. By

adding debonding strips the numerical model showed little improvement to the overall behaviour of the retrofitted masonry wall. Possible reasons for this is that the debonding strips consist of a small portion of the wall in comparison to the smaller masonry wallet tests in Section 4.3 and therefore on a larger scale the debonding strips have little effect on the structure as a whole. Another reason may be that the numerical model is not strip sensitive and it does not accurately reflect the effect of the debonding strips. The model results in Section 4.3 show an indication of this due to the debonding and ECF values that did not give a good representation of the experimental results, but did show little improvement. Therefore the debonding strips could have a significant effect on the full scale model that was not captured as effectively in the numerical model and the debonding and ECF values might be higher than what the numerical model showed.

The overall shear resistance of the building was significantly improved, indicating that SHCC retrofitting could be a viable solution to retrofit ULM buildings to better withstand seismic resistance.

Chapter 7

Conclusions and Recommendations

The Conclusions drawn from the smaller FE models are discussed followed by the discussion of the models on the representative building. Recommendations on further improvements and studies are also listed.

7.1 Finite Element Models of Experimental Walls

The FE models based on the experimental tests discussed in Chapter 5 gave a good representation of the experimental models. The ductility factors and maximum shear forces are summarized in Table 7.1. The numerical models capture the maximum shear forces of the experimental results.

Table 7.1: Ductility factors and maximum shear force of the numerical and experimental test for the masonry wallettes

Test	$\bar{\mu}_{experimental}$ (CoV)	$\mu_{numerical}$	$F_{experimental}$ (CoV)	$F_{numerical}$
Masonry	1.82 (0.187)	3.28	131.04 kN (0.014)	130.50 kN
SHCC	1.98 (0.15)	4.72	256.52 kN (0.07)	261.29 kN
Strips: 75-150	2.04	5.68	243.76 kN	252.02 kN
Strips: 100-200	2.82	-	256.98 kN	-

The ductility factors are overestimated in the numerical models, but a similar trend in the ductility factors can be seen by using the ductility factor of the masonry model as a baseline. The numerical model does not represent the full effect of the debonding strips. Overall improvement in ductility was observed by adding debonding strips but the ductility of the 75-150 experimental test did not improve significantly, but it did for the 100-200 strips. The model captured an overall improvement in ductility but not related to a specific strip width. This might also be due to the limited experimental data available, as a reliable conclusion on the effect the strip widths and spacings have on the masonry walls is not clear. This is similar for the ECF values listed in Table 7.2.

Table 7.2: Energy Contribution Factors of the numerical and experimental test for the masonry wallettes

Strips	Force	175 kN	200 kN	225 kN
75-150	Experimental	1.36	1.62	1.97
	Numerical	1.15	1.12	1.22
100-200	Experimental	2.28	3.02	5.09

7.2 Full Scale FE Models of the Representative Building

The full scale numerical results as discussed in Chapter 6, showed that the SHCC retrofitting on the ground floor significantly increased the shear resistance and ductility of the continuous wall on the East side, this increase is listed in Table 7.3. The SHCC retrofitting also changed the failure mechanism from diagonal shear failure to flexural failure. This is advantageous as it significantly increases the seismic resistance of the building on the East and West side.

The numerical model on the North side showed the typical diagonal shear failure between openings on the ground floor with and without SHCC retrofitting. Table 7.3 shows that the SHCC overlay significantly increased the shear resistance of the walls but the ductility was reduced and only increased slightly by adding 75-150 debonding strips. It is important to note that these values are for a 8 m width of the building with a total width of 32 m. As discussed in Section 6.3 a possible reason for the insignificant increase may be that the debonding strips form only a small portion of the wall face or that the numerical model does not fully capture the effect of the debonding strips.

Table 7.3: Summary of the ductility factors and maximum shear resistance for the representative building

		Masonry	SHCC	Debonding
East	μ	6.7	20.93	-
	F_s [kN]	544.14	1 585.78	-
North	μ	5.92	4.71	5.12
	F_s [kN]	98.13	406.6	413.44

The ECF for the North wall retrofitted with an SHCC overlay and debonding strips was 1.11 at 350 kN. This is low and shows that the debonding strips only improve the energy dissipation by 11%. The low ECF was also observed in the wallettes tests as listed in Table 7.2 and therefore the ECF values for the wallettes tests and the full scale test may give a misrepresentation of the true behaviour of the debonding strips.

It is important not to retrofit floors unnecessarily as the additional stiffness would cause the structure to have a higher fundamental frequency leading to higher base loads.

7.3 Recommendations for further research

From this research it was noticed that there are shortcomings with the available experimental data and more experimental data is needed on:

- The necessary material parameters of masonry and sprayable SHCC that are implemented in the numerical model
- More experimental tests on debonding strips are needed to draw reliable conclusions on the effect they have on the ductility and ECF of the retrofitted masonry wallettes
- The effect the debonding strip width and spacing has on the ductility and ECF of the retrofitted masonry wallettes needs to be determined

The numerical model can be refined by:

- Improve the way the rod forces are modelled by either:

- Changing the analysis from a load step to a time step analysis to directly implement the change in rod forces, or
- Modelling the rods as pretension elements so that the increase in the rod forces are computed by the numerical model
- Considering a meso model instead of a macro model to better capture the detailed failure mechanisms
- Refine the material models based on the experimental tests done on the respective materials, specifically focusing on better capturing the failure of SHCC
- Refine the numerical model to capture the effect of debonding strips more accurately to give a better representation of the experimental tests

If the experimental tests on debonding strips confirm that the debonding strips increases the ductility and ECF of the masonry walls and a numerical model captures this behaviour accurately, the following research can be done numerically on debonding strips:

- The debonding strip layout only takes into account displacements from one way, this is not the case in seismic events. The debonding strip layout can be optimized by using the refined numerical model to obtain the optimal debonded surface area and placement of the debonding strips to account for the two way displacement induced in seismic actions
- An optimal debonded area to bonded area ratio and placement can be determined to fully utilize the debonding strips and to prevent delamination

Further experimental tests followed by numerical tests are necessary with seismic loading on masonry and masonry retrofitted with SHCC to determine the loading and unloading behaviour.

The out-of-plane behaviour of the masonry and masonry retrofitted with SHCC has to be determined and three dimensional numerical models accounting for the out-of-plane as well as the in-plane behaviour can be set up.

Bibliography

- ASTM (2010). Standard test method for diagonal tension (shear) in masonry assemblages.
- Beushausen, H. and Chilwesa, M. (2013). Assessment and prediction of drying shrinkage cracking in bonded mortar overlays. *Cement and Concrete Research*, vol. 53, pp. 256–266.
- Boshoff, W.P. (2007). *Time-dependant behaviour of engineered cement-based composites*. Ph.D. thesis, Stellenbosch: University of Stellenbosch.
- Bruedern, A., Abecasis, D. and Mechtcherine, V. (2009). Development of strain-hardening cement-based composites for the strengthening of masonry.
- Chilwesa, M. (2012). *Assessing the age at cracking of concrete repair mortars*. Ph.D. thesis, University of Cape Town.
- Churilov, S. and Dumova-Jovanoska, E. (2011). Experimental evaluation of in-plane shear behaviour of unreinforced and strengthened brick masonry walls. In: *7th International Conference amcm*.
- Coburn, A.W., Spence, R.J. and Pomonis, A. (1992). Factors determining human casualty levels in earthquakes: mortality prediction in building collapse. In: *Proceedings of the First International Forum on Earthquake related Casualties. Madrid, Spain, July 1992*.
- Council, N.R. *et al.* (2003). *Preventing earthquake disasters: the grand challenge in earthquake engineering: a research agenda for the Network for Earthquake Engineering Simulation (NEES)*. National Academies Press.
- De Beer, L.R. (2016). *Developing and testing a sprayable overlay of Strain Hardening Cement-based Composite for retrofitting of unreinforced load bearing masonry walls*. MEng-thesis, Department of Civil Engineering, Stellenbosch University. 138pp.
- De Jager, D.J.A. (2018). *Assessment of SHCC overlay retrofitting of unreinforced load bearing masonry for seismic resistance*. MEng-thesis, Department of Civil Engineering, Stellenbosch University. 145pp.
- De Villiers, W.I. (2019). *Computational and Experimental Modelling of Masonry Walling towards Performance-Based Standardisation of Alternative Masonry Units for Low-Income Housing*. PhD dissertation, Department of Civil Engineering, Stellenbosch University.
- Dehghani, A., Fischer, G. and Alahi, F. (2015). Strengthening masonry infill panels using engineered cementitious composites. pp. 185–204.
- DIANA FEA BV (2006). DIANA Theory manual. ISSN 9254492507.
- DIANA FEA BV (2017a). User 's Manual Analysis Procedures.
- DIANA FEA BV (2017b). User 's Manual Element Library.

- du Béton, C.E.-I. (1993). *CEB-FIP model code 1990: Design code*. 213-214. Telford.
- ElGawady, M., Lestuzzi, P. and Badoux, M. (2006). Retrofitting of masonry walls using shotcrete. *2006 NZSEE Conference*, , no. 45, pp. 45–54.
- Ferreira, D. (2013). *A model for the nonlinear, time-dependent and strengthening analysis of shear critical frame concrete structures*. PhD dissertation, Universitat Politècnica de Catalunya, Barcelona Tech.
- Govindjee, S., Kay, G.J. and Simo, J.C. (1995). Anisotropic modelling and numerical simulation of brittle damage in concrete. *International journal for Numerical Methods in Engineering*, vol. 38, no. 21, pp. 3611–3633.
- Hordijk, D. (1991). *Local approach to fatigue of concrete*. PhD dissertation, Delft University of Technology.
- JSCE (2010). Standard specifications for concrete structures - 2007.
- Kim, y., kong, H. and Li, V. (2003). Design of Engineered Cementitious Composite Suitable for. , no. 100.
- Li, V.C., Wang, S., Wu, C. *et al.* (2001). Tensile strain-hardening behavior of polyvinyl alcohol engineered cementitious composite (pva-ecc). *ACI Materials Journal-American Concrete Institute*, vol. 98, no. 6, pp. 483–492.
- Lin, Y.-W., Wotherspoon, L., Scott, A. and Ingham, J.M. (2014). In-plane strengthening of clay brick unreinforced masonry wallettes using ecc shotcrete. *Engineering Structures*, vol. 66, pp. 57–65.
- Lin, Z. and Li, V.C. (1997). Crack bridging in fiber reinforced cementitious composites with slip-hardening interfaces. *Journal of the Mechanics and Physics of Solids*, vol. 45, no. 5, pp. 763–787.
- Lourenco, P. (1996). *Computational strategies for masonry structures*. PhD dissertation, Delft University, The Netherlands.
- Luković, M., Dong, H., Šavija, B., Schlangen, E., Ye, G. and van Breugel, K. (2014). Tailoring strain-hardening cementitious composite repair systems through numerical experimentation. *Cement and Concrete Composites*, vol. 53, pp. 200–213.
- Mahmood, H. and Ingham, J.M. (2011). Diagonal compression testing of frp-retrofitted unreinforced clay brick masonry wallettes. *Journal of Composites for Construction*, vol. 15, no. 5, pp. 810–820.
- Paul, S.C. (2015). *The Role of Cracks and Chlorides in Corrosion of Reinforced Strain Hardening Cement-Based Composite (R/SHCC)*. PhD dissertation, University of Stellenbosch.
- Rots, J.G. (1988). *Computational Modeling of Concrete Fracture*. PhD dissertation, Delft University of Technology.
- SABS 0160 (1989). *The structural use of masonry, part 1: Unreinforced masonry walling*. South African Bureau of Standards, South Arica.
- SANS 10160-1 (2011). Sans 10160-1: Basis of structural design and actions for buildings and industrial structures. part 1: Basis of structural design.
- SANS 10160-2 (2011). Sans 10160-1: Basis of structural design and actions for buildings and industrial structures. part 2: Self-weight and imposed loads.
- SANS 10160-4 (2011). Sans 10160-4: Basis of structural design and actions for buildings and industrial structures. part 4: Seismic actions and general requirements for buildings.

- Shang, Q. (2006). *Shear Behaviour of Engineered Cement-based Composites*. Ph.D. thesis, Stellenbosch: University of Stellenbosch.
- Stander, H. (2007). *Interfacial bond properties for ECC overlay systems*. Ph.D. thesis, Stellenbosch: University of Stellenbosch.
- Strasheim, B., Maincon, P. and Wium, J. (2018). Introduction to dynamic analysis of structures.
- Taerwe, L., Matthys, S. *et al.* (2013). Fib model code for concrete structures 2010.
- Thorenfeldt, E. (1987). Mechanical properties of high-strength concrete and applications in design. In: *Symposium Proceedings, Utilization of High-Strength Concrete, Norway, 1987*.
- Tomažević, M. (1999). *Earthquake-Resistant Design of Masonry Buildings*. 1st edn. Imperial College Press, London. ISBN 1-86094-066-8.
- Van der Kolf, T. (2014). *The Seismic Analysis of a Typical South African Unreinforced Masonry Structure*. PhD dissertation, Department of Civil Engineering, Stellenbosch University.
- van Zijl, G.P.A.G. and de Vries, P.A. (2005). Masonry Wall Crack Control with Carbon Fiber Reinforced Polymer. *Journal of Composites for Construction*, vol. 9, no. 1, pp. 84–89. ISSN 1090-0268.
- Visser, C.R. (2007). *Mechanical and structural characterisation of extrusion moulded SHCC*. Ph.D. thesis, Stellenbosch: Stellenbosch University.
- Wium, J.A. and van Zijl, G.P.A.G. (2005). The South African loading code: Revision of provisions for seismic loading. Tech. Rep., Department of Civil Engineering, University of Stellenbosch.
- Wu, Z.S. and Bazant, Z.P. (1993). Finite element modeling of rate effect in concrete fracture with influence of creep. *Creep and Shrinkage of Concrete*, pp. 427–432.

Appendix A

Digital Appendix

A digital Appendix is provided.